

**DOSIMETRIC CHARACTERIZATION OF A MINIATURE X-RAY SOURCE  
FOR BIOPHYSICS STUDIES**

By

Karanvir Singh Virdi

A THESIS SUBMITTED IN PARTIAL FULFILLMENT OF THE REQUIREMENTS  
FOR THE DEGREE OF  
Master of Applied Science

In

Nuclear Engineering

Faculty of Energy Systems and Nuclear Science

University of Ontario Institute of Technology

July, 2015

© Karanvir Singh Virdi, 2015

## ABSTRACT

Tritium is a low energy beta emitter that is found in abundance at CANDU nuclear power plants and is a cause of concern since it accounts for roughly thirty three percent of the total occupational exposure of nuclear workers. According to current standards, the radiation weighting factor for all electrons irrespective of their energies is 1. However, there is some evidence suggesting that this factor for low energy electrons could be more than 1. Due to the complexities associated with handling tritium in a liquid or gaseous state alternate arrangements to simulate tritium radiation are investigated. Therefore, in this project it is proposed to use a miniature X-Ray source (Mini-X) to simulate tritium radiation and characterise these low energy X-Ray beams with the aim of investigating the relative biological effectiveness of low energy electrons.

The scope of this study is to design and characterize low energy X-Ray beams, suitable for biophysical experiments using Gafchromic's XR-QA2 radiochromic film and Standard Imaging's A-20 ionization chamber. To safely carry out the characterization experiments a dual layered safety shielding was constructed and parameters including beam dimensions, air-kerma and dose to tissue values from the Mini-X were explored. Lastly, a cross calibration curve between an optically stimulated luminescent dosimeter (nanoDots) and A-20 ionization chamber was established, with an aim to use nanoDots for a proposed future biophysical experiment.

It was found that the Mini-X produced a flat beam profile at distances up to 12.7 cm from the source. In addition, air-kerma values of 11.56 and 6.442 cGy/s could be obtained at 2.54 cm and 5.08 cm respectively with operating parameters of 20 keV and 75  $\mu$ A. It was also established that there is no substantial difference between air-kerma and dose to tissue

values for the X-Ray beams studied. For future work, a biophysical experiment would be carried out using fish eggs where the impact of the Mini-X X-Ray beams on egg hatchability and embryonic mortality would be measured.

## ACKNOWLEDGEMENTS

I would like to take this opportunity to express my deep gratitude to Dr. Anthony Waker for being an excellent mentor throughout the course of my graduate studies. His exemplary patience, undying enthusiasm, and constant encouragement made this research work an enjoyable experience throughout. I would like to thank him for providing me with this opportunity and also for his constant guidance and support throughout.

I would also like to thank all the professors and staff of FESNS for their help and support. Special thanks to Dr. Gloria Orchard for her continued help and encouragement.

I would also like to thank Natural Sciences and Engineering Council of Canada (NSERC) and the University Network of Excellence in Nuclear Engineering (UNENE) for their financial contributions for this research work.

Lastly, I would like to thank my family and close friends for believing in me and inspiring me through every aspect of my life. Special thanks to all the graduate students in ERC 4100 for providing an excellent working atmosphere and making this a truly memorable experience.

## TABLE OF CONTENTS:

<b>ABSTRACT</b> .....	(i)
<b>ACKNOWLEDGMENTS</b> .....	(iii)
<b>LIST OF TABLES</b> .....	(vi)
<b>LIST OF FIGURES</b> .....	(vii)
<b>LIST OF ACRONYMS</b> .....	(xii)
<b>CHAPTER 1: INTRODUCTION</b> .....	1
1.1 Ionizing and Non-Ionizing Radiation.....	1
1.2 Relative Biological Effectiveness.....	4
<b>CHAPTER 2: THESIS OBJECTIVES</b> .....	8
2.1 Proposal and Objectives.....	8
2.2 Outline of Thesis.....	11
<b>CHAPTER 3: THEORETICAL BACKGROUND</b> .....	12
3.1 Tritium and Low Energy Beta Particles.....	12
3.2 Photon Interaction with Matter.....	16
<b>CHAPTER 4: MATERIALS AND METHODS</b> .....	14
4.1 X-Ray Source.....	21
4.2 Detectors.....	26
4.2.1 X-123 Spectrometer.....	26
4.2.2 Radiochromic Films.....	30
4.2.3 Analyzing Radiochromic films.....	32

4.2.4	A-20 ionization chamber and SuperMAX electrometer.....	36
<b>CHAPTER 5: EXPERIMENTAL SETUP.....</b>		<b>41</b>
5.1	Design and construction of Low Energy Photon Irradiation Facility .....	41
<b>CHAPTER 6: RESULTS AND DISCUSSIONS.....</b>		<b>47</b>
Beam Characterization.....		47
6.1	Beam Dimensions.....	47
6.2	Beam Uniformity.....	57
6.3	Ion Chamber Dosimetry .....	62
6.3.1	Air Kerma vs. Distance.....	62
6.3.2	Dose to Tissue.....	69
6.4	Cross calibration of A-20 ionization chamber and Landauer’s OSL nanoDots.....	81
6.4.1	Introduction.....	81
6.4.2	Experimental Setup and Landauer’s OSL nanoDots.....	82
6.4.3	Results-Cross Calibration Curve.....	87
<b>CHAPTER 7: CONCLUSIONs AND FUTURE WORK.....</b>		<b>94</b>
<b>APPENDIX A: RAW DATA TABLES.....</b>		<b>97</b>
<b>REFERENCES.....</b>		<b>99</b>

## LIST OF TABLES

1.1 Radiation Weighing Factors.....	6
4.1 Calibration data for X-123 spectrometer.....	28
4.2 Properties of XR-QA2 film.....	31
4.3 Calibration values for ImageJ.....	35
6.1 Characteristic X-Rays and beam energies for different spectra.....	74
6.2 Comparison between air-kerma and dose to tissue.....	78

## LIST OF FIGURES

1.1 Ionizing and Non-Ionizing radiation in electromagnetic spectrum.....	1
1.2 Direct and Indirect action of radiation.....	3
1.3 Low LET vs High LET radiations.....	4
1.4 Graph representing the concept of RBE.....	5
2.1 Tritium beta-decay spectrum.....	8
2.2 Mini-X output at varying energies.....	9
3.1 Total Stopping Power vs. Energy for electrons.....	15
3.2 Photon Interaction with Matter.....	16
3.3 Photoelectric vs. Compton interaction cross sections in water for low energy photons.....	18
3.4 Spectra comparison between Mini-X and Tritium.....	19
3.5 Spectra comparison between Tritium and simulated electron spectrum.....	20
4.1 Schematic of a modern day X-Ray tube.....	21
4.2 Production of Characteristic X-Rays.....	22
4.3 Mini-X X Ray tube.....	23
4.4 Back Panel of Mini-X showing Interlock and flashing LED/beeper on the Mini-X...	24
4.5 Angular Response of Mini-X.....	24
4.6 Amptek Mini-X spectrum at 50 kV.....	25
4.7 Screenshot of the controller's panel of the Mini-X.....	25
4.8 The X-123 spectrometer.....	26
4.9: Connection diagram and schematic for X-123 spectrometer.....	27
4.10: Energy resolution of X-123 spectrometer.....	27

4.11: Americium-241 spectrum as measured by X-123 spectrometer.....	28
4.12: Iron-55 spectrum as measured by X-123 spectrometer.....	29
4.13: Energy calibration curve.....	29
4.14: Schematic of Gafchromic's XR-QA2 film.....	30
4.15: i) Radiochromic film before being exposed to radiation ii) Radiochromic film after being exposed to radiation.....	31
4.16: Optical Density distribution for a given irradiated film.....	33
4.17: Optical Density calibration using step-tablet.....	34
4.18: Optical Density calibration curve.....	34
4.19: Design of a typical parallel plate ionization chamber.....	36
4.20: Saturation curve for Exradin's A-20 ionization chamber.....	38
4.21: The SuperMax electrometer display.....	38
4.22: Exradin's A-20 ionization chamber along with its calibration certificate.....	40
5.1: Pre-existing experimental setup.....	41
5.2 Schematic of the experimental setup.....	42
5.3: Frontal view of the experimental setup showing the magnet controlling the reed switch, SuperMAX electrometer and Canon 8800F scanner.....	43
5.4: Top view of the experimental setup.....	44
5.5: Experimental setup with the radiochromic film attachment.....	45
5.6: Schematic of the interlock circuit.....	46
5.7: Interlock circuit on the PCB board showing the reed switch, capacitor and a voltage regulator.....	46
6.1: Optical Density vs. time for the Mini-X source.....	48
6.2: Film Response for P-385 Thermo Fisher Neutron Generator.....	49

6.3: Mini-X Accessories.....	50
6.4: Lines showing how the beam height and beam width are defined on the film.....	50
6.5: Beam size at 10 keV and 50 micro-amps with 3 mm collimator.....	51
6.6: Beam size at 10 keV and 50 micro-amps with just the brass cover.....	52
6.7: Beam size at 20 keV and 50 micro-amps using the brass cover.....	52
6.8: Beam size at 20 keV and 50 micro-amps using the 3 mm collimator.....	53
6.9: Beam size at at 25 keV and 50 micro-amps using the brass cover.....	53
6.10: Beam size at 25 keV and 50 micro-amps using the 3 mm collimator.....	54
6.11: Beam size at 25 keV and 50 micro-amps using the brass cover.....	54
6.12: Beam size at 15 keV and 50 micro-amps using the 3 mm collimator.....	55
6.13: Beam width as a function of distance for different energies.....	55
6.14: Beam height as a function of distance for different energies.....	56
6.15: Scale calibration in ImageJ.....	58
6.16: Example of the how the line method can be used to obtain the spatial distribution at varying positions along the image.....	59
6.17: Spatial distribution of the 20 keV beam at 2.54 cm from the source.....	60
6.18: Film exposed to 20 keV beam at 2.54 cm from the source.....	60
6.19: Spatial distribution of the beam at 7.62 cm from the source.....	61
6.20: Radiochromic film exposed to 20 keV at 7.62 cm from the source.....	61
6.21: Air-Kerma rate vs. Distance for the Mini-X at varying energies.....	63
6.22: Experimental values vs. Inverse square fit.....	65
6.23: Effect of current on the dose rate.....	66
6.24: Current vs. Dose for different energies.....	67
6.25: Graph comparing the dose rates obtained using different collimators.....	68

6.26: Change in air-kerma as a function of beam size.....	68
6.27: Graph showing relationship between $\mu_{en/p}$ (Water) and Energy.....	70
6.28: Graph showing relationship between $\mu_{en/p}$ (Air) and Energy.....	70
6.29: Energy spectrum at 10 keV.....	71
6.30: Energy spectrum at 15 keV.....	72
6.31: Energy spectrum at 20 keV.....	72
6.32: Energy spectrum at 25 keV.....	73
6.33: Energy spectrum at 30 keV.....	73
6.34: X-123 spectrometer with brass collimator.....	76
6.35: Simulated and Experimental Mini-X spectra at 20 keV using iron filter.....	76
6.36: Dose in Tissue vs. Dose in Air @ 10 keV and 5 micro-amps.....	79
6.37: Dose in Tissue vs. Dose in Air @ 15 keV and 5 micro-amps.....	79
6.38: Dose in Tissue vs. Dose in Air @ 20 keV and 5 micro-amps.....	80
6.39: Dose in Tissue vs. Dose in Air @ 25 keV and 5 micro-amps.....	80
6.40: Mass attenuation ratios (Tissue/Air) vs. Energy.....	81
6.41: Landauer's InLight nanoDot.....	82
6.42: Image showing complete setup involving the nanoDots and microStar reader.....	83
6.43: Summary of the process of emission of thermoluminescence of photons.....	84
6.44: Vial housing the fish eggs for proposed biophysics experiment.....	85
6.45: Proposed experimental setup for the biophysics experiment using fish eggs.....	86
6.46: Dose Rate as a function of Energy at 100 $\mu$ A current using the A-20 ionization chamber.....	87

6.47: Dose Rate as a function of Energy at 100 micro-amps current using the OSL nanoDots.....	88
6.48: Dose Rate ratio (Ionization Chamber/OSL nanoDots) plotted as a function of Energy.....	89
6.49: Dose Rate comparison between nanoDots and ionization chamber at 100 $\mu$ A tube current.....	90
6.50: Dose Rate comparison between nanoDots and ionization chamber at 200 $\mu$ A tube current.....	90
6.51: Schematic of the petri dish showing the nanoDots facing the X-Ray beam.....	91
6.52: Beam Profile for the x-axis at varying distances from the X-Ray tube.....	92
6.53: Beam Profile for the y-axis at varying distances from the X-Ray tube.....	92

## LIST OF ACRONYMS

<b>LET</b>	Linear Energy Transfer
<b>RBE</b>	Relative Biological Effectiveness
<b>AAPM</b>	American Association of Physicists in Medicine
<b>ICRP</b>	International Commission of Radiological Protection
<b>CANDU</b>	Canada Deuterium Uranium
<b>MCNP</b>	Monte Carlo N-Particle Code
<b>MCA</b>	Multi-Channel Analyzer
<b>FWHM</b>	Full Width Half Maximum
<b>USB</b>	Universal Serial Bus
<b>ROI</b>	Region of Interest
<b>KERMA</b>	Kinetic Energy Released per Unit Mass
<b>TLD</b>	Thermoluminescent Dosimeter1

# CHAPTER-1

## INTRODUCTION

### 1.1 Ionizing and Non-Ionizing Radiation

The application of radiation has become a cornerstone activity for many modern day industries however, the use of radiation is still a cause of concern for many in society in spite of the research that has been done to correctly identify the effects of radiation as a whole.

Radiation can be broadly classified into two different categories, namely ionizing and non-ionizing radiation. The difference between these two types of radiation is defined by their ability or non-ability to ionize a given atom or molecule. For example, ionizing radiation tends to carry much higher energy per given quanta and has the ability to ionize the medium it traverses via atomic interactions. Non-ionizing radiation on the other hand lacks the ability to induce atomic electron transitions that result in ionization of the target atom. It is due to this process of ionization that ionizing radiation tends to be much more harmful for biological tissue as compared to non-ionizing radiation [1]. Figure 1.1 highlights different type of ionizing and non-ionizing radiation within the electromagnetic spectrum.

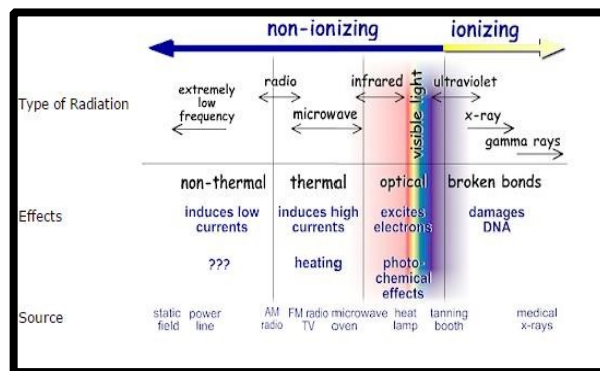


*Figure 1.1: Ionizing and Non-Ionizing Radiation in electromagnetic spectrum [2]*

Ionizing radiation can further be classified into directly and indirectly ionizing radiation. Directly ionizing radiation as the name suggests, is the type of radiation that can directly ionize the target atom due to its electrically charged nature. Electrons, alpha-particles and beta particles are examples of directly ionizing radiation. Indirectly ionizing radiation on the other hand is electrically neutral and works by interacting with the target material to produce fast moving charged particles which produces biological damage. Photons and neutrons are examples of indirectly ionizing radiation. X-Rays are photons that are classified as indirectly ionizing radiation and can interact with matter via three different mechanisms as outlined in section 3.2. For example, X-Rays can interact with matter via the photoelectric effect to produce charged particles in the form of electrons and these electrons can cause multiple ionization events within a given biological media to produce biological effects [1].

Ionizing radiation can produce biological effects via two different interaction mechanisms, namely direct and indirect action. In the direct action, the incident radiation interacts directly with the atoms of the DNA to cause single or double strand breaks whereas in the indirect action the incident radiation does not 'directly' damage the DNA molecules. For this interaction mechanism, ionizing radiation can interact with surrounding water molecules to produce highly reactive free radicals such as the hydroxyl ( $\cdot\text{OH}$ ) radical which can then attack the DNA molecules to produce biological damage. X-Rays interact predominantly via the indirect action and produce seventy percent of its biological effect via this interaction mechanism. To elaborate further, when the charged particles produced by the incident X-Rays directly ionizes the DNA, the damage is said to be caused by the direct action. In contrast, in indirect action these charged particles can end up interacting

with water molecules to produce highly reactive hydroxyl radicals which can then attack the DNA molecule to cause biological damage. Figure 1.2 gives a visual representation of the direct and indirect action of the X-Rays.

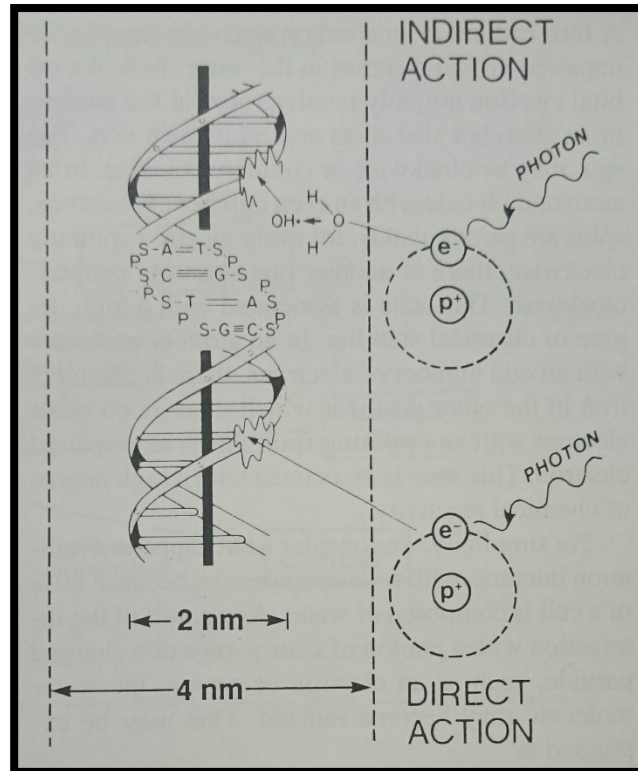


*Figure 1.2: Direct and Indirect action of radiation [1]*

The probability of direct or indirect action of the radiation is influenced by a parameter called linear energy transfer (LET). LET can be defined as the “rate of energy transfer per unit distance along a charged-particle track” [3] Mathematically LET can be defined as per equation 1.1.

$$LET = -\frac{dE}{dx} \quad [1.1]$$

Where  $dE$  is the “Average energy locally imparted” to a medium by a charged particle in traversing a distance  $dx$  [3]. Ionizing radiation with higher LET values tend to produce biological effects predominantly via the direct action as opposed to lower LET radiation that interacts predominantly via the indirect action. Protons or an ion beam are examples of high LET radiation while X-Rays or beta particles are example of low LET radiation. Figure 1.3 compares the stopping power for different radiation types and as evident from the graph, heavy ions like oxygen ion tend to have higher stopping power compared to an alpha particle. Similarly, electrons have significantly lower stopping power as compared to alpha particles. It should be noted that the term stopping power is closely related to LET and gives a good approximation of the measure of LET values. The term stopping power is explained in more detail in section 3.2.

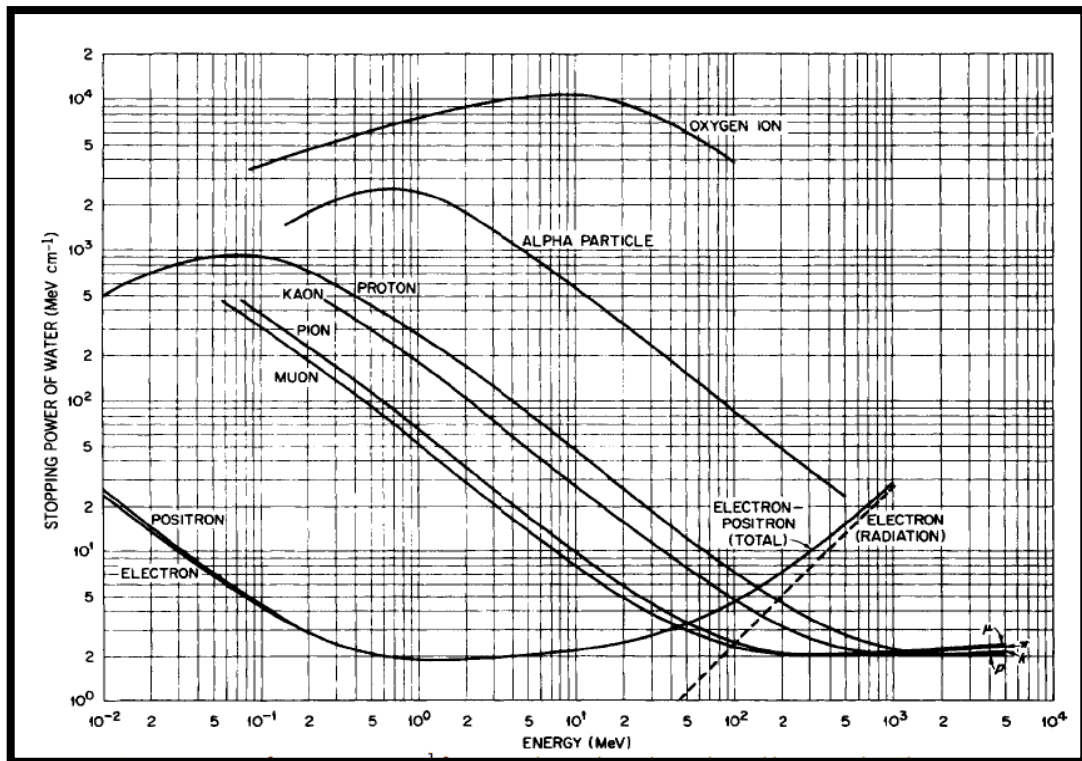


*Figure 1.3: Low LET vs. High LET radiations [3]*

## 1.2 Relative Biological Effectiveness

The American Association of Physicists in Medicine (AAPM), defines Relative Biological Effectiveness (RBE) as “the ratio of the doses required by two radiations to cause the same level of effect. Thus, the RBE depends on the dose and the biological end point” [4]. Mathematically, RBE can be defined as the following:

$$RBE = \frac{Dose(Reference)}{Dose(Test)} \quad [1.2]$$

The term relative biological effectiveness is an important parameter that indicates that different types of radiation produce different levels of biological effect for the same given dose. For example, alpha radiation would require a lower amount of dose to induce the same ‘damage’ as compared to X-Rays (as illustrated in Figure 1.4). Therefore, one can find the RBE of the beam as long as the dose required to reach the same biological end point from two different radiation types is known.

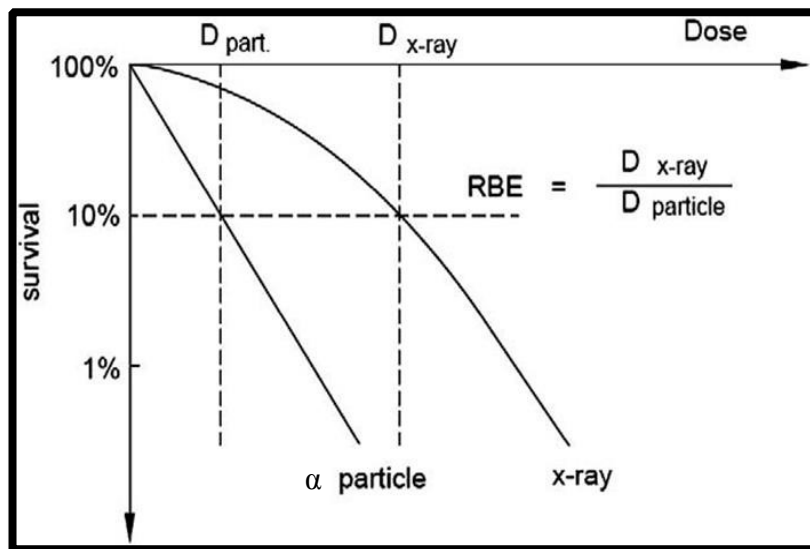


*Figure 1.4: Graph representing the concept of relative biological effectiveness [5]*

RBE is closely related to another quantity defined as the radiation weighing factor. Radiation weighing factor ( $W_R$ ) is defined as the quality factor used to characterize a specific type of radiation. It is used along with the absorbed dose to find the equivalent dose for a given type of radiation. The reason why it is necessary to incorporate the radiation weighing factors to find the equivalent dose is because different radiation types tend to have different levels of biological effects for the same absorbed energy. The value for radiation quality factor increases with the increase in LET of the beam. These quality factors for different radiation types are summarized in Table 1.1 [6].

*Table 1.1: Radiation Weighing Factors [6]*

<i>Type and Energy Range</i>	<i>Radiation Weighing Factor, <math>W_R</math></i>
Photons, all energies	1
Electrons and muons, all energies	1
Neutrons, energy <10 keV	5
10 keV to 100 keV	10
>100 keV to 2 MeV	20
>2 MeV to 20 MeV	10
>20 MeV	5
Protons, other than recoil protons, energy > 2 MeV	5
Alpha particles, fission fragments, heavy nuclei	20

International Commission on Radiation Protection (ICRP) publication 60 defines equivalent dose ( $H_{T,R}$ ) as “the absorbed dose  $D_{T,R}$  averaged over a tissue or organ T due to

radiation R multiplied by a radiation weighting factor  $W_R$ ” [6]. Mathematically, equivalent dose can be defined as following:

$$(Equivalent\ Dose) = (Absorbed\ Dose) * (Radiation\ Weighting\ Factor) \quad [1.3]$$

Based on equation 1.3 it is evident that for a given absorbed dose different radiation types would produce different equivalent doses and hence different levels of biological effects. For example, alphas would produce a higher equivalent dose for a given absorbed dose as compared to protons or electrons. Therefore, the radiation quality factor gives a direct measure of the relative biological effectiveness of the beam and is important in establishing the biological impact of a given radiation type. Tritium is an example of low energy beta emitter, for which previous studies have suggested an RBE value of greater than 1 (see Chapter 3 for more details). Tritium being an isotope of hydrogen has physical properties similar to hydrogen and is found predominantly in the form of tritiated water in the environment. Due to its low range of 6 mm in air, tritium cannot directly penetrate through the skin but can be ingested in the form of water vapour from the air. Once ingested, tritium can interact with biological material similar to a hydrogen molecule and impart its energy to the surrounding tissue by decaying to helium with the emission of a beta particle. Therefore, it is important to quantify the  $W_R$  factor of low energy electrons like those emitted in beta decay of tritium to accurately measure the equivalent dose imparted by them. The following chapters (2 and 3) provide further details into the properties of tritium and its energy distribution.

## CHAPTER-2

### THESIS OBJECTIVES

#### 2.1 Proposal and Objectives

Tritium is a matter of concern in occupational radiation protection in CANDU plants as well as for the environment. Due to the complexities associated with handling tritium in liquid or gaseous state, alternative methods to simulate tritium irradiation are being investigated. In this project it is proposed to use a miniature X-Ray machine from Amptek to produce a surrogate beam that would mimic the beta-decay spectrum of tritium and carry out a dosimetric characterization of this beam.

Tritium decays via beta decay with an average energy of 5.7 keV and maximum energy of 18.6 keV. The beta decay spectrum of tritium can be seen in Figure 2.1.

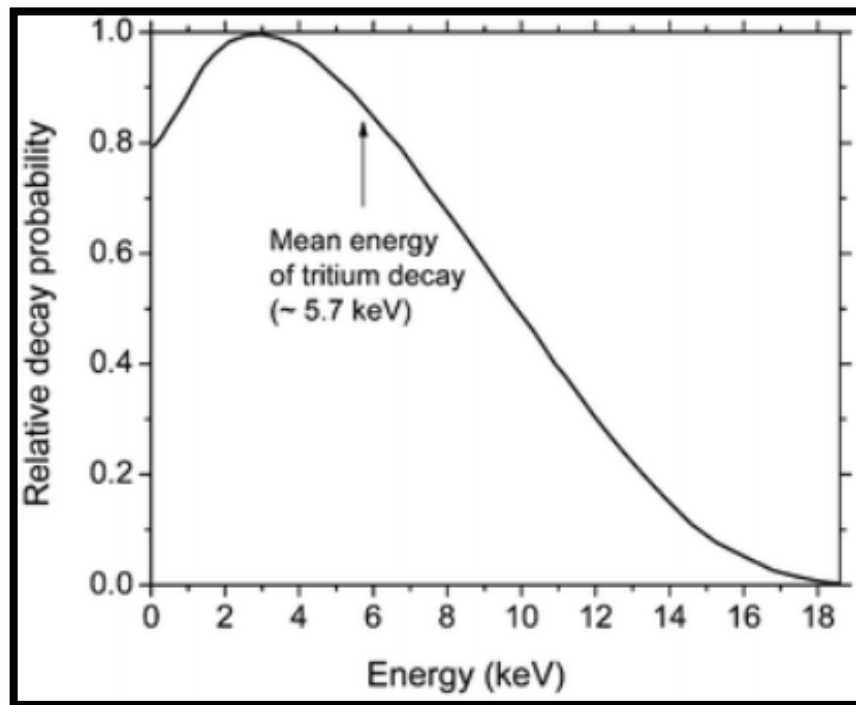


*Figure 2.1: Tritium Beta Decay Spectrum [7]*

As evident from the spectrum in Figure 2.1, tritium has a continuous spectrum typical of a beta decay. Through this project it is aimed to produce a similar radiation field using Amptek's miniature X-Ray machine (Mini-X) that uses a silver target to produce X-Rays. The miniature X-Ray machine allows the production of X-Ray beams of varying energies and the output of the Mini-X at different high voltages can be seen in Figure 2.2. Based on the graph in Figure 2.2, it can be seen that at energies of 10 and 20 keV Mini-X produces average energies similar to that of tritium.

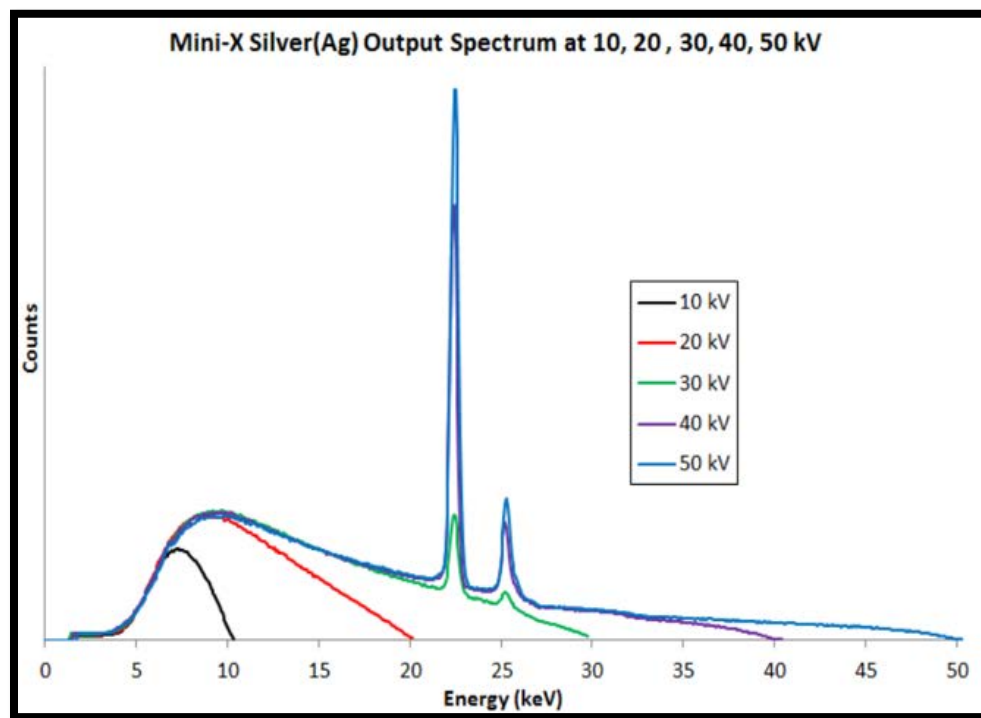


*Figure 2.2: Typical Mini-X output at varying high voltages [8]*

The objective of this work was to design and construct a low photon irradiation facility that would mimic low energy betas, like those emitted in tritium. The experimental facility was to be designed and built such that it could be used to safely characterize the X-Ray source and also be used for the proposed biophysics experiments in the future. As a part of the characterization process, low energy X-Ray beams were to be characterized

using Gafchromic's XR-QA2 radiochromic and a Standard Imaging A-20 ionization chamber. It should be noted that for the characterization experiments, beams of energies between 10 keV-20 keV were of interest since they produce similar average energies as that of tritium. Lastly, a cross calibration curve was to be established between the A-20 ionization chamber and Landauer's OSL nanoDots<sup>1</sup> since nanoDots will be used as the dosimeter of choice for a proposed future biophysics experiment. It should be noted that Landauer's OSL nanoDots are not an absolute method of dosimetry hence, they need to be calibrated against an absolute dosimeter such as, the A-20 ionization chamber. To summarize the main objectives of this project include:

- The design and construction of an experimental irradiation facility that could be used as a substitute for low energy betas by using low energy photons. The experimental facility was to be designed such that it could be used to safely perform characterization experiments and also be used for the future biophysics experiments. In addition, the experimental facility was to be built such that the radiation leakage from the facility was well within the regulatory limits.
- Characterization of low energy X-Ray beams suitable for biophysics experiments using Gafchromic's XR-QA2 radiochromic film and Standard Imaging's A-20 ionization chamber. As a part of the characterization process parameters such as beam dimensions, beam uniformity and dose rates were to be explored.
- Lastly, a cross-calibration curve was to be established between an absolute method of dosimetry, such as an ionization chamber and a more practical method of dosimetry that might be employed in an actual biophysics experiment.

---

1. OSL nanoDots is the trade name of the dosimeter.

## 2.2 Outline of Thesis

This thesis explores the use of a miniature X-Ray source to produce low energy electrons. The work was focused on designing and building an experimental facility that would safely house the X-Ray source along with the detectors required to characterize the X-Ray beams. The experimental facility designed will be used in the future to execute biophysics experiments to establish the RBE of this X-Ray source. Chapter 1 introduces the concepts of radiation quality factor and RBE and defines how this factor changes for different radiation types. It also introduces tritium, a low energy beta emitter and underlines how  $W_R$  factor is important in measuring the biological impact this radiation type. Chapter 2 defines the scope and objectives of this work and also identifies the problems associated with the use of tritium for biophysics experiments. The background theory behind the proposal will be discussed in chapter 3 and this chapter will explain how low energy photons can be used to produce low energy betas/electrons. Chapter 3 also discusses the principle interaction mechanisms of low energy photons with matter and also defines the concept of stopping power and its relationship to the  $W_R$  factor. The materials and methods chapter (Chapter 4) will discuss in detail the X-Ray source and the detectors used to characterize the X-Ray source. In addition, the methodology used to characterize the X-Ray source is also discussed. Chapter 5 will cover in detail the experimental facility built for this project. The results obtained from the characterization experiments will be discussed in detail in chapter 6. Finally, the conclusions will be drawn in chapter 7 along with the suggestions for future work.

## CHAPTER-3

### THEORETICAL BACKGROUND

#### 3.1 Tritium and Low Energy Beta Particles

The ultimate goal of this project was to provide an experimental facility to find the relative biological effectiveness of low energy electrons and beta particles. The resultant RBE value would then be used to establish a comparison with the radiation weighing factor for low energy electrons as set by the ICRP. Tritium is one such example of a beta emitter that decays via a beta-decay process (produces electrons) with the maximum energy of 18.6 keV and an average energy of 5.7 keV. The decay equation for tritium is shown as below:



The determination of RBE for low energy beta emitters and electrons is of importance because there is some evidence to suggest that the RBE value for low energy beta emitters could be more than 1. Based on the experimental studies done by Nikjoo and Goodhead it was concluded that RBE of tritium varies between 2 to 3 relative to  ${}^{60}\text{Co}$  gammas [9]. It was also suggested that other radiation sources with similar energies could also exhibit similar RBE values. As a part of their study it was also concluded that roughly seventy five percent of the total absorbed dose from tritium is deposited by interactions of energies below 5 keV [9]. The reasoning behind a possible increase in RBE value is that low energy beta particles or electrons have higher stopping power as compared to higher energy electrons and as such, lower energy electrons tend to have a greater ionization density. Due to their higher ionization density, lower energy electrons can form more ion pairs per unit distance in a given medium and as such they produce a larger cluster of

interactions [10]. On a biological level, this larger cluster of interactions would lead to an increased frequency and complexity of DNA damage since higher density of single strand and double strand breaks would occur. The heightened formation of DNA strand breaks might increase the chances of DNA mis-repair and ultimately result in mutations [10]. Hence, it is believed that lower energy electrons might be more effective per unit dose as compared to higher energy electrons.

As stated earlier, the term stopping power is related closely to linear energy transfer and it describes the rate of energy loss for a particle along its track. Since stopping power is inversely dependent upon the speed of the particle, it makes intuitive sense that a particle with lower velocity would lose energy more rapidly and hence have higher stopping power values. The linear stopping power  $S$  “for charged particles in a given absorber is defined by the differential energy loss for that particle within the differential path length” [11]. Mathematically, this can be defined by:

$$S = -\frac{dE}{dx} \quad [3.2]$$

Here, the differential energy loss over the differential path length is also referred to as the specific energy loss and the stopping power formula for fast electrons is defined by equation 3.3 [11].

$$-\left(\frac{dE}{dx}\right) = \frac{2\pi e^4 NZ}{mv^2} \left( \frac{\ln mv^2 E}{2I^2(1-\beta^2)} - (\ln 2) 2\sqrt{1-\beta^2} - 1 + \beta^2 \right) + (1-\beta^2) + \frac{1}{8}(-\sqrt{1-\beta^2})^2 \quad [3.3]$$

This formula describes the specific energy loss for the electrons that occurs during the excitation and ionization events and Equation 3.3 is also referred to as the collisional

stopping power for electrons. Here  $v$  represents the velocity of the fast electron while  $N$  and  $Z$  represent the number density and atomic number of the absorber atoms and  $I$  represents the average excitation and ionization potential of the absorber. In addition, the term  $\beta$  represents the speed of a particle relative to the speed of light [11].

It should be noted that for electrons, energy loss can also take place in forms of radiative processes in addition to the collisional losses as defined by equation 3.3. These “radiative energy losses can take place in form of bremsstrahlung or electromagnetic radiation that can emanate from any position along the electrons track” [11]. Therefore, the total stopping power for an electron is the sum total of its collisional and radiative stopping powers. However, in the context of this report it is not important to define the radiative stopping power, since the key idea to extract from equation 3.3 is that energy deposited locally by fast electrons increases with decrease in electron velocity. Thus in principle, lower energy electrons would be expected to have higher stopping powers since energy of an electron is directly proportional to its velocity. To elaborate further, the relationship between the total stopping power and electron’s energy is summarized in Figure 3.1 (next page). As evident from the graph the stopping power of an electron in tissue decreases quite significantly as its energy increases from  $10^{-2}$  MeV to 1 MeV. The term stopping power is measured in terms of  $(\text{MeV cm}^2)/\text{g}$  and this graph was obtained from NIST and the raw data for this graph is given in Appendix-A [12].

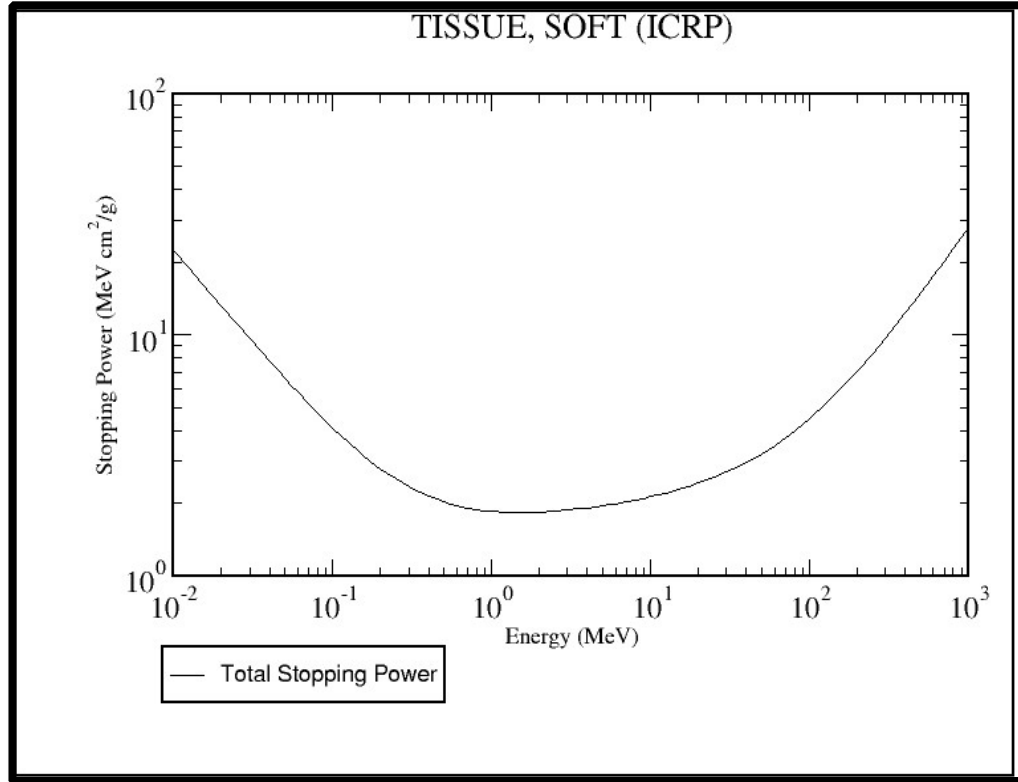


*Figure 3.1: Total Stopping Power vs. Energy for electrons [12]*

Therefore, it is being hypothesized that lower energy electrons/beta particles would have an RBE that would suggest  $W_R$  values of more than 1, contrary to what is currently accepted. The direct use of a low energy beta emitter like tritium for making biophysical measurements has a number of difficulties mainly associated with the fact that tritium is either in the form of a radioactive gas or as tritiated water vapour, hence it is difficult to manage and quantify the exposure. It is proposed that a low energy X-Ray source be used. This X-Ray source would mimic the beta decay spectrum of Tritium by producing photoelectrons upon their interaction with biological tissue with average energies similar to that of tritium/beta particles.

### 3.2 Photon Interaction with Matter

X-Rays are photons that can produce photoelectrons upon interaction with water or biological tissue. Photons can interact with matter via three different processes and these interactions are energy dependent as shown in the figure below.

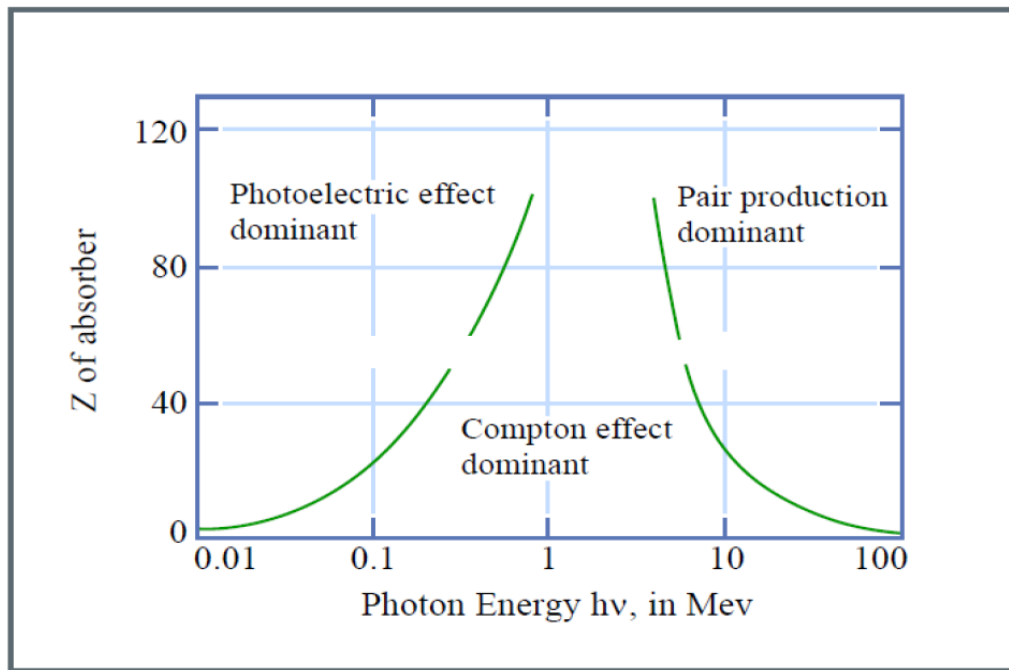


*Figure 3.2: Photon Interaction with Water [8]*

As evident from Figure 1.6, the photoelectric effect dominates for low energy photon interactions with matter while the Compton effect or Compton scattering dominates for intermediate energies and pair production dominates for higher energy photons. Since, for the sake of this project, only maximum X-Ray energies of 20 or 25 keV will be used with low atomic number materials, the photoelectric effect would be the dominant mode of interaction. The binding energy for an electron bound to a water molecule is 12.6 eV, which is approximately a thousand times smaller than the energies used in this project [8]. The

photoelectric effect, as the name suggests is a phenomenon where a target material emits electrons upon its interaction with photons. If the energy of the incoming photon is more than the binding energy of the electron, a photoelectron is produced. The energy of this photoelectron is equal to the difference between the energies of incident photons and the binding energy of the target electron. As stated earlier the energy of the photons used in the experiment is 1000 times higher than the binding energy of the electron bound to the water molecule. Therefore, the energy of the photoelectron would be approximately similar to that of the incident photon. Hence, it can be inferred that the photoelectron spectrum within a biological tissue would be approximately similar to that of the incident photon spectrum [8].

In addition to photoelectric effect, compton scattering is also of interest since lower energy photons can interact with matter via compton scattering as well. Compton scattering is a phenomenon in which a photon scatters after interacting with an atomic electron. In this process the incident photon transfers part of its energy to atomic electron to produce a recoil electron and scatters with an energy as defined in equation 3.4 [8].

$$E' = \frac{E}{1 + \left(\frac{E}{mc^2}\right)(1 - \cos \theta)} \quad [3.4]$$

Here  $E'$  represents the energy of the scattered photon while the  $E$  represents the energy of the incident photon and  $\theta$  represents the angle at which the photon scatters. Furthermore,  $m$  represents the rest mass of an electron and  $c$  is the speed of light. The energy lost by incident photons is transferred to recoil electrons hence, low energy electrons can be produced via the compton effect for low energy photon interaction with matter [8]. To give an example, the scattered photon would have a maximum energy when  $\theta$  is  $90^\circ$  and

minimum energy when  $\theta$  is  $180^\circ$ . Therefore, if an incident photon of 10 keV scatters at an angle of  $180^\circ$ , the scattered photon would have an energy of 9.62 keV and a recoil electron with an energy of 0.38 keV would be produced. However, as shown in figure 3.3 the Compton interaction cross section in water is significantly lower than photoelectric interaction cross section. Therefore, the bulk of the recoil electrons produced would be produced via the photoelectric effect with a small amount of electrons produced from Compton scattering.

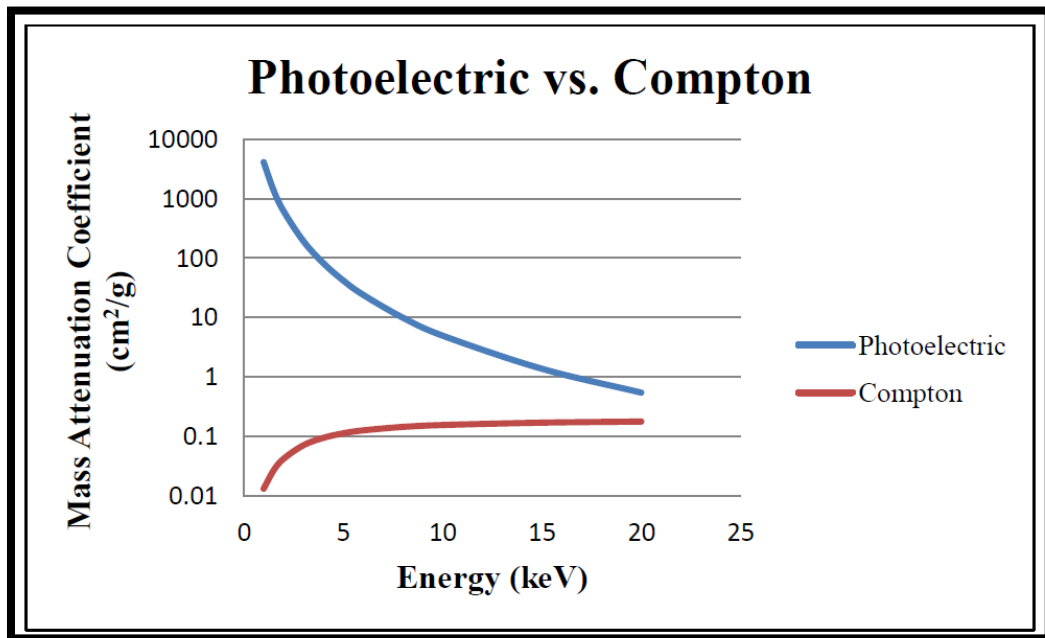


*Figure 3.3: Photoelectric vs. Compton interaction cross sections in water for low energy photons [8]*

Photoelectrons owing to their charged nature can produce a biological effect by ionizing the medium they traverse in exactly the same manner as beta particles emitted within a tissue. Figures 3.4 and 3.5 elaborate further on how a similar X-Ray and photoelectron spectra can be expected. These results were obtained from a preliminary

study done at UOIT and Figure 3.4 shows how the 20-keV Mini-X spectrum compares with the beta decay spectrum of tritium [8]. The photoelectron (electron) spectrum in Figure 3.5 was simulated using Monte Carlo N-Particle code (MCNP) and represents the spectrum that would be obtained after the incident X-Ray photons (20 keV) interacted with a 2mm slab of water. As evident from the Figures 3.4 and 3.5, the simulated electron spectrum is in very good agreement with the Mini-X spectrum. Therefore, based on these preliminary results it is to be believed that similar results can be reproduced experimentally and the photoelectron spectrum produced after X-Ray interaction with biological tissue would be almost identical to that of incident X-Ray photon spectrum. Thus it can be said that the Mini-X would provide a good alternative for producing low energy electrons since photons upon interacting with the target matter would produce low energy electrons throughout the medium and these electrons would bring about biological damage just like the low energy electrons emitted in beta decay of tritium [8].

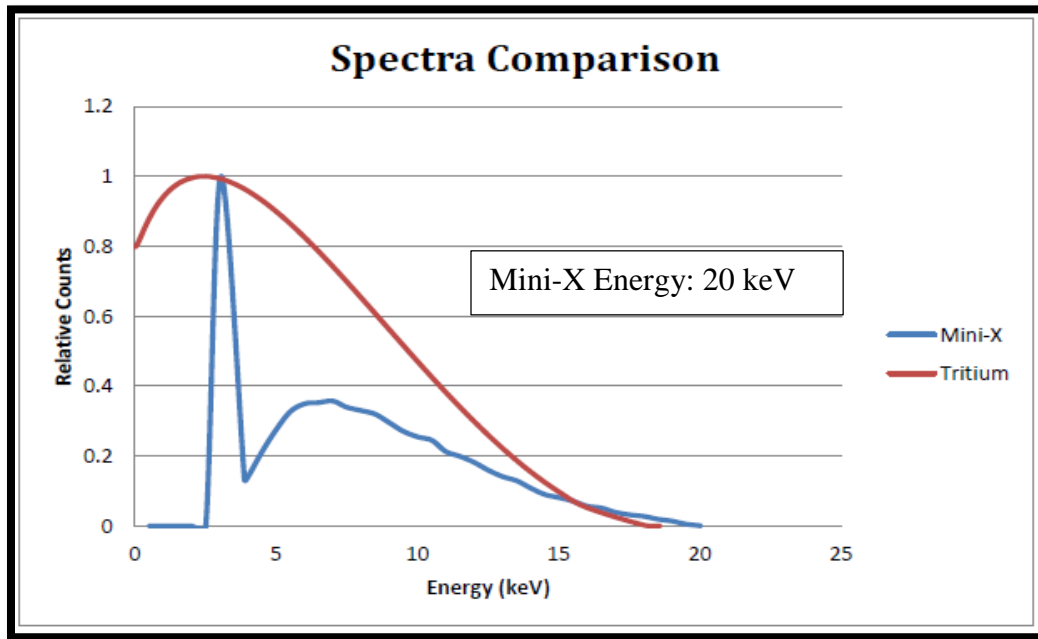


*Figure 3.4: Spectra Comparison between Mini-X and Tritium [8]*

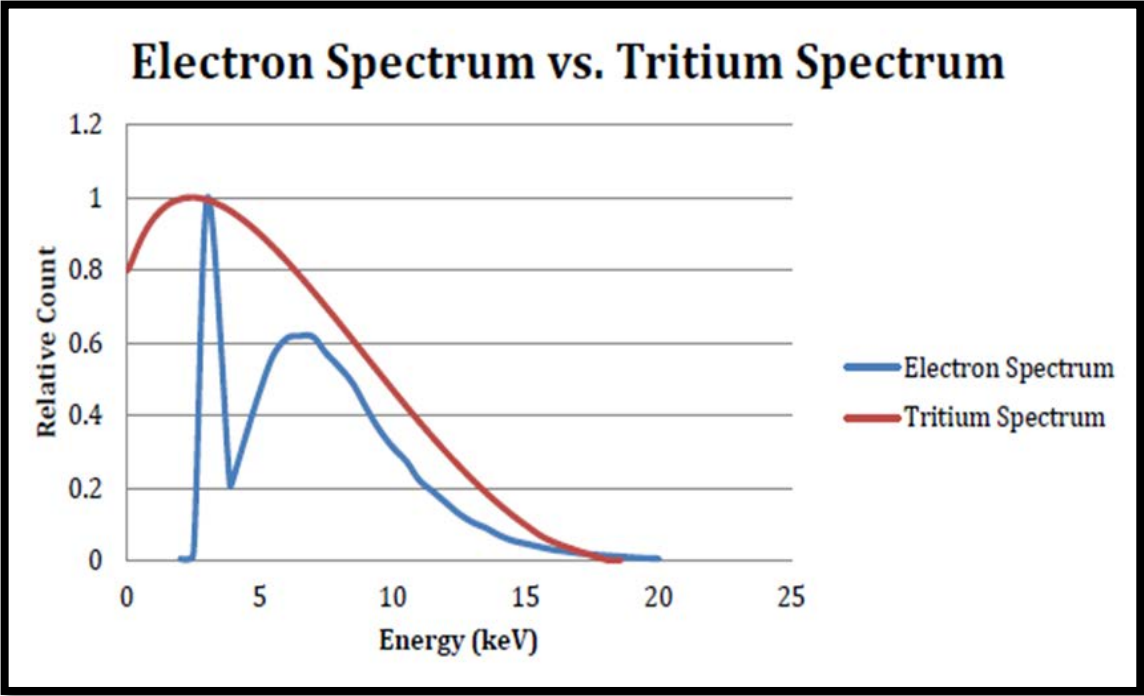


*Figure 3.5: Spectra comparison between Tritium and simulated electron spectrum [8]*

## CHAPTER-4

### MATERIALS AND METHODS

#### 4.1 X-Ray Source

To produce X-Rays, electrons are accelerated using a high voltage onto a target metal. These electrons produce X-Rays as they are brought to a stop by the target metal. The type of X-Rays produced by this sudden braking of the electrons is referred to as Bremsstrahlung or braking radiation. Another type of X-Ray produced in the process (as a result of electron transitions) within the atom are referred to as Characteristic X-Ray [13]. Figure 4.1 shows a schematic of a typical X-Ray tube.

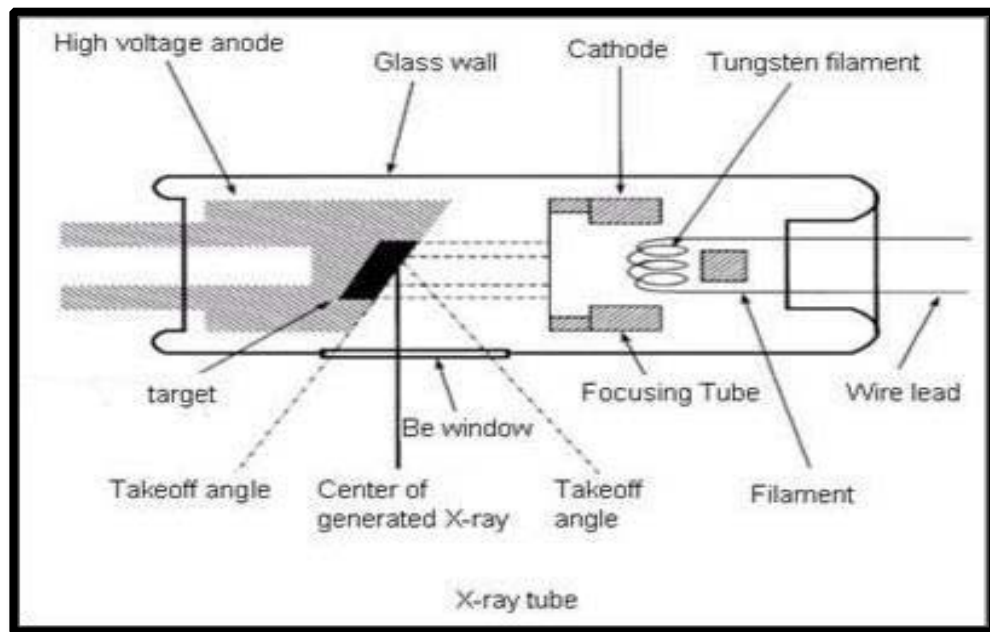


*Figure 4.1: Schematic of a modern day X-Ray tube [8]*

Characteristic X-Rays are produced when the electrons have sufficient energy to remove an electron from the atomic shell of the target atom. The vacant spot in the atomic

shell is often taken by an electron from another shell resulting in production of X-Rays that is characteristic of the target metal. For example, when an electron falls from the L-shell to K-shell the resultant X-Ray would have an energy equal to the energy difference between the energy levels. The transition that involves an electron falling from the L-shell to K-shell results in production of K-alpha X-Ray. Similarly, if electron transitions from M-shell to K-shell, K-Beta X-Ray is produced. This concept is further illustrated in Figure 4.2.

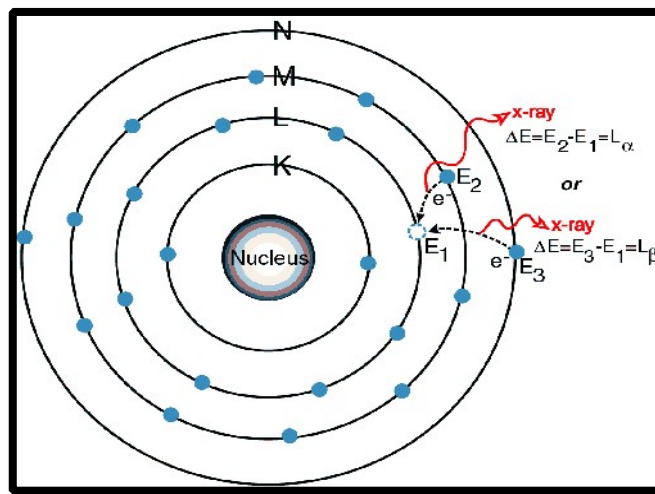


*Figure 4.2: Production of Characteristic X-Rays [14]*

For example, if an accelerated electron removes an electron from the K shell of the atom (energy of  $E_0$ ), an electron from L shell with an energy of  $E_1$  would take its place thereby resulting in production of X-Ray with net energy given by the following formula [14]:

$$E_{X-Ray} = E_1 - E_0 = K\text{-Alpha} \quad [4.1]$$

It should be noted that in addition to accelerated electrons, the K-shell vacancies can also be caused by bremsstrahlung photons since they can carry enough energy to remove an electron from the K-shell of the atomic orbit. The X-Rays that carry the energy

as specified in equation 4.1 contribute to the K-Alpha line seen on the spectrum, since these energies are characteristic to a specific transition of electrons.

The Mini-X X-Ray source produces X-Rays using similar concepts as explained above with silver as the target metal. The Mini-X is a first of its kind X-Ray tube that uses a compact, self-contained design and is controlled via an attached computer using an usb interface (see Figure 4.3). The Mini-X was designed to replace radioisotopes for X-Ray fluorescence applications and can be operated within tube voltage range of 10 kV to 40 kV while the tube current can be varied from 5  $\mu$ A to 200  $\mu$ A [15].



*Figure 4.3: Mini-X X-Ray Tube [8]*

As stated earlier, the Mini-X is controlled by a computer usb interface which adds to the safety features of the Mini-X. The device cannot be operated unless the software is loaded onto the attached computer and all the necessary attachments are made. In addition to this, the Mini-X also has a built in interlock that prevents the production of X-Rays while the interlock is open. In other words pin 1 and 2 on the interlock must be in contact for the Mini-X to produce X-Rays (see Figure 4.4). Apart from this, the Mini-X also has a built in 'beeper' with flashing LED which beeps while the X-Ray machine is in use. The X-Ray machine comes with a three tier built-in safety system to ensure the safety of the operating

personnel at all time. In addition, the machine uses an air-cooling system and can be operated within a temperature range of -10 °C and 60 °C [15]. The flashing LED/beeper, USB port, Interlock, and the power outlet on the Mini-X can be seen in Figure 4.4.



*Figure 4.4: Back Panel of Mini-X showing Interlock and Flashing LED/Beeper on*

*Mini- X [8]*

The Mini-X is capable of producing an output flux of  $10^6$  counts per second/mm<sup>2</sup> on the axis at a distance of 30 cm with operating parameters of 50 keV and 1  $\mu$ A. The X-Ray tube is capable of producing a uniform beam with a 120° cone as shown in Figure 4.5. The Mini-X also includes a 2 mm collimator that can reduce the X-Ray cone to 5° [15]. For this project additional collimators with diameters of 2.5, 3.0 and 3.5 mm were also fabricated.

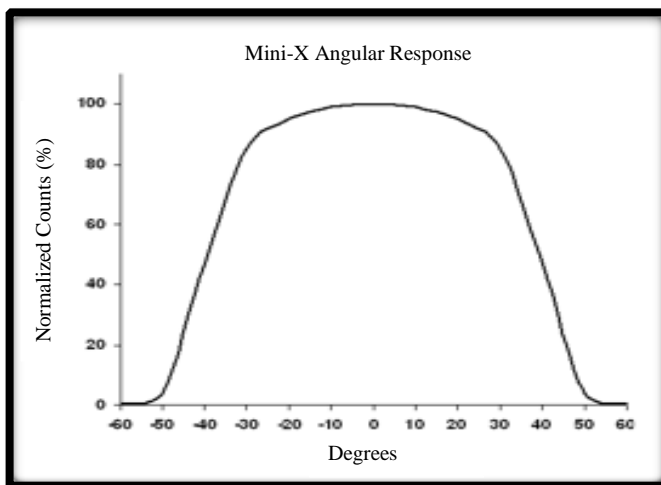


*Figure 4.5: Angular Response of Mini-X [15]*

Since the Mini-X uses a silver target it produces characteristic X-Rays at energies of 22.1 keV and 24.9 keV as well as a continuous bremsstrahlung spectrum. Figure 4.6, clearly shows the two characteristic lines on the Mini-X spectrum where the first K-alpha line represents a 22.1 keV peak, while the K-Beta line represents the 24.9 keV peak. Figure 4.7 shows the screenshot of the Mini-X controller used to control the output parameters of the X-Ray beam.

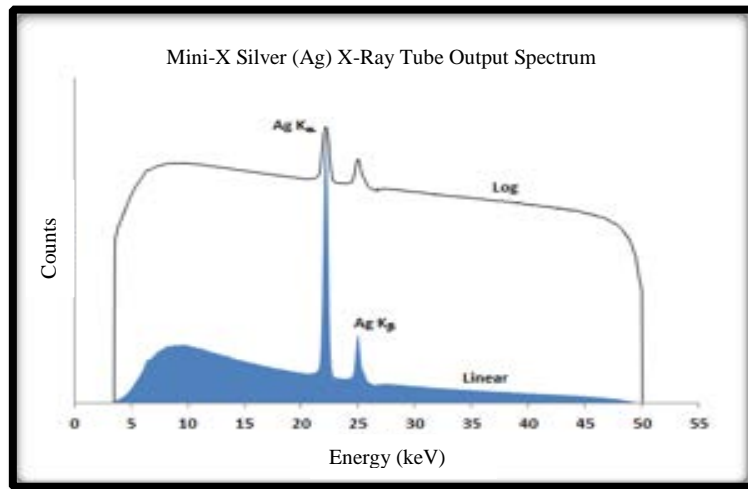


*Figure 4.6: Amptek Mini-X Spectrum at 50 kV [15]*

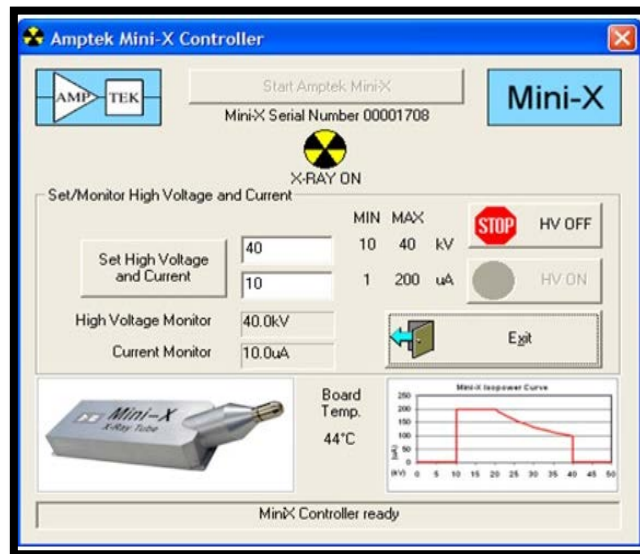


*Figure 4.7: Screenshot of the controller's panel of the Mini-X [15]*

## 4.2 Detectors

### 4.2.1 The X-123 Spectrometer

The X-123 spectrometer from Amptek was the detector of choice for the spectrometry applications required for this project. The spectrometer uses a silicon-pn detector and like the Mini-X it also consists of a compact design that allows the spectrometer to fit comfortably in your hand. Figure 4.8 further illustrates the compact design of X-123 spectrometer.



*Figure 4.8: The X-123 spectrometer [16]*

The spectrometer consists of the X-Ray detector and its charge sensitive pre-amplifier along with the digital pulse processor, MCA and the power supply all in one compact design and connects to the computer via a USB interface (see Figure 4.8). Also, the spectrometer is ideal for X-Ray fluorescence applications and is sensitive to the X-Ray energies used for this project [16].

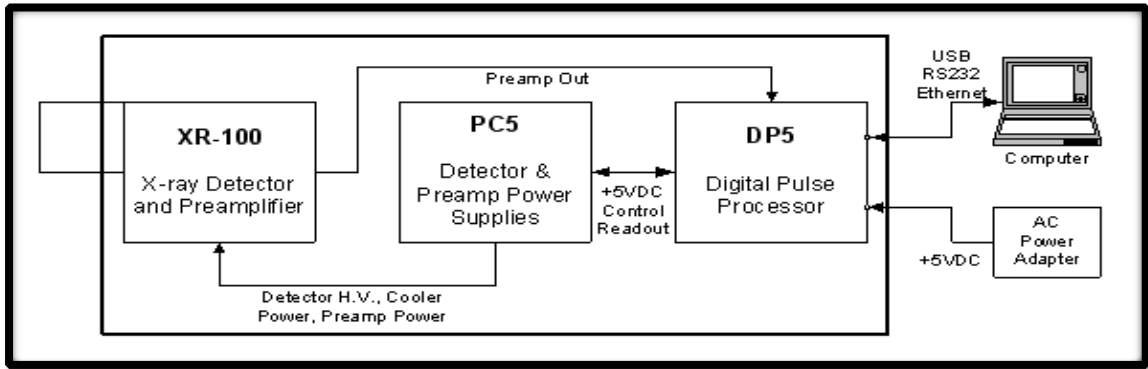


*Figure 4.9: Connection diagram and schematic for the X-123 spectrometer [16]*

The spectrometer has a resolution of 145 to 260 eV FWHM at 5.9 keV and the resolution depends upon parameters like peaking time and temperature. The detector consists of a thin Beryllium window with thickness of 12.5  $\mu\text{m}$  and it is imperative not to touch the thin Beryllium window since it is extremely prone to damage and very fragile. In addition, the detector can accept a maximum count rate of  $2 * 10^6$  cps and is sensitive to energies in the range of 1 keV to 40 keV. Figure 4.10 shows the typical output obtained from X-123 spectrometer using Fe-55 source.

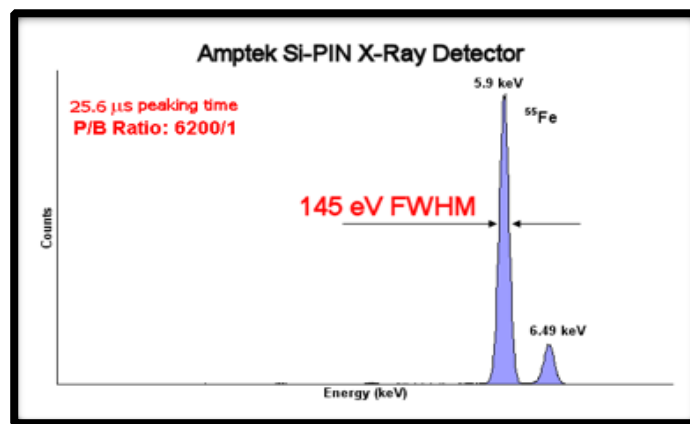


*Figure 4.10: Energy Resolution of the X-123 spectrometer [16]*

The spectrometer was calibrated using Americium-241 and the calibration data is shown in Table 4.1.

Table 4.1: Calibration Data for the X-123 spectrometer

Index	Channel	Energy (keV)	Calibration Equation
1	137	13.95	Energy=0.1023*Channel Number
2	174	17.74	
3	204	21.00	
4	257	26.00	
5	581	59.54	

Figures 4.11 and 4.12 show the spectra obtained from Americium-241 and Fe-55, respectively. As evident from Figure 4.11, the Americium-241 spectrum gives a higher number of peaks over a broader energy range which makes it ideal for the calibration purposes.

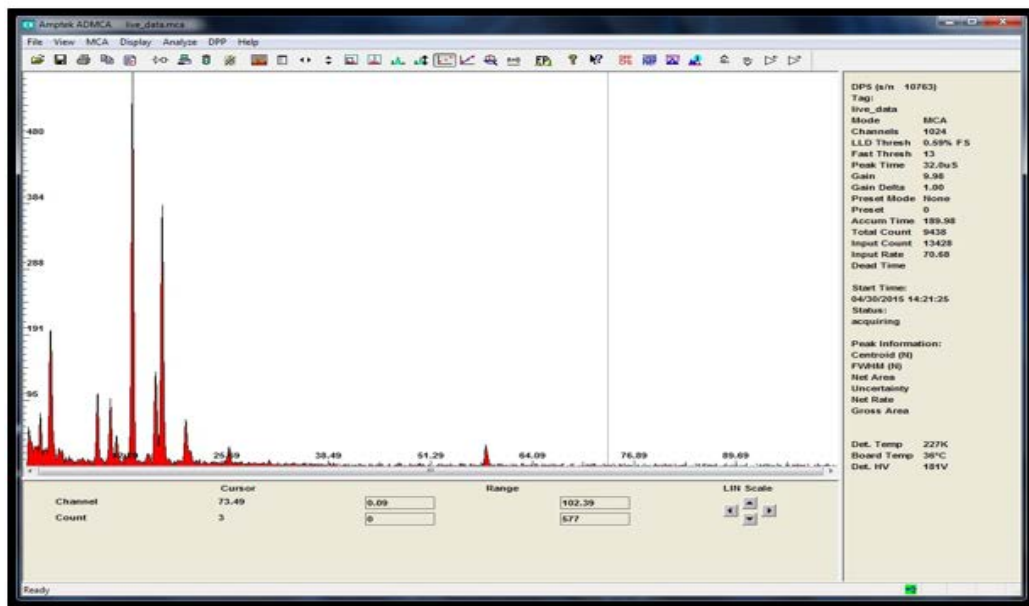
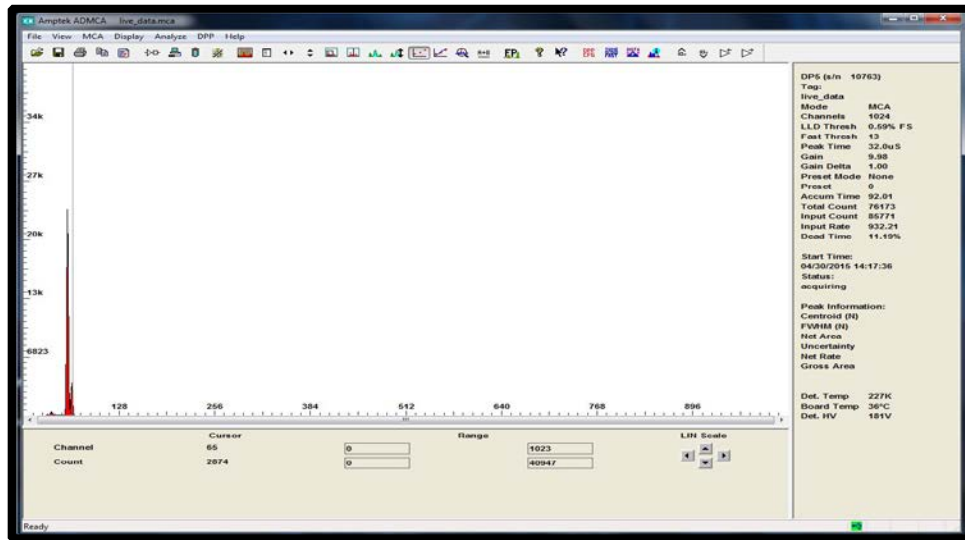


Figure 4.11: Americium-241 spectrum as measured by the X-123 spectrometer



*Figure 4.12: Iron-55 spectrum as measured by the X-123 spectrometer*

Figure 4.13 shows the energy calibration curve for the spectrometer and shows a linear relationship between channel number and energy. The resultant fitted calibration equation obtained from the data is shown in equation 4.2 and it has an  $R^2$  value of 0.9999 which indicates a strong linear relationship between channel number  $x$  and energy  $y$  in keV.

$$y = 0.1023x \quad [4.2]$$

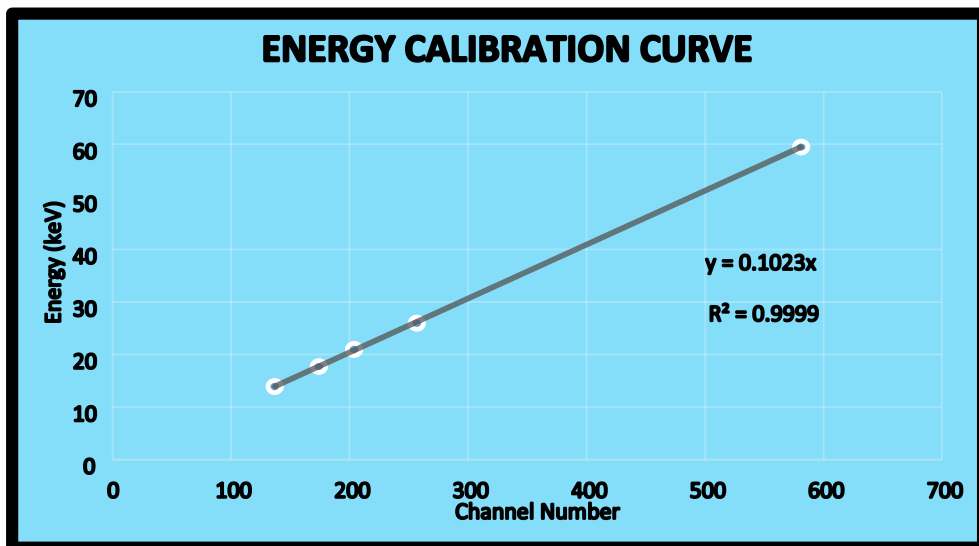


*Figure 4.13: Energy Calibration Curve*

#### 4.2.2 Gafchromic's XR-QA2 Radiochromic film

Radiochromic films are used quite extensively in radiology for quality assurance purposes and the films are ideal for small field dosimetry since they provide high spatial resolution. For example, intensity modulated radiation therapy uses a highly collimated beam, where the beam is made to conform to the shape of the target tumor in order to limit dose to healthy tissue. In such treatment methods, radiochromic film is a useful quality assurance tool since it helps with the verification of the accuracy of the dose delivered to the patient [17].

Radiochromic films were used as a part of the experimental beam characterization of the Mini-X to determine the size and uniformity of the Mini-X beam. After interacting with radiation, radiochromic film undergoes a series of chemical reactions that results in colourization of the film. In addition, the spread of the colourization obtained on the film is a direct indication of the spatial distribution of the incident radiation. The specific type of radiochromic film used in this experiment is called Gafchromic's XR-QA2 radiochromic film which is particularly sensitive to low energy X-Rays used in this study. A schematic of Gafchromic's XR-QA2 film is given in Figure 4.14.

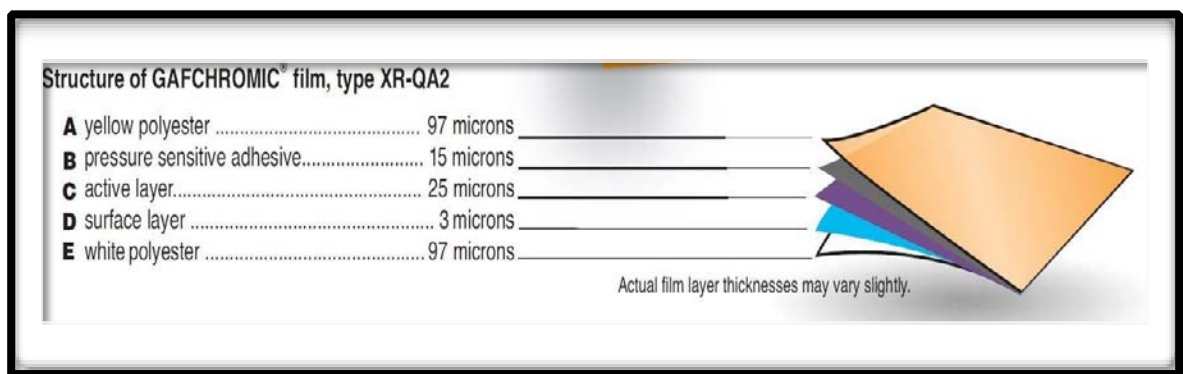


*Figure 4.14: Schematic of the Gafchromic's XR-QA2 film [17]*

The active layer of the film releases a dye upon being exposed to radiation which results in colourization of the film and the exposed film can then be analyzed using any image analysis software to find the exact spatial distribution of the incident radiation. ‘ImageJ’, a freeware image analysis software was used to analyze the exposed radiochromic films and this process is explained in more detail in the next section. As shown in Table 4.2, the film is sensitive to the doses in range between 0.1 cGy and 20 cGy and hence, is ideal for the study undertaken since the dose from the X-Ray source is expected to be within this range [17].

*Table 4.2: Properties of XR-QA2 film [17]*

<i>Dose Range</i>	<i>Energy Range</i>	<i>Configuration</i>	<i>Active Layer Thickness</i>
0.1 cGy to 20 cGy	20 kVp to 200 kVp	3-Layer Laminate substrate active layer substrate	White polyester-97 microns Yellow Polyester-97 microns

Figure 4.15 illustrates how the color of the film changes after being exposed to radiation.

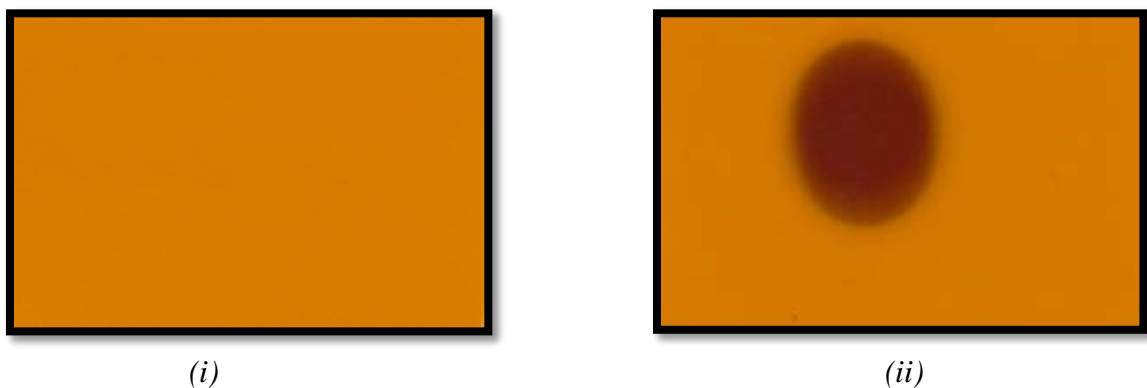


*Figure 4.15: (i) Film before being exposed to radiation (ii) Film after being exposed to radiation*

### 4.2.3 Analyzing Radiochromic films using ImageJ

ImageJ is an image analysis software that was used to analyze the exposed radiochromic films. ImageJ comes with built in commands and functions that allows the user to measure the intensity distribution for a given image. A valuable feature of the radiochromic films is that they can be analyzed using a flatbed scanner which eliminates the need for a commercial densitometer. For the sake of this project a Canon's 8800F scanner was used and all the images were scanned at the highest available resolution of 600 dpi. To ensure optimal results it is critical that the films are placed in the middle of the scanner during the scanning process. After scanning the films, ImageJ can be used to find the intensity distribution of the film which gives a direct indication of the radiation absorbed by the film. To find the intensity distribution of the film, the image is first converted into an 8-bit grayscale image that represents 256 possible shades of gray from black to white. Here, an intensity value of 255 is taken as white which means that all the light passes through the film. While the intensity value of 0 refers to black and is essentially the state where no light passes through the film. To get meaningful information out of this intensity distribution the intensity values were changed to optical density using the formula shown in equation 4.3:

$$\text{Optical Density} = -\log_{10} (I/I_0) \quad [4.3]$$

Here  $I_0$  represents the intensity of the light before it enters the film and  $I$  represents the intensity after it leaves the film. Using this equation and the known values for  $I$  and  $I_0$  as given by ImageJ the optical density distribution can be obtained, which is directly proportional to the dose absorbed by the film. Therefore, higher optical density values mean

higher dose absorbed and vice versa [18]. Figure 4.16, gives an example of the optical density distribution obtained for a given irradiated film.

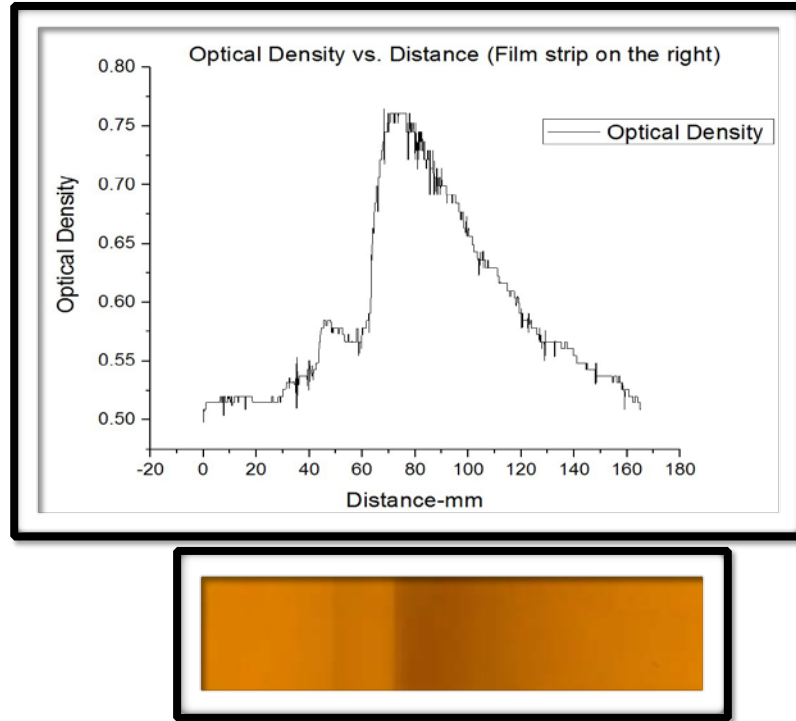


*Figure 4.16: Optical Density distribution for a given irradiated film*

As evident from Figure 4.16, there is a direct correlation between the colour of the film and the corresponding optical density values. Using the known size of the film, ImageJ can also be used to calibrate the number of pixels on the film into distance (example in centimetres) and hence, give us the spatial distribution of the incident radiation on the film. To elaborate further, an un-calibrated optical density distribution curve would give a distribution curve in terms of optical density vs. pixels which fails to provide any useful information as far as image analysis is concerned. Therefore, it is imperative to calibrate the x-axis of the curve using the known image size. As mentioned previously, the intensity values obtained from ImageJ can be converted to optical density and a convenient way of

calibrating intensity for optical density is using a step tablet. According to the suggested calibration technique by ImageJ, a calibrated Kodak step tablet is used with optical density ranging between 0.05 and 3.05 (see Figure 4.17).



*Figure 4.17: Optical Density calibration using step tablet [19]*

This step tablet consists of 21 different steps with a known optical density for each step and using ImageJ the intensity for each individual step can be found and related to its corresponding optical density value. The raw data for this is shown in table 4.3 and the resultant relationship between optical density and intensity can be described by the curve shown in Figure 4.18.

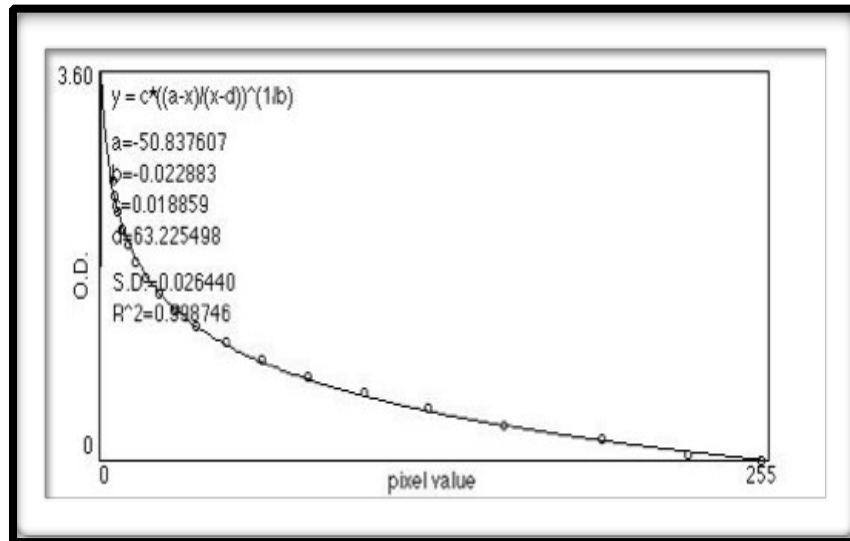


*Figure 4.18: Optical Density calibration curve [19]*

*Table 4.3: Calibration Values for ImageJ [19]*

<i>Intensity (I)</i>	<i>Optical Density</i>
252.37	0.00
224.74	0.06
191.54	0.20
154.19	0.34
125.56	0.49
100.88	0.64
79.41	0.79
61.97	0.94
48.19	1.10
37.10	1.26
29.26	1.41
23.11	1.56
17.90	1.70
14.04	1.85
10.98	2.01
8.69	2.16
7.20	2.32
6.03	2.46
5.15	2.60

It should be noted that radiochromic film is not a method of absolute dosimetry and the films needs to be calibrated against a detector to obtain the net dose absorbed by the film. Since the optical density value is directly proportional to the dose absorbed by the film the optical density values can be calibrated for dose using an ionization chamber or any other calibrated dosimeter. Therefore, upon calibration the spatial distribution of the film can give a direct indication of the dose rate delivered at a given point on the film, thereby making it an excellent tool for beam characterization.

#### 4.2.4 Standard Imaging's A-20 Ionization Chamber and SuperMAX Electrometer

Ionization chambers are gas filled detectors that measure the change created in the medium by the passage of radiation. Ionization chambers differ from other gas filled detectors like Geiger Muller and Proportional counters in the sense that there is no charge multiplication and only the charge generated by incoming radiation is collected. Some of the common fill gases used in ionization chambers include argon, oxygen, air, and methane. This type of detector is ideal for gamma radiation, X-Rays and beta particles as required for this project. The specific type of ionization chamber used for this project is the Exradin's A-20 ionization chamber from Standard Imaging. It is a parallel plate ionization chamber with a collecting volume of  $0.074 \text{ cm}^3$  and collector diameter of 1.93 mm. Figure 4.19 shows the design of a typical parallel plate ionization chamber.

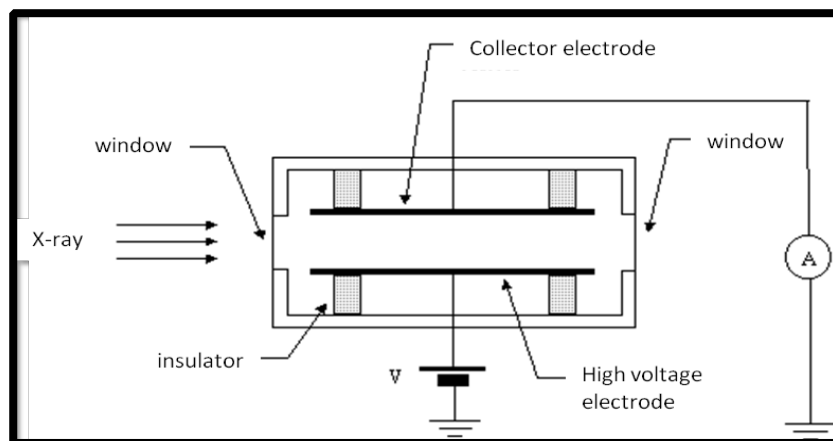


*Figure 4.19: Design of a typical parallel plate ionization chamber [5]*

Incident radiation upon its interaction with the gas medium, creates ion-pairs that can be collected via the use of an electric field. For example, a chamber with air as its gas medium would produce a positive ion and an electron after it interacts with gamma radiation. Some of the electrons combine with the oxygen molecule to produce negatively

charged ions. The positive and negatively charged particles would move towards one of the two electrodes, depending on their charge. Positive ions tend to move towards the cathode while the electrons or negative ions move towards the anode. Electrons move much more rapidly than the ions owing to their relatively smaller mass and it is these ion pairs that form the basis of electric signal from the ionization chamber. The charge produced in the medium can be collected by the application of electric field and the drift velocity of these charged particles is directly related to the applied electric field [21]. The drift velocity for these charged particles is defined by the following equation:

$$V_{drift} = (\mu * E) / p \quad [3.4]$$

Here,  $\mu$  represents the charge mobility and is a parameter that is dependent upon the gas used in the medium while  $E$  represents the electric field and  $p$  represents the gas pressure [21]. The electric field can be increased or decreased by varying the voltage applied between the two electrodes. With an increase in voltage the number of charged particles collected would continue to increase until it hits a saturation point. The increase in electric field ensures that there is little or no loss of charged particles due to the recombination process. Therefore, it is ideal to work at a voltage where all or most of the charged particles are collected. The applied voltage where all the charged particles are collected is referred to as the operating voltage. The operating voltage for Exradin's A-20 chamber as suggested by the manufacturer is 300 V and Figure 4.20 shows the saturation curve for the A-20 ionization chamber. As a mode of precaution, it should be duly noted that a given ionization chamber should not be operated beyond its operating voltage simply because over voltage can cause permanent damage to the chamber.

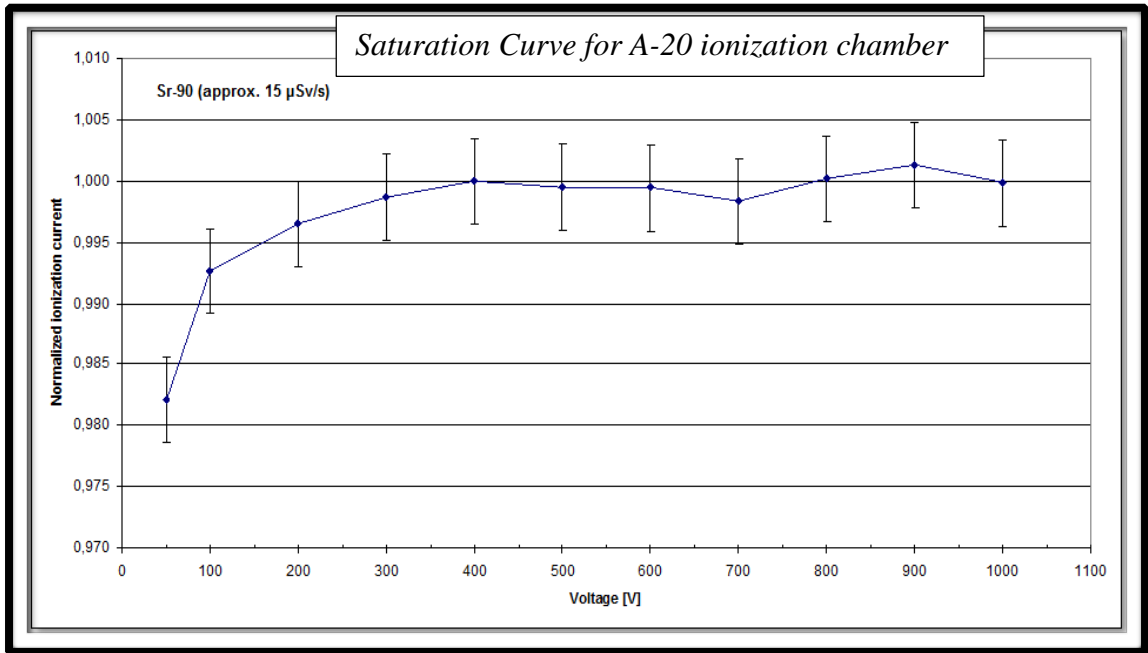


*Figure 4.20: Saturation curve for Exradin’s A-20 ionization chamber [Standard Imaging, Personal Communication, September 2014]*

The high voltage of the ionization chamber is controlled via the attached SuperMAX electrometer. The SuperMAX electrometer has two different channels that can accept two ionization chambers at a given time via a TNC connector. Therefore, high voltage can be applied to different detectors at a given time which can become useful in applications involving cross calibration of two different detectors. The SuperMAX consists of an easy to use touch screen interface that is controlled via a smart pen. The electrometer allows the user to collect charge in three different modes namely: trigger, timed, and continuous modes. In the trigger mode, the user can define the charge thresholds between which the electrometer would operate and the electrometer would automatically start and stop between these ‘charge thresholds’. For example, the user can define the charge range on electrometer to collect charge between 0.1 pA and 10 pA and once the limit of 10 pA is

achieved the electrometer would automatically stop supplying high voltage to the attached ionization chamber. Similarly as the name suggests, in timed collection mode the user can define the time for which the charge would be collected. The range can be set anywhere between 0-600 s. Lastly, in continuous collection mode the charge can be collected for an indefinite period until the user manually stops the charge collection. The SuperMAX allows the user to collect charge in two different modes namely high range and low range. The low range collects current between 0.001-500 pA with 1 pA resolution, while the high range collects current within 0.001-500 nA with 1 nA resolution. It is suggested by the manufacture that the electrometer be operated at the low range for optimal results [22]. Figure, 4.21 shows the display of SuperMAX electrometer and the drop down menus including range, bias and time etc. can be seen clearly on the 16.26 cm LCD display of the SuperMAX.

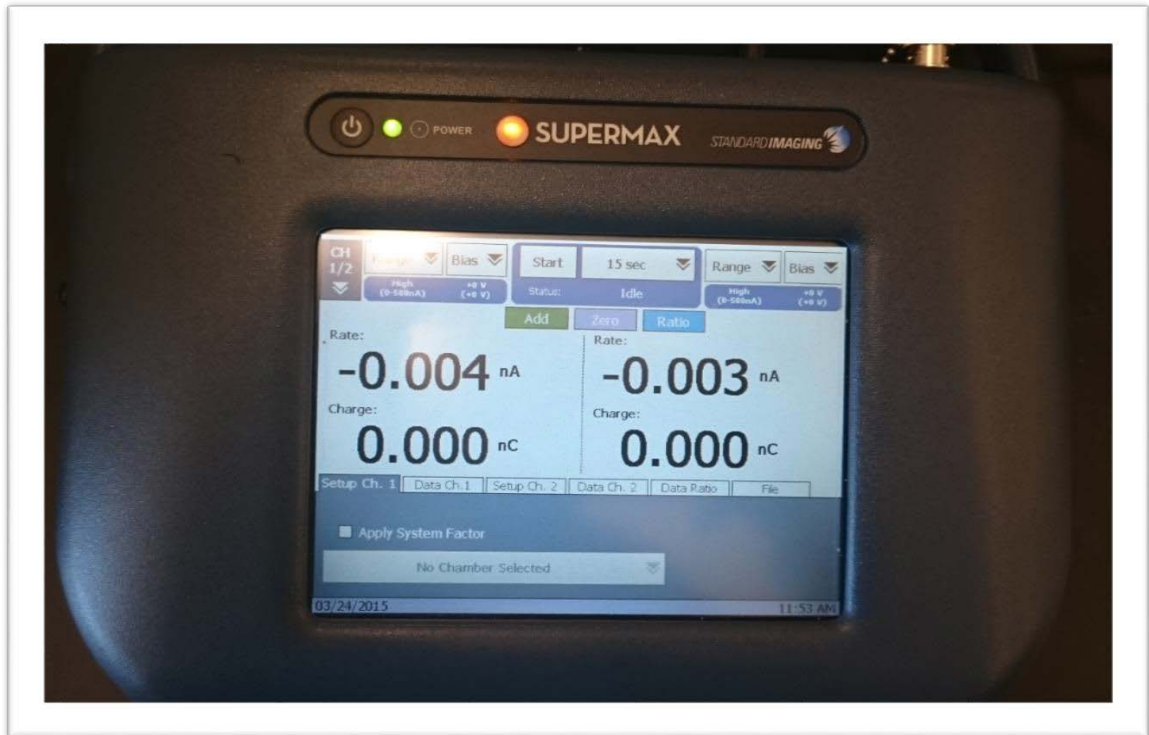


*Figure 4.21: The SuperMAX electrometer display*

The SuperMAX electrometer gives an output in the form of three different parameters including rate (current), charge and dose (air-kerma). To get the output in air-kerma, a system factor can be applied using the built-in detector library. SuperMAX has a built in wizard that allows the user to apply the system factor and store calibration data for a particular ionization chamber. The user can input parameters such as calibration date, calibration report number, beam quality and calibration coefficient for a given ionization chamber and the electrometer would automatically apply the conversion factors and give the corrected air-kerma value for a given ionization chamber. This feature of the SuperMAX is particularly useful since it can be used to store over 100 detectors and calibrations at a given time. In addition, SuperMAX also allows the user to save the data in an easy to read Excel format. Figure 4.22 shows the A-20 ionization chamber along with the calibration certificate for the chamber.



Figure 4.22: Exradin's A-20 ionization chamber along with its calibration certificate

## CHAPTER-5

### EXPERIMENTAL SETUP

#### 5.1 Design and construction of Low Energy Photon Irradiation Facility

The pre-existing experimental setup for this project is shown in Figure 5.1. The setup shows the Mini-X, X-123 spectrometer and the enclosure built to shield the X-Rays. Based on the results obtained from some preliminary experiments it was concluded that this experimental setup was not conducive for properly characterizing the X-Ray source. The reason being that the enclosure was too small to study the beam dimensions and also the setup was not conducive for performing the proposed biophysics experiments in future. This is because the enclosure was too small to fit any biological sample and also because the enclosure only allowed for one position to fit in the radiochromic films. It should be noted that the pre-existing setup is shown here because the results shown in Figure 6.1 were obtained using this setup.

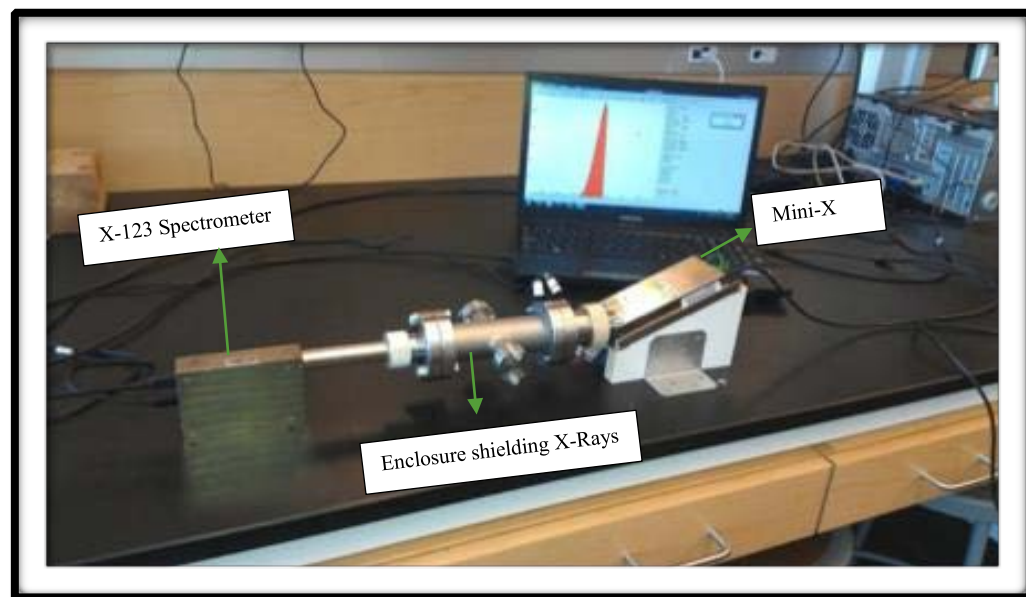


*Figure 5.1: Pre-existing experimental setup [16]*

Therefore, the pre-existing experimental setup was discarded and a new enclosure was constructed that would safely house all the detectors along with the X-Ray source. As per the regulatory requirement, it is required that the X-Ray source be secured firmly to the table, such that it cannot be removed from the lab. A dual-layered shielding was constructed with 1.4 cm thick primary aluminum shielding and a secondary 16-gauge stainless steel shielding. It was concluded that the aluminum shielding was not sufficient by itself since there was a significant amount of radiation leakage occurring at energies higher than 25 keV, especially when the current was increased beyond 50  $\mu\text{A}$ . This is due to the fact that the X-Ray mass attenuation coefficient for aluminum drops off from 3.094  $\text{cm}^2/\text{g}$  to 0.8778  $\text{cm}^2/\text{g}$  as energy is increased from 20 keV to 30 keV. In other words, the attenuation coefficient for aluminum decreases by a factor of 3.52 for the given energy increment. Therefore, the aluminum shielding was not enough by itself and hence, additional stainless steel shielding was required. A 16-gauge or 0.158 cm thick stainless steel shielding was constructed with the following dimensions:

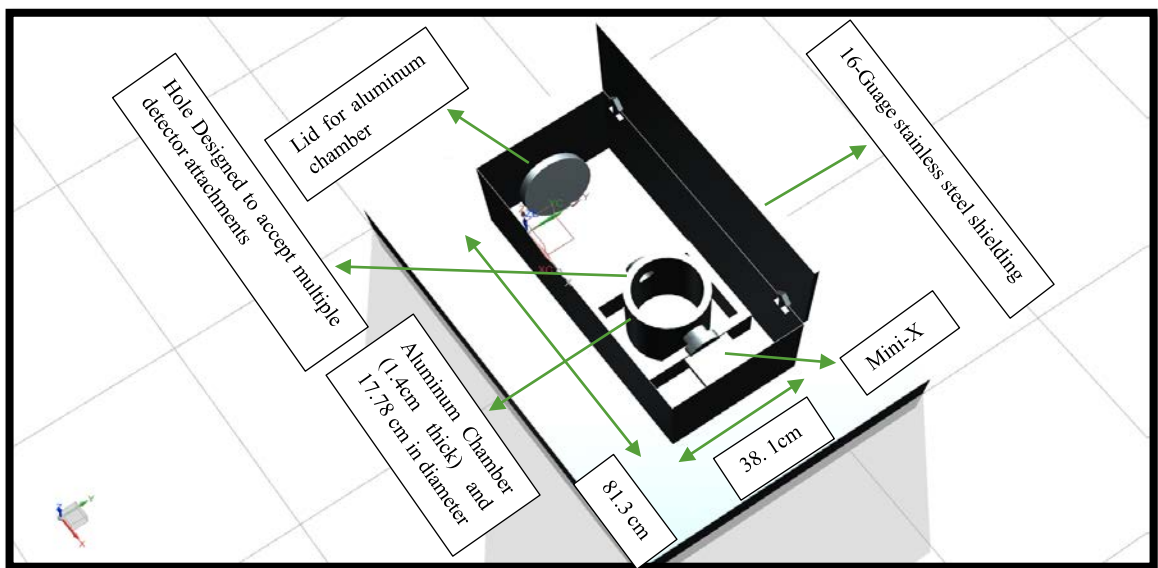


*Figure 5.2: Schematic of the experimental setup*

It was concluded that 16-gauge stainless steel shielding would cut the leakage from the primary aluminum shielding by a factor of 1000 for energies up to 30 keV. This attenuation was sufficient to bring the dose rate from leakage well within the regulatory requirements. The external stainless steel shielding was designed such that it sat on top of the primary aluminum shielding and like the aluminum shielding, the stainless steel shielding was also screwed securely to the table. To calculate the thickness of the shielding material, the mass attenuation coefficient formula was used as shown in equation 5.1:

$$I = I_o * e^{-\mu x} \quad [5.1]$$

Here,  $I$  represents the intensity of the radiation ‘exiting’ the material, while  $I_o$  represents the intensity of the radiation incident on the material and  $\mu$  represents the mass attenuation coefficient factor of a given material with thickness  $x$ . Figures 5.3 and 5.4, show two different viewpoints of the final experimental setup. In Figure 5.3, the external stainless steel shielding can be seen with the SuperMAX electrometer, Canon 8800F scanner along with the attached computer used to control the Mini-X and X-123 spectrometer.

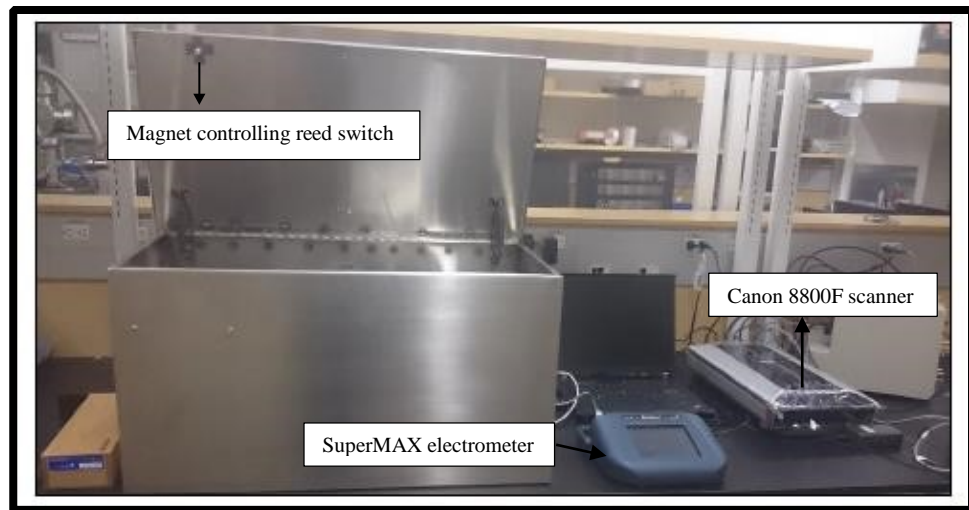


*Figure 5.3: Frontal view of the experimental setup showing the magnet controlling the reed switch, SuperMAX electrometer and Canon 8800F scanner*

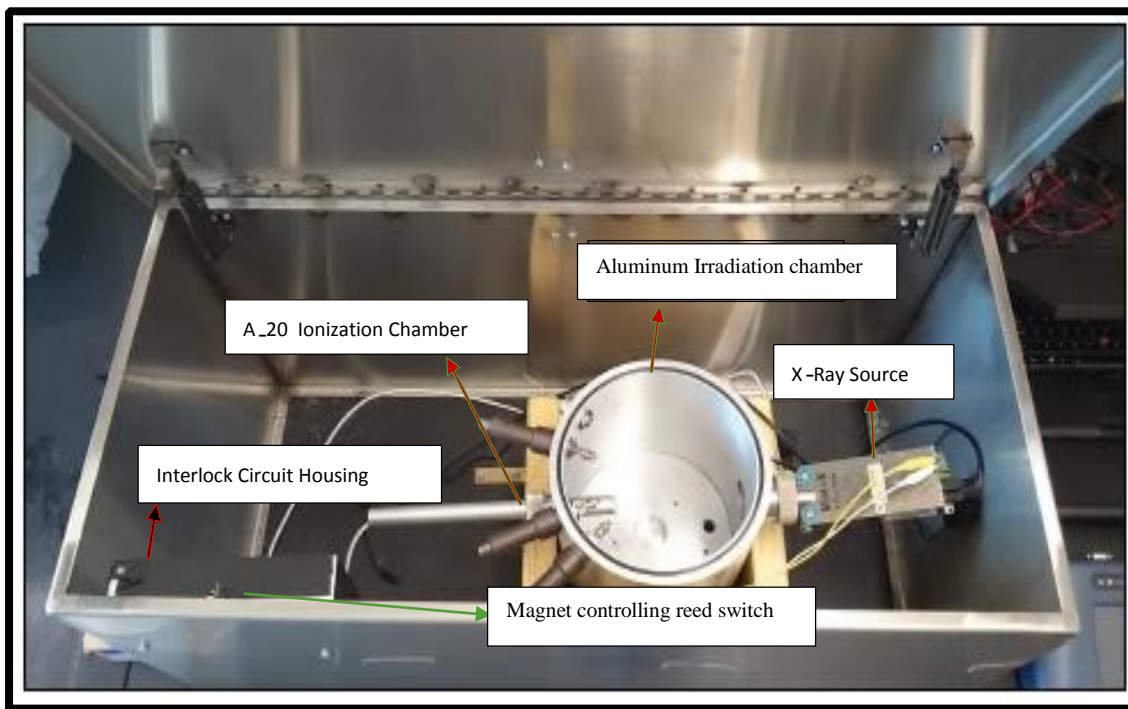


*Figure 5.4: Top view of the experimental setup*

As shown in Figure 5.4, the X-Ray source is housed within the aluminum chamber shielding that is secured firmly to the table with the help of a wooden base. The hole opposite to the X-Ray source is positioned so that it is in direct alignment with the X-Ray beam and can accept attachments including A-20 ionization chamber, X-123 spectrometer and a moveable rod mount for the radiochromic films. To use the ionization chamber a hollow piece of aluminum tube was used that would fit in the primary aluminum shielding. This hollow tube was used to house the ionization chamber such that its tip was precisely in the middle of the aluminum tube and in line with the X-Ray beam target. Similarly, a custom mount for radiochromic films was built using a plain sheet of metal. The top and bottom end of the sheet were bent to form a ‘pocket’ such that it would securely accept a piece of radiochromic film. The film mount was then attached to a 1/8 inch brass rod that allowed the user to freely move the radiochromic film back and forth and take

measurements at different distances from the X-Ray source. Figure 5.5 illustrates this concept further and shows how the moveable rod film mount was used.



*Figure 5.5: Experimental setup with the radiochromic film attachment*

The X-123 spectrometer attachment can be used using a similar setup where the ionization chamber is replaced by the spectrometer stem. As mentioned earlier, the interlock from the Mini-X was attached to an external circuit that was controlled via a magnetic reed switch. The specific type of reed switch used for this circuit was the OMRON's G4D-87P-BT2 magnetic reed switch. As the name implies, the reed switch consists of an open circuit that closes when two attached magnets are brought together. Figure 5.3 shows one of the two magnets attached to the secondary stainless steel shielding lid. These magnets come into contact once the lid is closed, completing the attached circuit. This design ensures that the X-Ray source would only run when the lid is closed thereby reducing the chances of accidental exposure to the user. Lastly, to add an additional layer

of safety, all the user controlled devices were placed to the opposite side of the X-Ray source such that the user was not in line with the X-Ray beam while operating the source. Figures 5.6 and 5.7 further show the schematic and actual design of the interlock circuit.

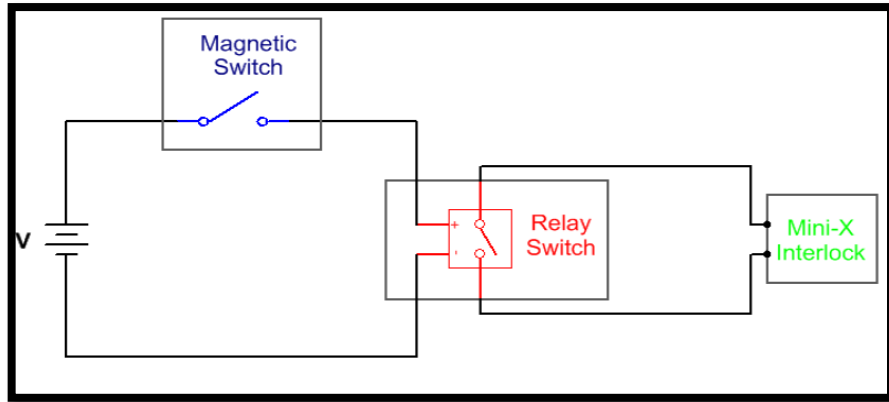


*Figure 5.6: Schematic of the Interlock circuit [8]*

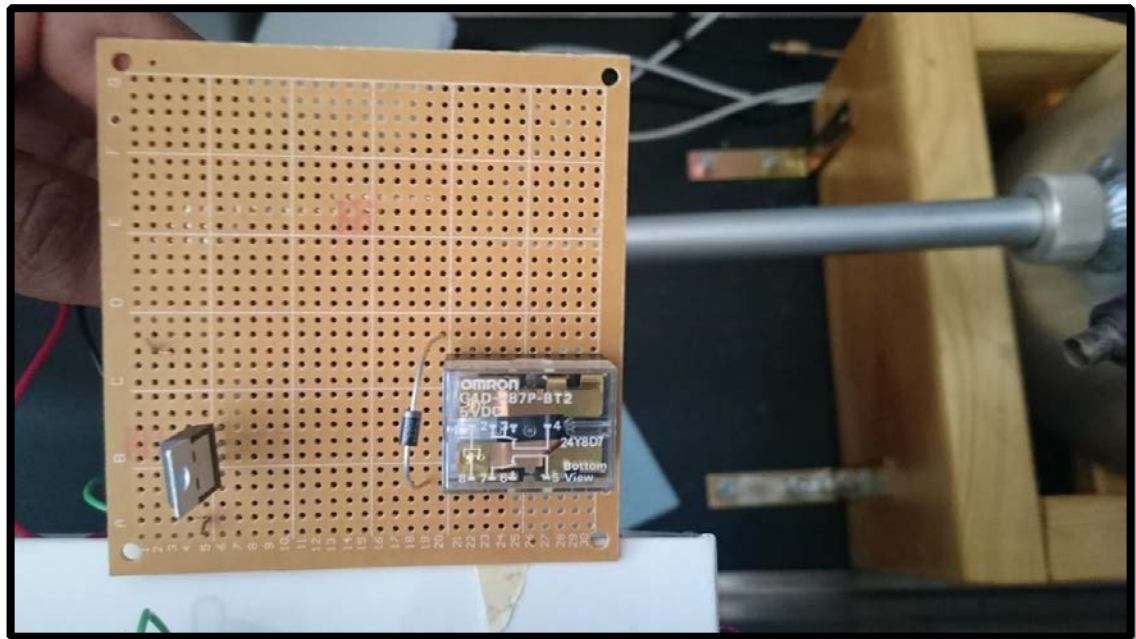


*Figure 5.7: Interlock circuit on the PCB board showing the reed switch, capacitor and a voltage regulator*

**CHAPTER-6**  
**RESULTS AND DISCUSSION**  
**Beam Characterization**

**6.1 Beam Dimensions**

The first part of the beam characterization process was to find the beam dimensions of the X-Ray source at varying energies and distances. This part of the experiment was done with the aid of radiochromic films and measurements were taken using different collimators at varying energies. The whole point of this part of the study was to find the change in size and uniformity of the beam as a function of distance from the source. Ideally from a biophysics point of view, one would require a uniform beam that is big enough to cover the proposed target volume. By doing so, the user can keep track of the exact amount of dose being delivered to the target volume at a given time and as stated earlier, radiochromic film is an excellent tool to accomplish this.

The first part of the experiment was to find the response of the film as a function of time (or the dose delivered). To accomplish this, the radiochromic film was exposed to radiation for different periods of time and the resultant optical density was analyzed as a function of time. It should be noted that in this case the increase in time refers to the increase in total dose delivered to the film. As expected, the optical density of the films increased as a function of time, indicating the optical density is directly proportional to the dose absorbed by the film. As shown in Figure 6.1, there is a direct linear relationship between the optical density of the film and the exposure time. The coefficient of determination, or the  $R^2$  value, for this relationship was 0.9997 thereby, indicating a strong linear relationship between optical density value and its corresponding exposure time. The coefficient of determination simply defines how well the data fits a given statistical model and the value

for this parameter can range anywhere between 0 and 1, where a value closer to 1 indicates a strong correlation between data and the statistical model. Hence it can be concluded that there is a strong linear relationship between the optical density of the film and dose absorbed. It should be noted that the measurements for Figure 6.1 were taken at 20 keV and 5  $\mu$ A and the linearity has been found to be independent of the energy or current of the incident X-Rays.

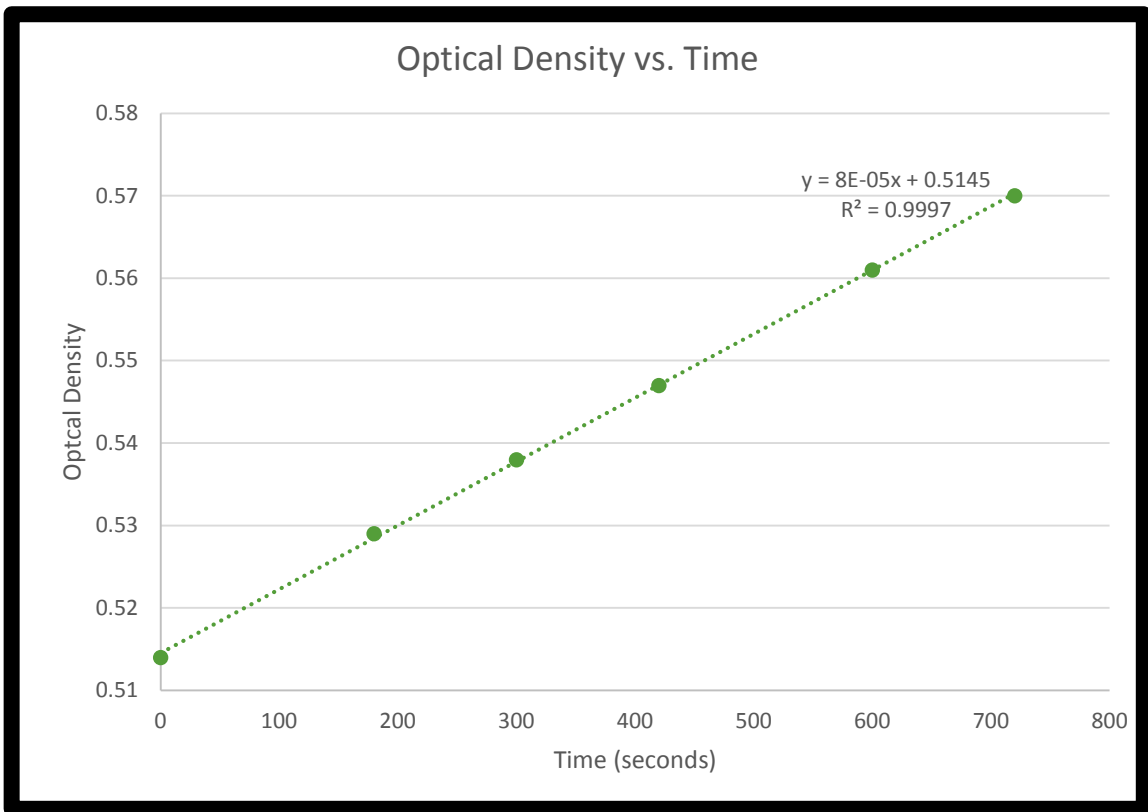


*Figure 6.1: Optical Density vs. Time for the Mini-X source*

The only thing that changes as a function of energy and current is the optical density. That is, the optical density increases as a function of the energy and flux. Also for a given energy, if the current is increased, the optical density also increases because flux increases as a function of the current. The linear relationship has been found to stay true

for all the energies investigated. Another example of the film's linear response can be seen in Figure 6.2, where the measurements were taken using Thermo Fisher's P-385 Neutron Generator. This accelerating tube has been demonstrated to emit X-Rays with average photon energies of approximately 70 keV.

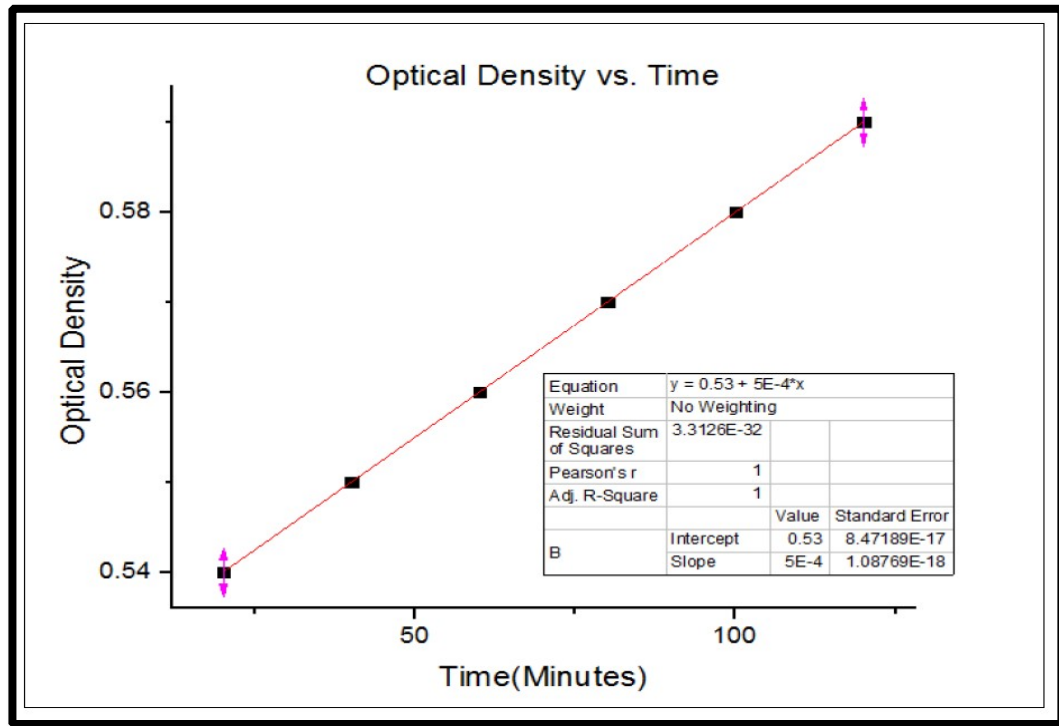


*Figure 6.2: Film Response for P-385 Thermo Fisher Neutron Generator*

The next parameter that was investigated was the dimensions of the beam as a function of distance from the source. For this part of the experiment two different set-ups were used including a 3 mm collimator and a screw-on brass cover respectively. Figure 6.3 shows, different accessories that come standard with the Mini-X, which includes a brass safety plug, screw on brass cover and a 2 mm brass collimator with an aluminum insert. It should be noted that the collimators and the brass safety plug sit inside the brass cover. An additional 3 mm brass collimator, without the aluminum insert was fabricated since the 2 mm collimator was too small for the beam characterization purposes. While on the other

hand the beam cone of  $120^\circ$  (without the brass cover) was too big for the existing setup. In other words, the beam became too large for the radiochromic film to measure without the screw-on brass cover. Therefore, all the measurements were taken either with just the brass cover or 3 mm collimator.



*Figure 6.3: Mini-X Accessories [8]*

For this part of the experiment, the radiochromic films were exposed to beams of 10 keV, 15 keV, 20 keV, and 25 keV at a current of  $50 \mu\text{A}$ . The film was exposed to radiation at various distances from the source and the resulting dimensions of the beam were then measured. Figure 6.4 shows how the beam height and beam width were defined. The beam height in Figure 6.4 defines the major axis of the ellipse while the beam width defines the minor axis of the ellipse.

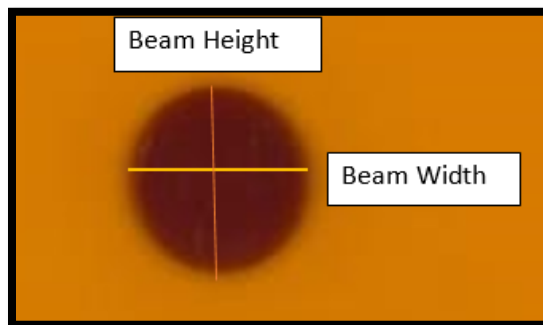


*Figure 6.4: Lines showing how the beam height and beam width are defined on the film*

Based on the measurements taken it was concluded that the beam was elliptical in shape and increased in size as a function of distance from the source. Figures 6.5 to 6.12 show the results obtained from this part of the experiment. As seen in Figure 6.5, when the setup involving the 3 mm collimator was used at 10 keV, the beam had dimensions of 2.9 cm in width and 4 cm in height at the distance of 10.16 cm (4 inches) from the source. Whereas, the setup involving just the brass cover at 10 keV gave a beam with width of 4.7 cm and height of 5.1 cm at 10.16 cm from the source.

It should be noted that Figures 6.5 to 6.12 are required here even though its results are reproduced in Figures 6.13 and 6.14 because the latter does not provide a clear picture about the beam dimensions due to the strongly overlapping points. Therefore, Figures 6.5 to 6.12 are included to give a direct measure of the beam size as a function of distance for different energies.

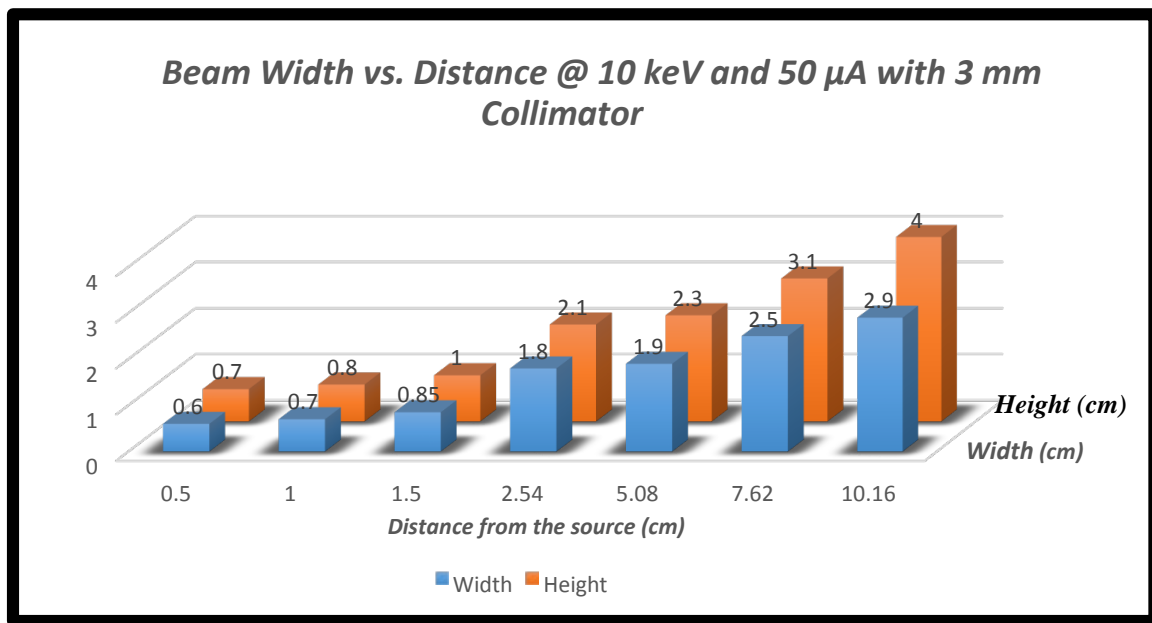


*Figure 6.5: Beam size at 10 keV and 50  $\mu$ A with 3 mm collimator*

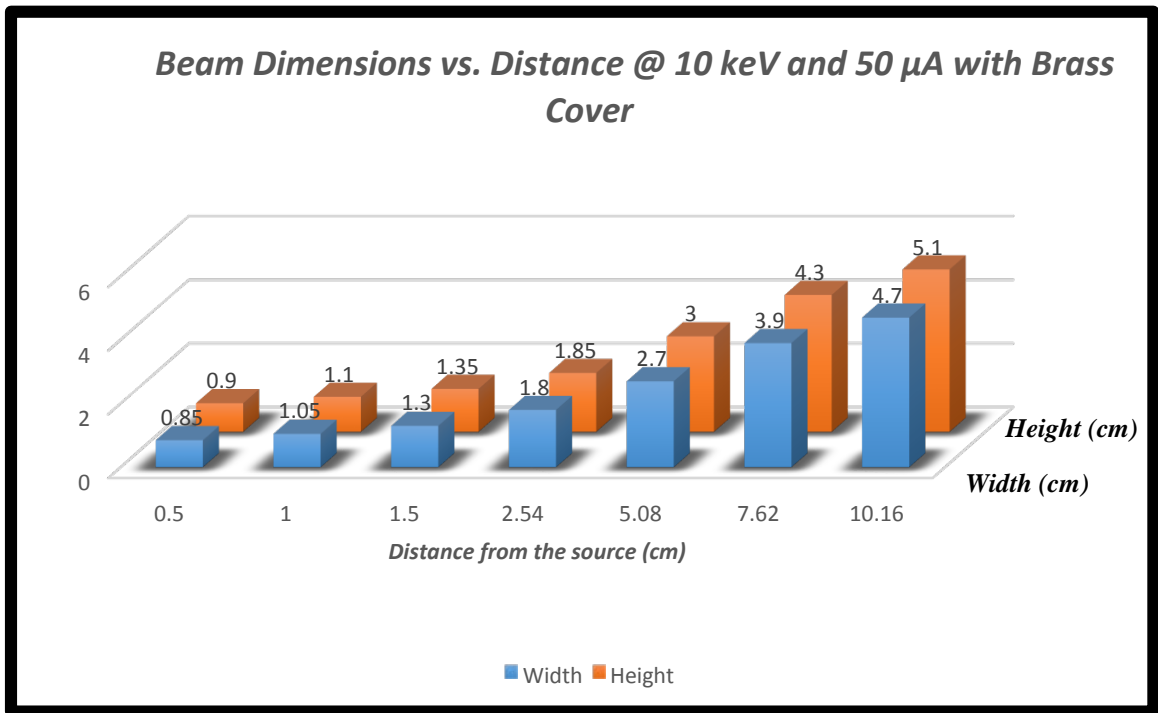


Figure 6.6: Beam size at 10 keV and 50  $\mu$ A with the brass cover

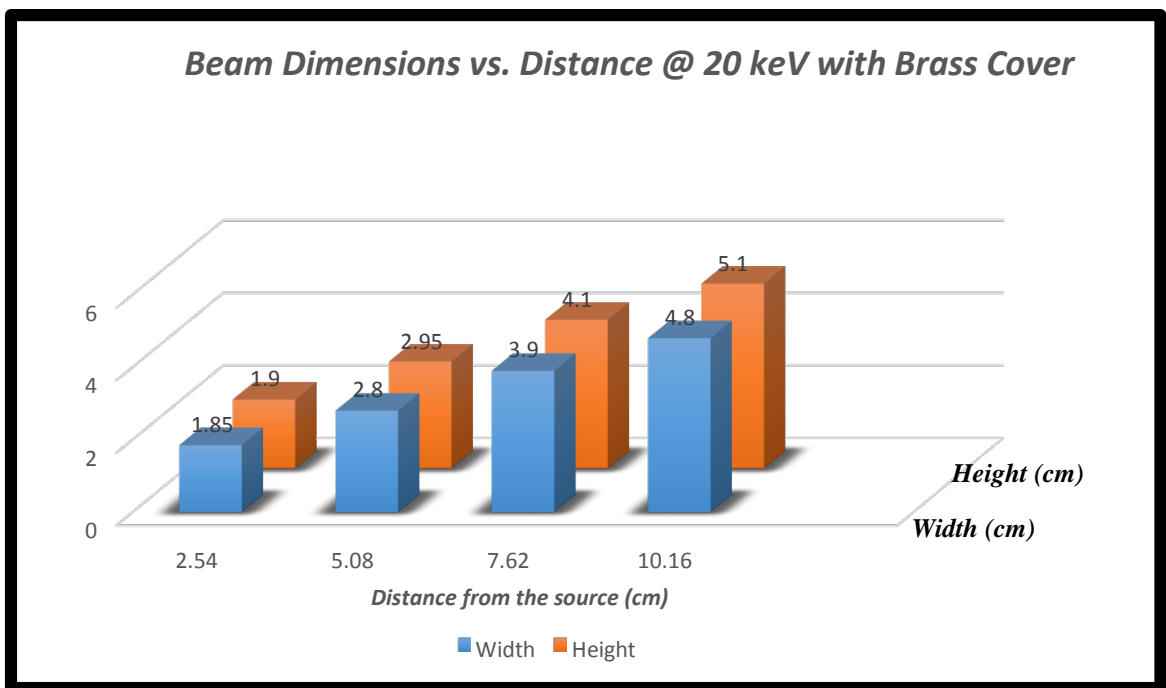
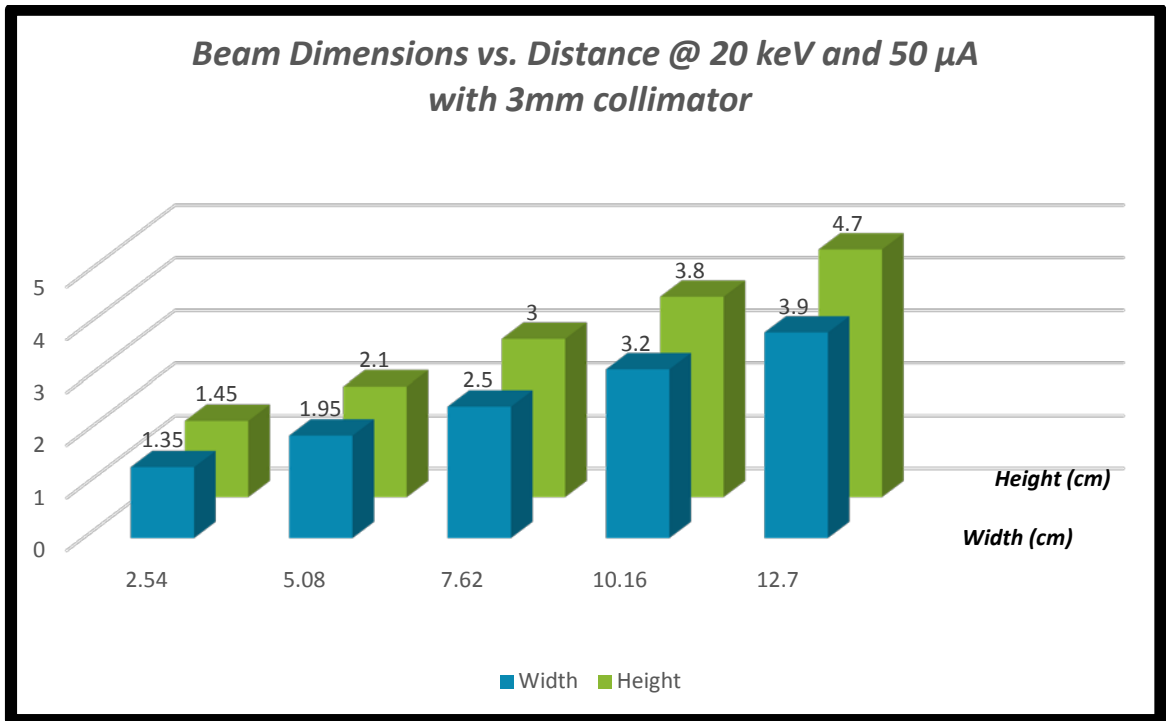
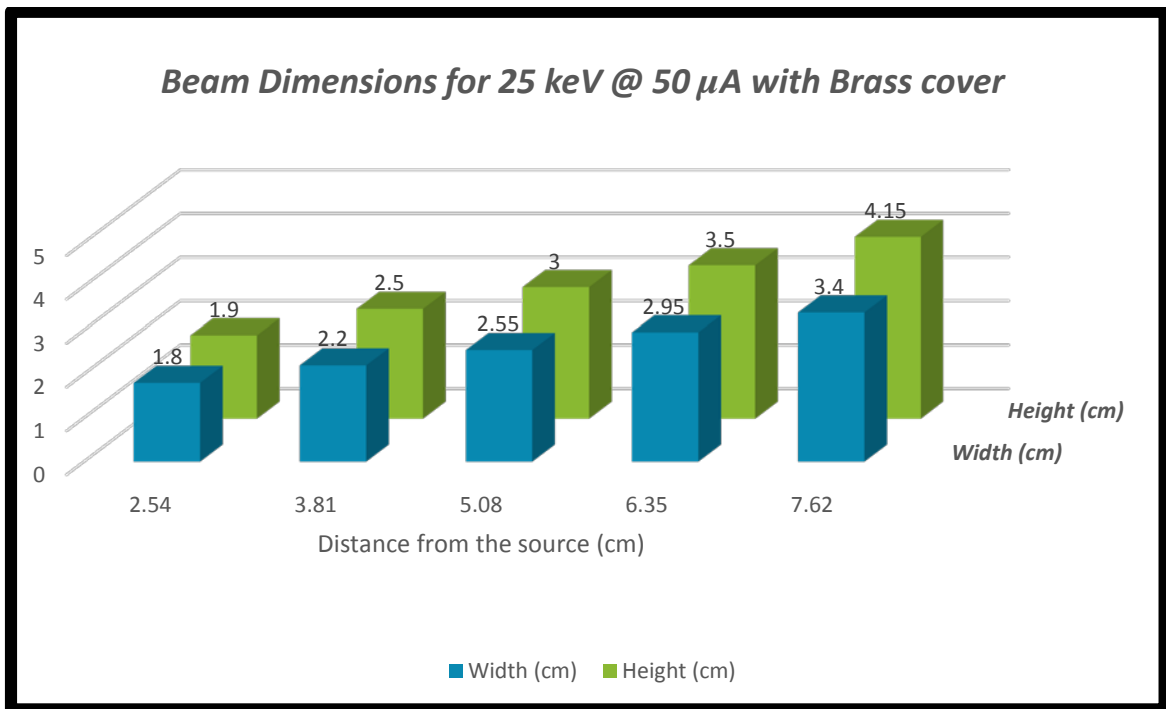


Figure 6.7: Beam size at 20 keV and 50  $\mu$ A using the brass cover



*Figure 6.8: Beam size at 20 keV and 50  $\mu$ A using the 3 mm collimator*



*Figure 6.9: Beam size at 25 keV and 50  $\mu$ A using the brass cover*

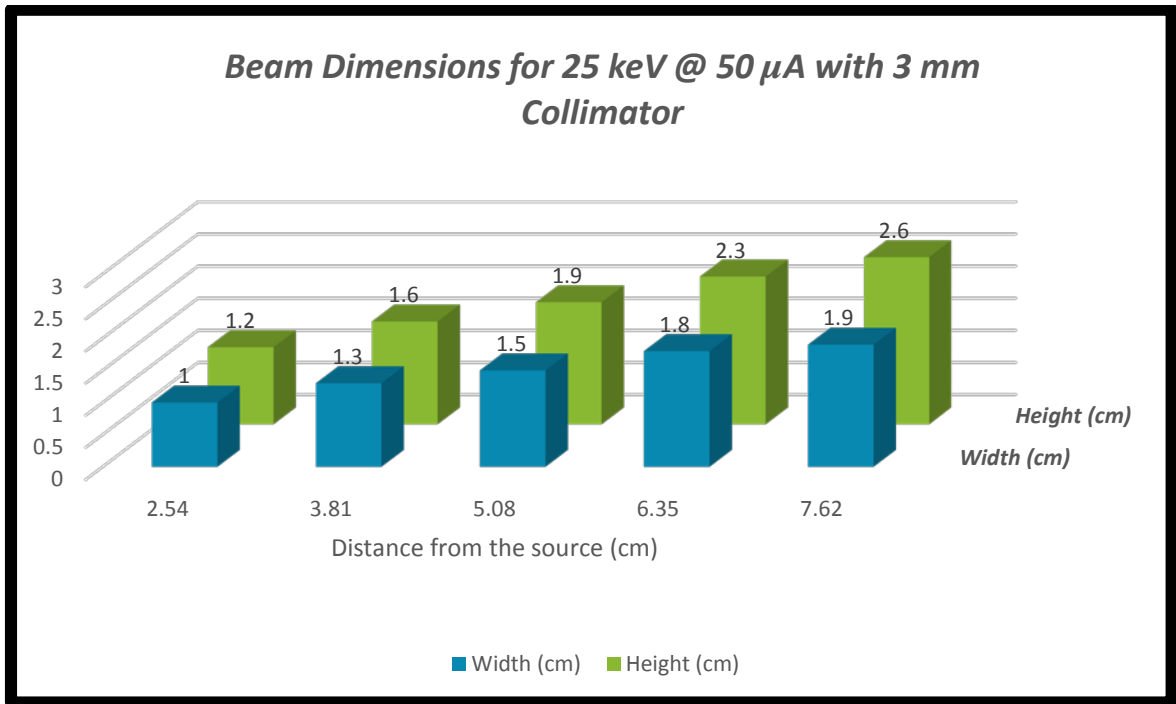


*Figure 6.10: Beam size at 25 keV and 50  $\mu$ A with the 3 mm collimator*

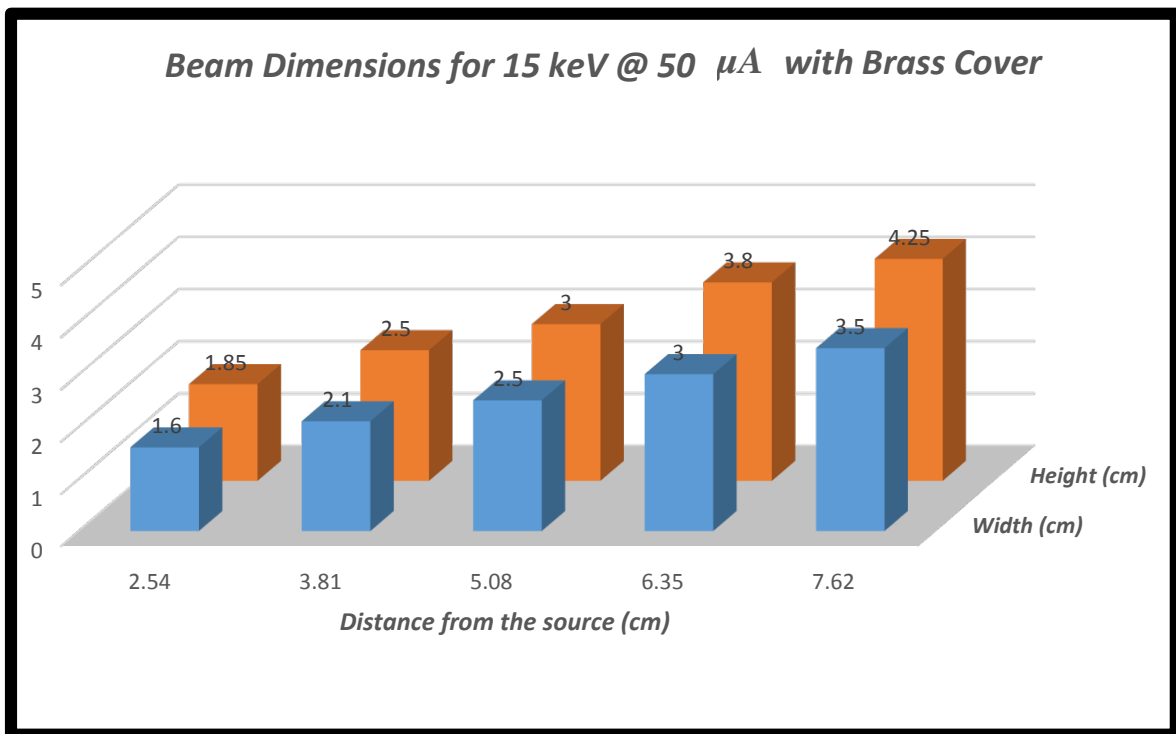


*Figure 6.11: Beam size at 15 keV and 50  $\mu$ A using the brass cover*

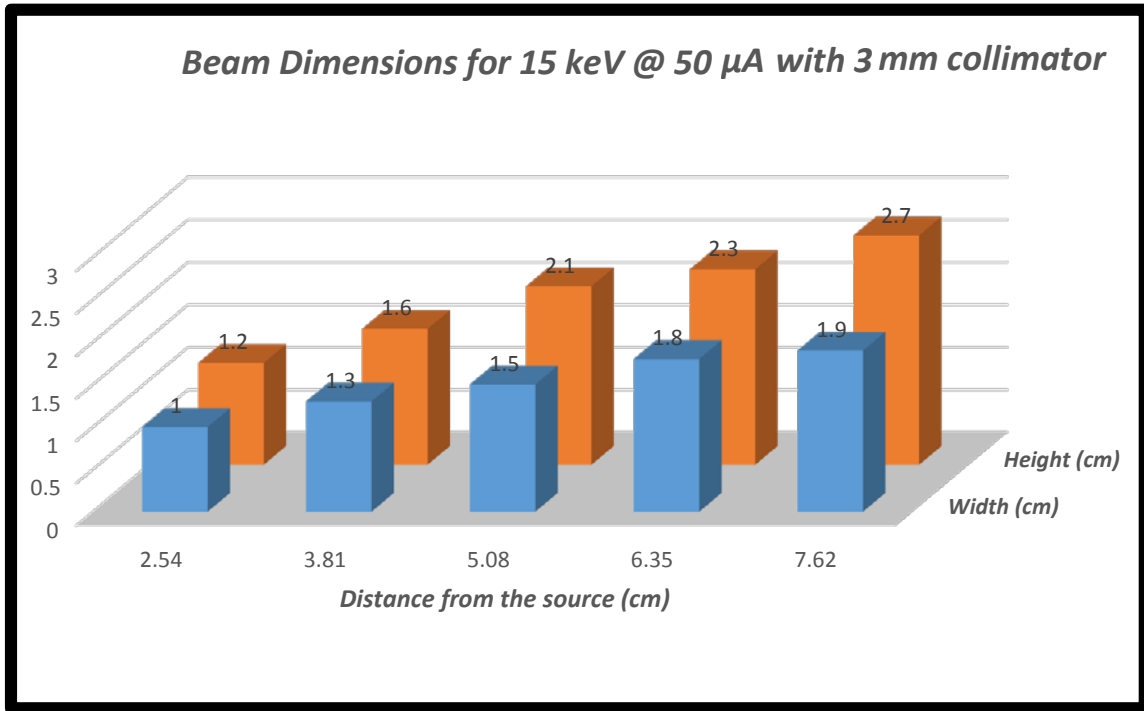


*Figure 6.12: Beam size at 15 keV and 50  $\mu$ A using the 3 mm collimator*

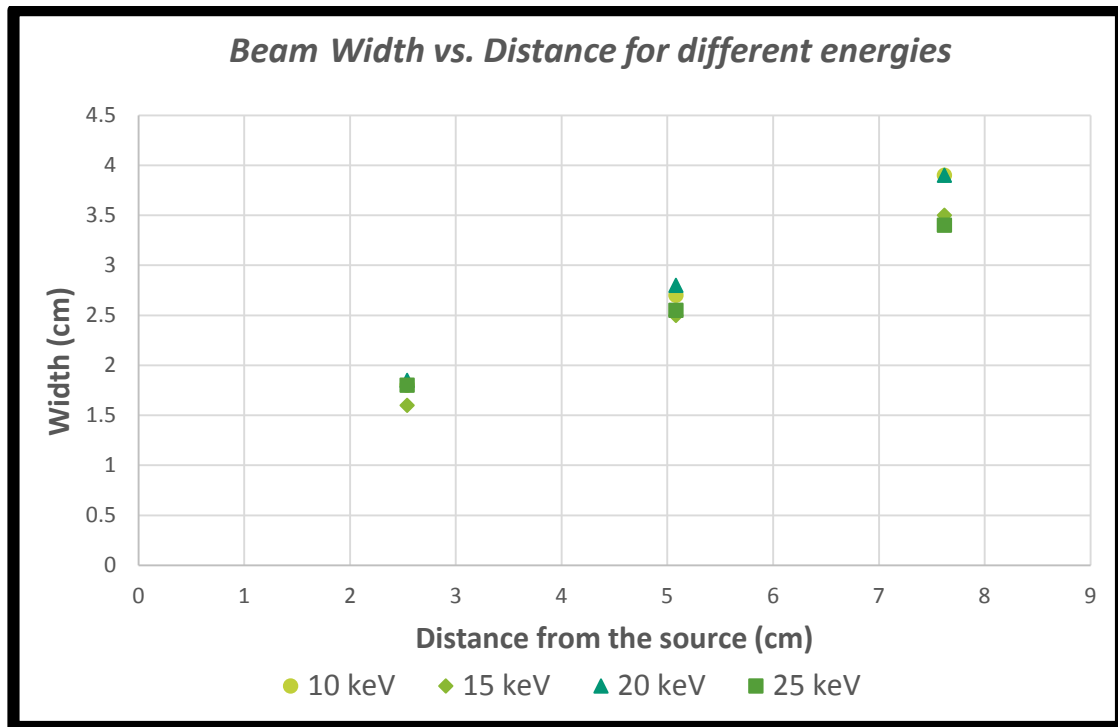


*Figure 6.13: Beam width as a function of distance for different energies*

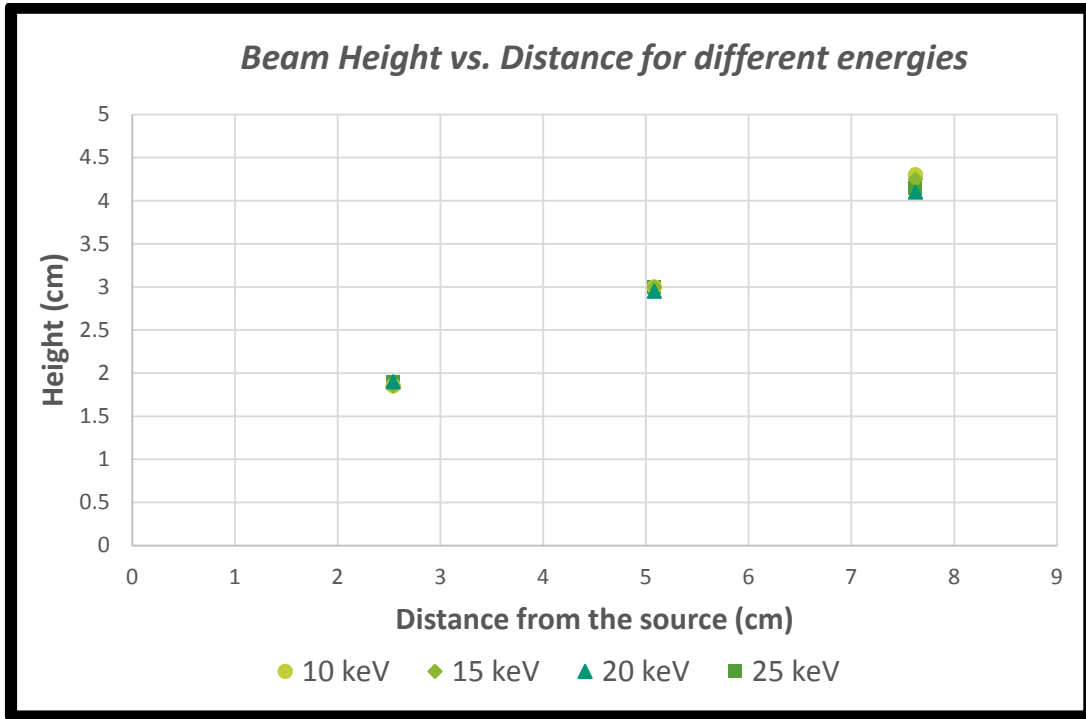


*Figure 6.14: Beam height as a function of distance for different energies*

The key observation here was that for a given setup the beam size does not change appreciably as the energy was increased from 10 keV to 25 keV. This is explained in more detail in figures 6.13 and 6.14. These graphs show how the height and width of the beam is changing as a function of distance, for different energies. As evident from the two graphs there is not a significant difference in the size of the beam for either of the four energies. This trend also holds true for the setup involving the use of 3 mm collimator. Hence, it can be concluded that beam size is independent of the energy for a given setup and would yield a similar sized beam at a given distance. Please note that Figures 6.5 to 6.12 show how the height and width of the beam changes a function of distance. To give an example, in Figure 6.5 the blue bar represents the beam width at a given distance while the orange bar represents the beam height at the same given distance.

## 6.2 Beam Uniformity

The next step in the beam characterization study was to test the uniformity or the spatial distribution of photon flux in the beam. To test the uniformity of the beam, similar approach was used as per the previous experiment and the resultant uniformity of the beam was explored as a function of distance.

To find the spatial distribution of the beam, ImageJ was used to analyse the films. As stated previously, ImageJ allows the user to use a commercial flatbed scanner as a densitometer. Using calibrated optical density values one can use ImageJ to obtain a plot profile in terms of optical density vs. distance. Furthermore, to get the spatial distribution of an image one can use the known distance of the image to calibrate pixels for distance.

Using the built in 'line' command in ImageJ, the user can define the starting and the end points for the region of interest, and by selecting the 'set scale' option under the 'analyze' drop down menu, the user can then enter the known distance of the region of interest and thereby, convert the number of pixels into distance. For example, in Figure 6.15, there are 600 pixels between the starting and the end point of the region of interest and the actual width of the beam spot is 2.7 cm. Therefore, using simple math ImageJ generates a conversion factor that sets the scale in terms of cm hence, providing more useful information. Upon setting the scale, the region of interest (ROI) can then be selected for which ImageJ plots the spatial distribution in terms of optical density vs. distance (as shown in Figures 6.17 and 6.18). The ROI can be changed accordingly and the spatial distribution of the film can be measured at different locations to decipher how the absorbed dose is changing over the selected regions of radiochromic film.

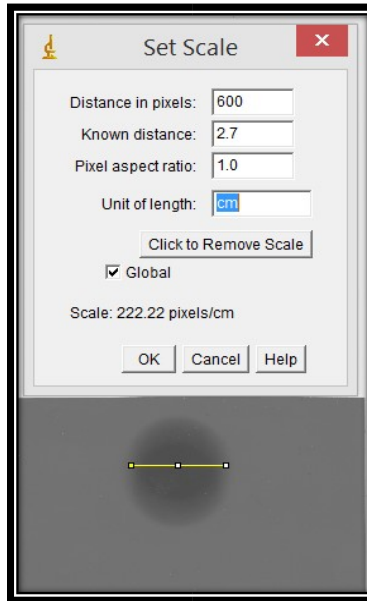


*Figure 6.15: Scale calibration in ImageJ*

ImageJ allows the user to obtain a plot profile using two different selection methods. The first method is the ‘line method’ and the second is the ‘rectangular method’. Figure 6.15, shows an example of the line method. In this specific method, the resultant plot profile obtained shows how the optical density of the film is changing as you move across the selected line. This selection method is particularly useful in measuring the change in optical density of a specific spot. In contrast, the rectangular method takes the average optical density for a given column of pixels and shows a plot profile with optical density averaged over a given column of pixels. For this work, the line method was used to find the spatial distribution since it provides a more accurate measure of the change in optical density along a specific ROI.

To elaborate further, Figure 6.16 shows how the line method can be used to find the optical density distribution at different points over the beam image. By dividing the beam into different slices the user can obtain a better idea of how the optical density is

changing over the whole beam. Similarly, the end points of the line or ROI can be defined from top to bottom and user can measure how the absorbed dose is changing along the major axis of the beam.

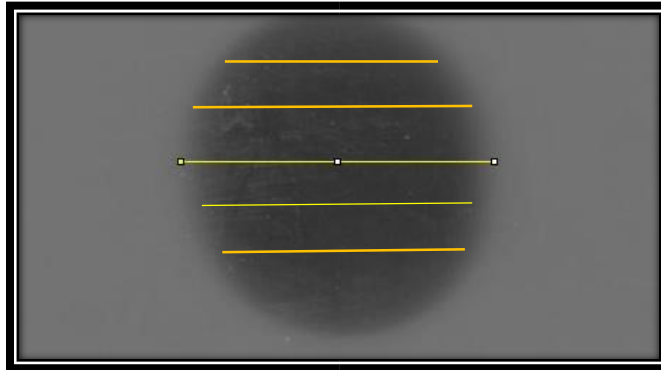


*Figure 6.16 Example of how line method can be used to obtain the spatial distribution at varying positions along the image*

Figure 6.17, gives an example of a radiochromic film exposed to 20 keV beam at 2.54 cm from the source. As evident from the optical density distribution of the film, the dose delivered is fairly uniform since the net optical density difference between the crest and trough of the plateau is 0.03 (the crest of the plateau is at 1.20 and the trough is at 1.17). It should be kept in mind that the optical density distribution in Figure 6.17 is that of the beam spot and spans the distance marked by the yellow line in Figure 6.18. This trend continued for all the other trials and the beam profile stayed fairly flat at distances up to 12.7 cm from the source. Figure 6.19, gives an example of the spatial distribution of a beam at 7.62 cm (Figure 6.20) from the source using the same current and high voltage. Again, as evident from the graph, the optical density of the film stays fairly uniform and there is very little difference between the crest and trough of the plateau, just like the beam at 2.54 cm from the source. This trend of beam uniformity holds true for all the other energies.

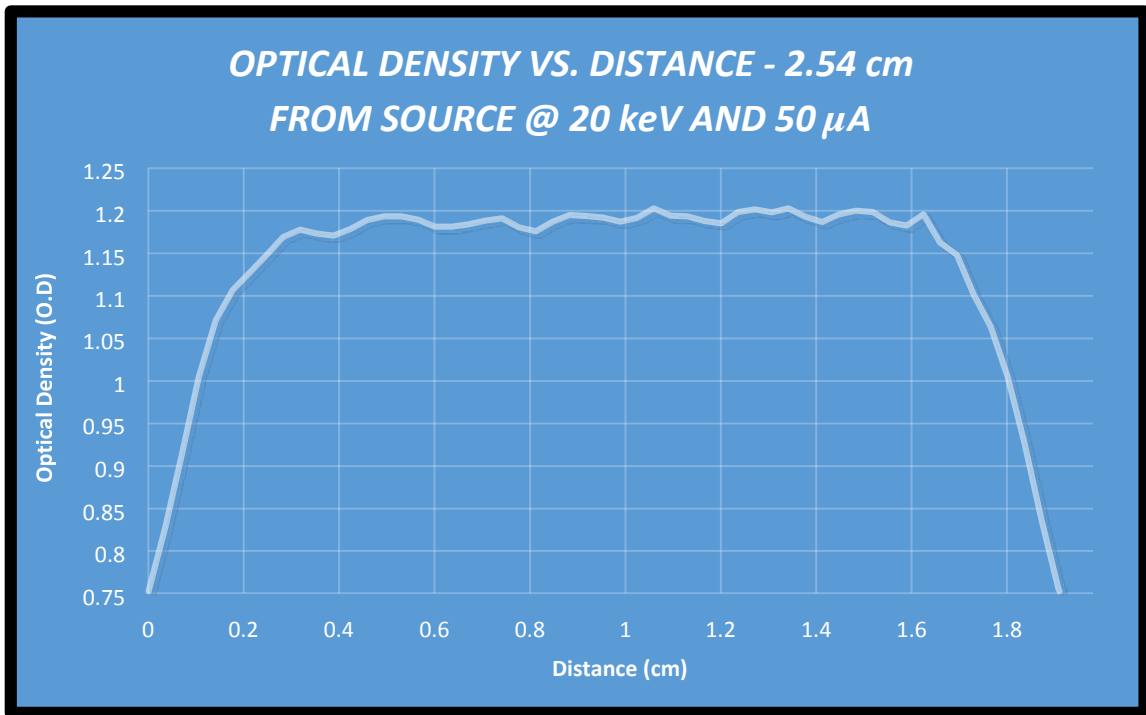


Figure 6.17: Spatial distribution of the 20 keV beam at 2.54 cm from the source

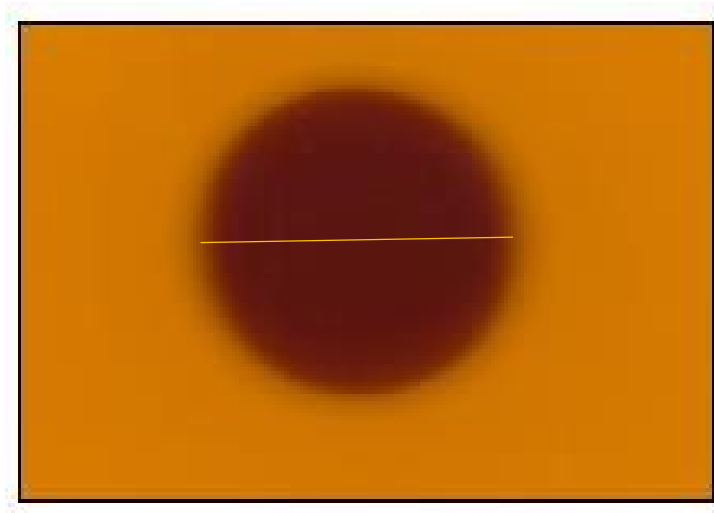
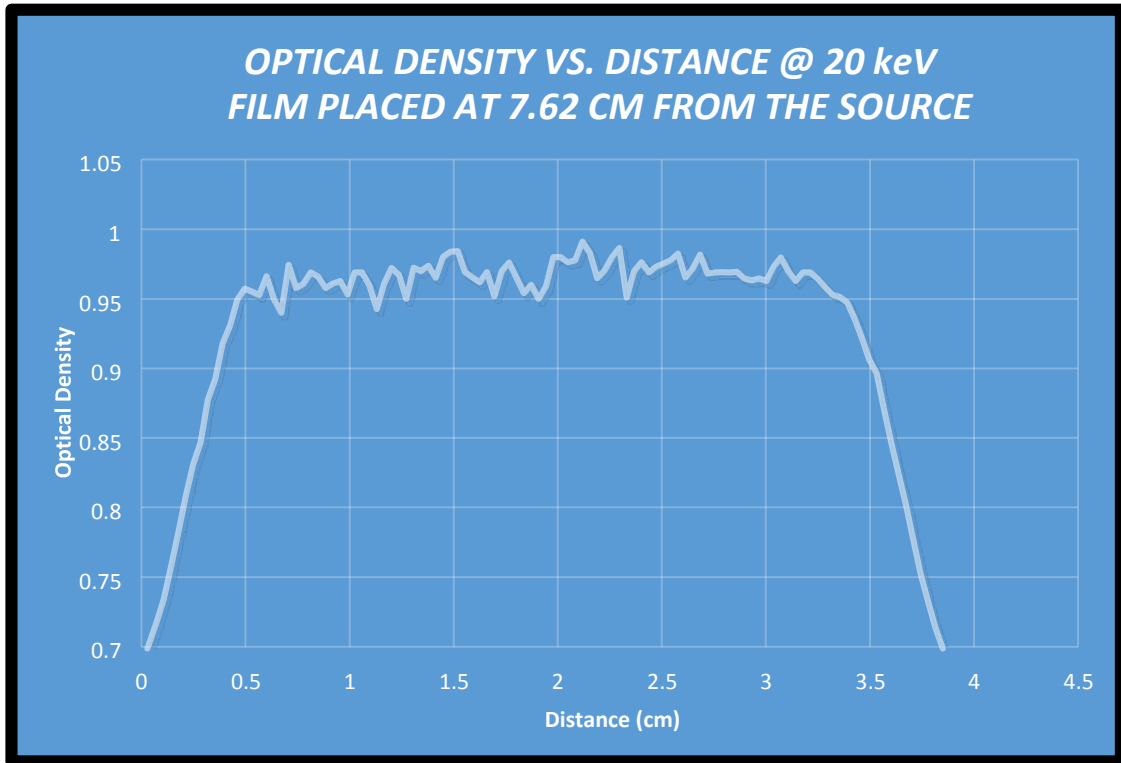
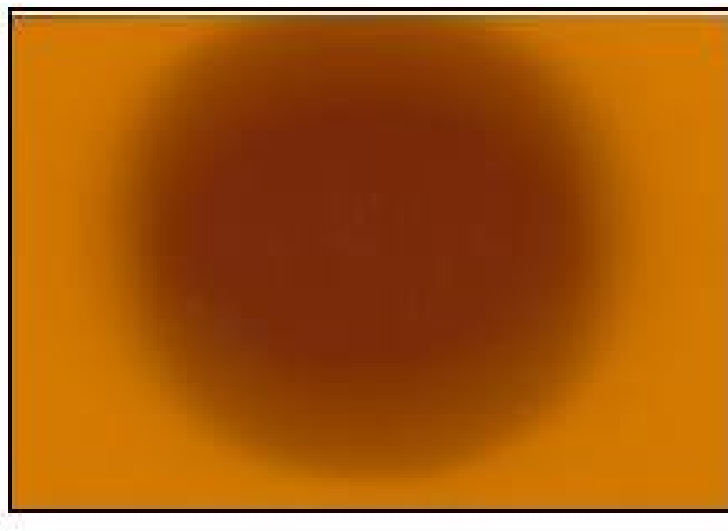


Figure 6.18: Film exposed to 20 keV beam at 2.54 cm from the source



*Figure 6.19: Spatial distribution of the beam at 7.62 cm from the source*



*Figure 6.20: Radiochromic film exposed to 20 keV at 7.62 cm from the source.*

## 6.3 Dosimetry

### 6.3.1 Air Kerma vs. Distance

Once, beam dimensions and beam uniformity of the X-Ray source had been established, the next part of the project was to find the actual dose delivered by the X-Ray source. This part of the study was carried out using the A-20 ionization chamber and SuperMAX electrometer. The first objective of the dosimetry experiment was to determine the air-kerma rate values as a function of distance. The word kerma is an acronym that stands for ‘kinetic energy released per unit mass’ and air-kerma simply stands for the kinetic energy released per unit mass of air [23]. The term absorbed dose itself is defined as the energy absorbed per unit mass and the term dose rate is defined as dose delivered per unit time. Mathematically dose and dose rate can be defined as per the following two equations.

$$Dose (Grays) = \frac{Energy}{Mass} \quad [6.1]$$

$$Dose Rate \left( \frac{Grays}{Second} \right) = \frac{Dose}{Time} \quad [6.2]$$

It should be noted that dose is a parameter that is dependent on the absorbing medium and different absorbing media would yield different absorbed dose values for same photon fluence. For example, same beam would yield different dose rate values in tissue as compared to air. For this part of the investigation, the ionization chamber was exposed to X-Rays of different energies at different distances from the source and the resultant air-kerma rate values were noted. Figure 6.21 plots the Air Kerma profiles for 10 keV, 15 keV, 18.5 keV, 20 keV, 25 keV, and 30 keV energies at 5  $\mu$ A. It should be noted that all the air-

kerma rate values are defined in units of centigrays/second (cGy/s) and the dose rate standard deviation from three trials was below  $\pm 0.001$  cGy/s.

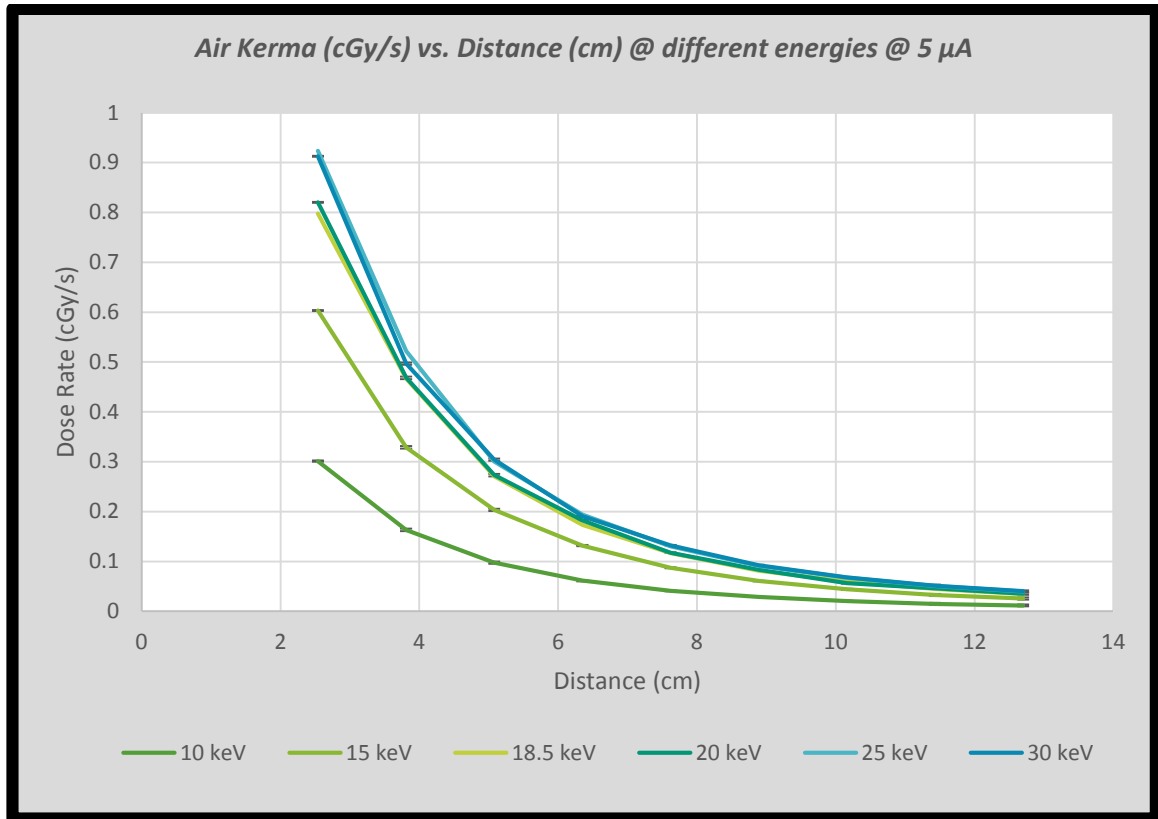


*Figure 6.21: Air Kerma rate vs. Distance for the Mini-X at varying energies*

The key observation from this set of data is that the dose rate drops by roughly half as you move from 2.54 cm to 3.81 cm. For example, the 10 keV beam gives a dose rate of 0.3 cGy/s at 2.54 cm and 0.16 cGy/s at 3.81 cm. Furthermore, the dose rate decreases roughly by a third as you move from 2.54 cm to 5.08 cm and as evident from the graph this trend stays true for all the energies. Another interesting observation made from Figure 6.21 is that the dose rate saturates at 25 keV and is approximately same as that at 30 keV.

The experimental air-kerma values obtained from the experiment were also compared with an inverse square fit. According to the inverse square law, the intensity of a point source of radiation becomes weaker as it spreads over larger distances and mathematically can be written as:

$$(I_1)/(I_2)=(D_2^2)/(D_1^2) \quad [6.3]$$

Here  $I_1$  and  $I_2$  represents the intensity of the radiation at distances  $D_1$  and  $D_2$  respectively. Therefore, if the intensity of the radiation is known at a specific distance, using equation 6.3 the intensity at any given distance may be found. In other words, the intensity of the radiation is inversely proportional to the square of the distance from the source. Since the intensity of the radiation gives a direct measure of the dose rate, this formula can be used to calculate the expected air-kerma values at different distances. The intensity can be replaced by the dose rate and using the same formula one can find the expected dose rate at a given distance from the source. Figure 6.22, shows an example of the comparison between the inverse square fit and the experimental dose rates obtained at the energies of 10 keV and 30 keV respectively (at 5  $\mu$ A). As evident from Figure 6.22, the experimental values for both 10 keV and 30 keV matches the inverse square fit well and the maximum percent difference between the two fits is below 3 %. Hence, it can be concluded that dose rate distribution from the Mini-X closely follow the inverse square law and for a given energy, the inverse square law can be used to approximate the dose rate at a specified distance. This trend was observed for all the energies and the measured experimental dose rates were slightly higher than that of the theoretical dose rates and this difference might be caused by the scattering back into the beam of the X-Rays occurring inside the irradiation chamber hence causing comparatively higher measured dose rates. It

should be noted that the Mini-X beam is only an approximation of a ‘point source’ required by the strict derivation of the inverse-square law.

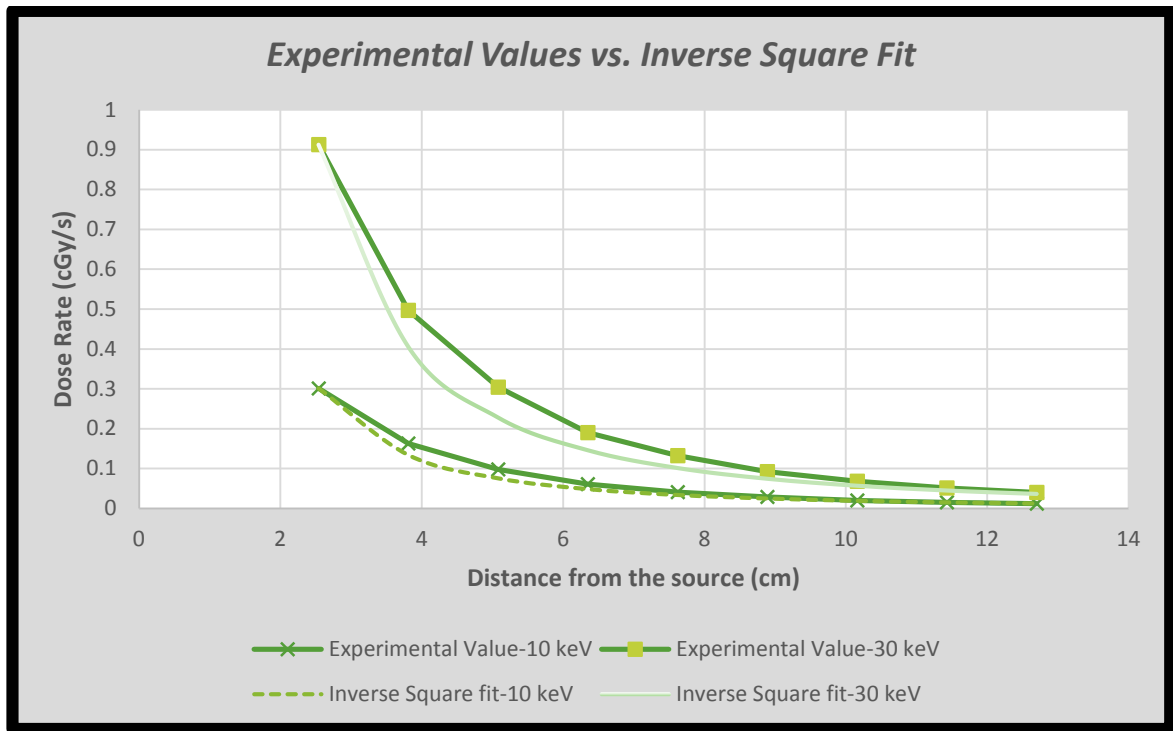
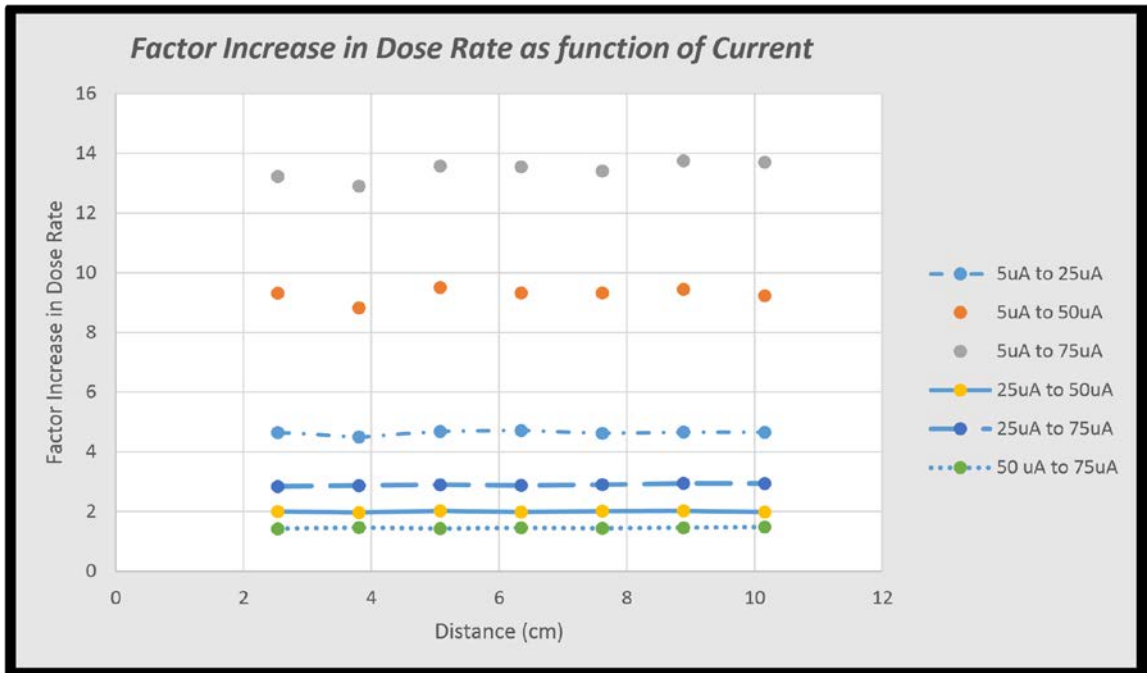


Figure 6.22: Experimental values vs. Inverse square fit

In addition, it was also explored how the dose rate changed as a function of current. As expected the dose rate for a given energy increased quite significantly as the current was increased beyond 5  $\mu\text{A}$ . The effects of current on the increase in dose rate are summarized in Figure 6.23, which shows the factors by which the dose rate changes as you increase or decrease the tube current. Figure 6.23 shows that for a given energy if the current increases from 5  $\mu\text{A}$  to 25  $\mu\text{A}$ , the dose rate increases by a factor of 4.6. This factor becomes more substantial as the current is further increased beyond 25  $\mu\text{A}$ . For example, the dose rate increases by a factor of 13.6 as one goes from 5  $\mu\text{A}$  to 75  $\mu\text{A}$ . In other words for a given distance, if 1 cGy/s is obtained at 10 keV and 5  $\mu\text{A}$ , roughly 13.6 cGy/s would be obtained at the same distance for same energy at 75  $\mu\text{A}$ . Thus, it can be deduced that

the dose rate for a given energy can be increased substantially by increasing the current and this can be a very useful attribute for biophysics experiments requiring high doses. Again, it should be noted that the current for Mini-X can be increased to the maximum of 200  $\mu\text{A}$  and significantly higher dose rates are possible



*Figure 6.23: Effect of current on the dose rate*

Furthermore, Figure 6.24 shows how the dose rate compares with current for different energies at a given distance and shows the resultant mathematical relationship between the dose rate and the current. There is a strong linear relationship between the dose rate and the current, as evident from the high  $R^2$  values. To give perspective, at 10 keV an  $R^2$  value of 1 was obtained, indicating a perfectly linear relationship between the dose rate and current. Hence, it can be concluded that dose rate increases linearly as a function of current and the equations given in Figure 6.24 can be used to estimate the increase in the dose rate if the current is increased beyond 75  $\mu\text{A}$ .

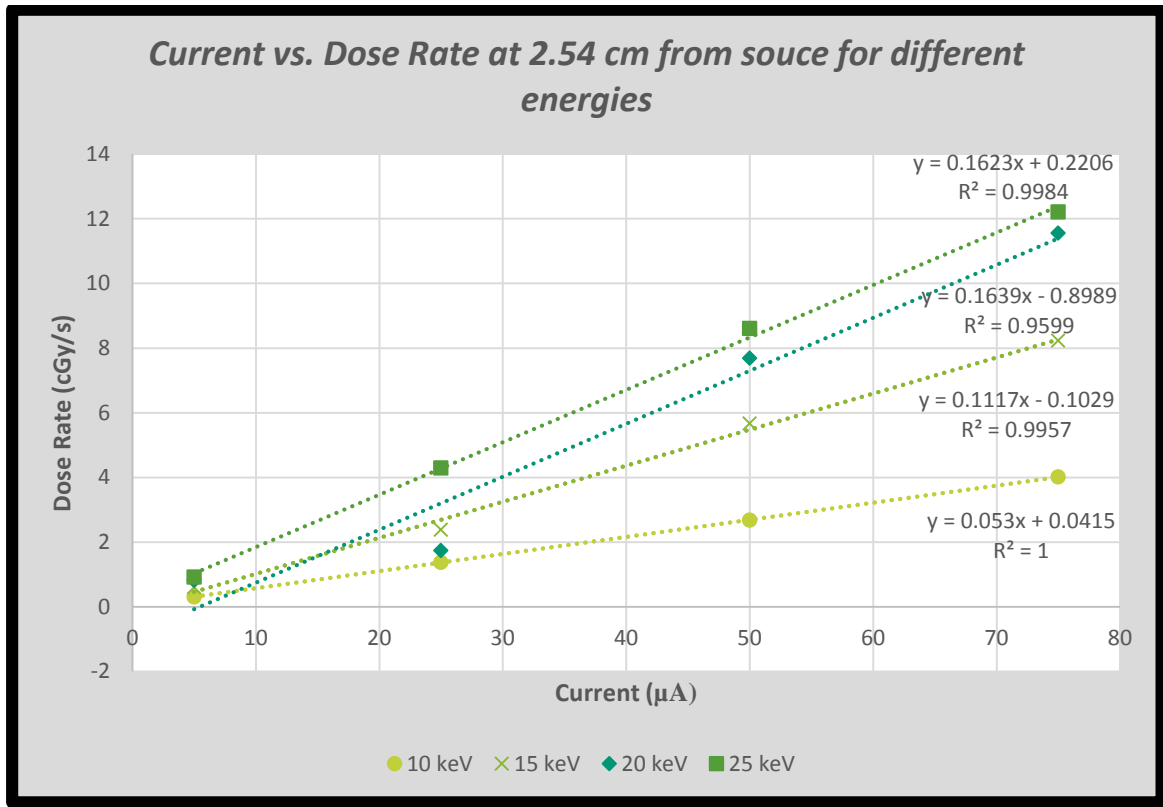


*Figure 6.24: Current vs. Dose for different energies*

The effect of different collimators on the dose rate was also investigated and the resultant findings from this experiment is summarized in Figures 6.25 and 6.26. Figure 6.26, gives an easier indication of how the dose rate changes as a function of the beam size. As evident Figure 6.26, the dose rate decreases the most as the change is made from no collimator to 2 mm collimator. This is to be expected since the setup involving no collimator and 2 mm collimator represent the biggest and smallest beam sizes obtainable respectively. However, an interesting deduction from this particular investigation is that the dose rate decreases quite sharply as one moves from 3 mm to 2 mm collimator and in addition, the factor by which dose the rate decreases does not stay constant over all distances. This is important information that would be extremely useful in the planning of future biophysical measurements.

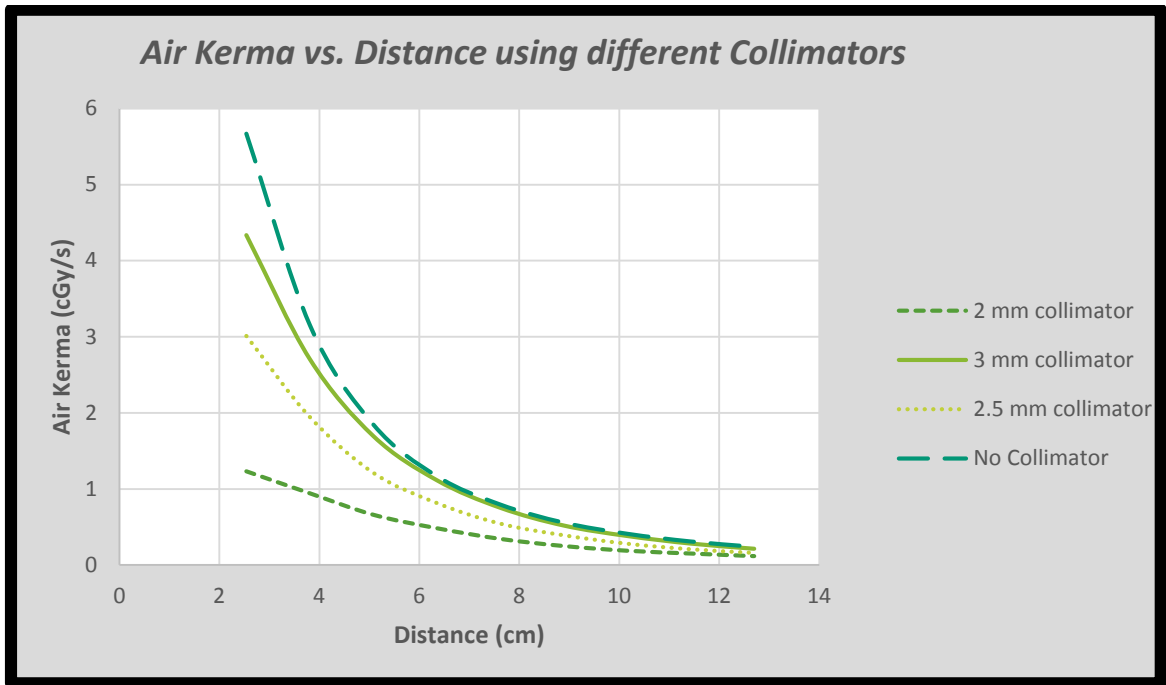


*Figure 6.25: Graph comparing the dose rates obtained using different collimators*

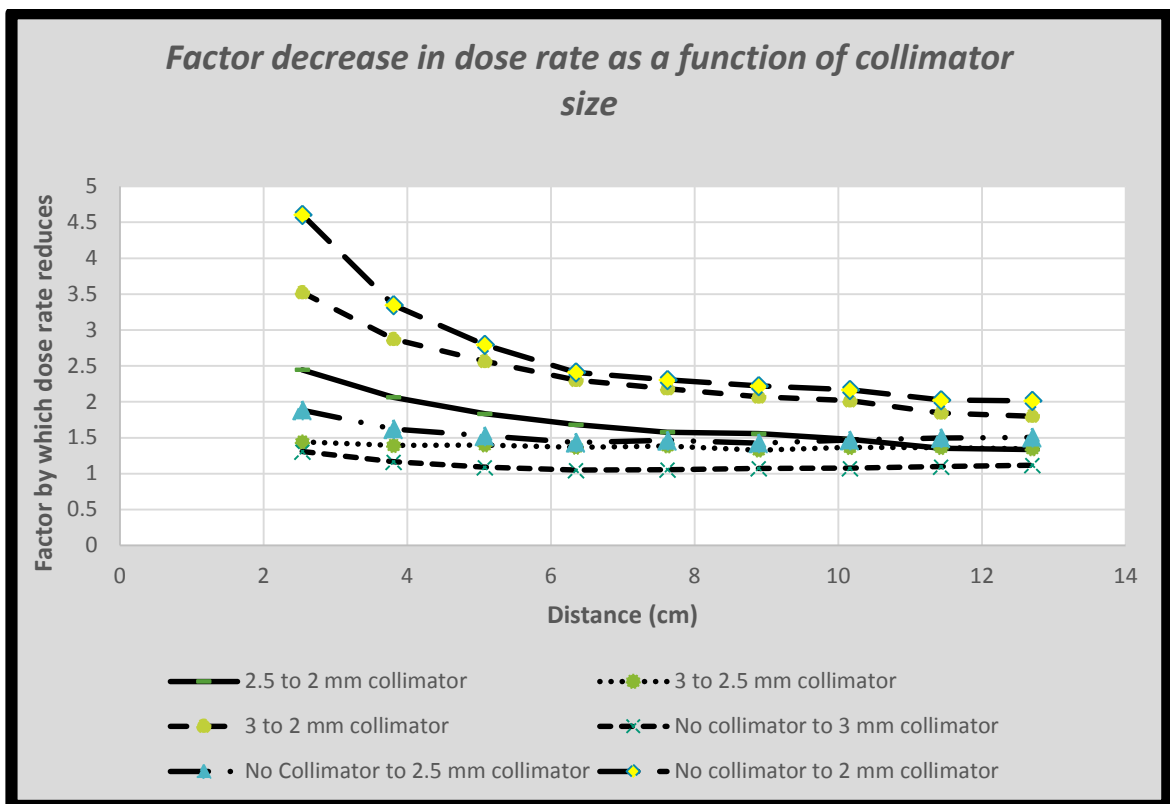


*Figure 6.26: Change in dose rate as function of beam size*

### 6.3.2 Dose to Tissue

Although air-kerma values have been established, from a biological standpoint air-kerma values do not provide the complete information since the energy released refers to air and not tissue and hence, they must be converted to absorbed dose to tissue to be more relevant for experimental radiation biophysics. Dose to air can be converted to dose to tissue via the following formula:

$$Dose\ Rate\ (Tissue) = Dose\ Rate\ (Air) * (\mu_{en}/\rho)^{tissue} / (\mu_{en}/\rho)^{air} \quad [6.4]$$

Here  $(\mu_{en}/\rho)^{tissue}$  represents the average mass energy absorption coefficient in tissue for the X-Ray spectrum used while  $(\mu_{en}/\rho)^{air}$  represents the average mass energy absorption coefficient in air. It should be noted that these mass energy absorption coefficient values are dependent on the energy of the X-Rays and change as a function of energy. To estimate the dose to tissue, the mass energy absorption coefficient values for water were used since they provide a good estimate for the mass energy absorption coefficient values of tissue. Using the data provided by the 'National Institute of Standards and Technology' (NIST) the relationships between the mass energy absorption coefficients and energy for both the media (air and water) were established [24 & 25]. Figures 6.27 and 6.28, show the relationship between  $\mu_{en}/\rho$  and energy for air and water respectively. Since the X-Ray source produces a continuous spectrum at varying energies it is required to find the average mass energy absorption coefficient value for a given spectrum, both in air and water. This is because a continuous spectrum consists of a range of energies for which the  $\mu_{en}/\rho$  value changes as a function of energy. Therefore, it is required to establish the relationship between  $\mu_{en}/\rho$  and energy such that it can be used to find the  $\mu_{en}/\rho$  value at each given energy for a given spectrum. Based on the data available from NIST, the relationship

between  $\mu_{en}/\rho$  and Energy can be defined by equations 6.5 and 6.6 for water and air respectively.

$$\mu_{en}/\rho(\text{Water}) = 4822.4 * (\text{Energy})^{-3.002} = \frac{\text{cm}^2}{\text{g}} \quad [6.5]$$

$$\mu_{en}/\rho(\text{Air}) = 4165.8 * (\text{Energy})^{-2.964} = \frac{\text{cm}^2}{\text{g}} \quad [6.6]$$

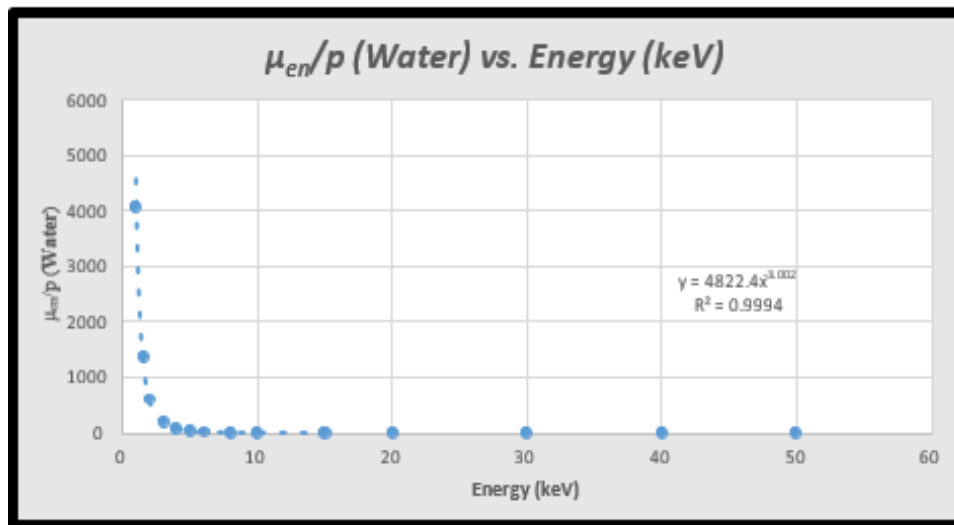


Figure 6.27: Graph showing relationship between  $\mu_{en}/\rho$  (Water) and Energy [24]

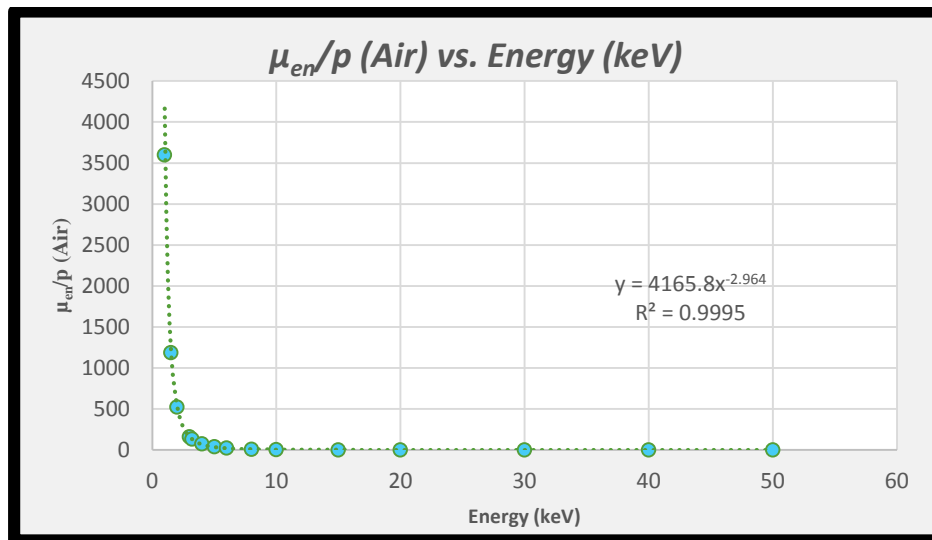
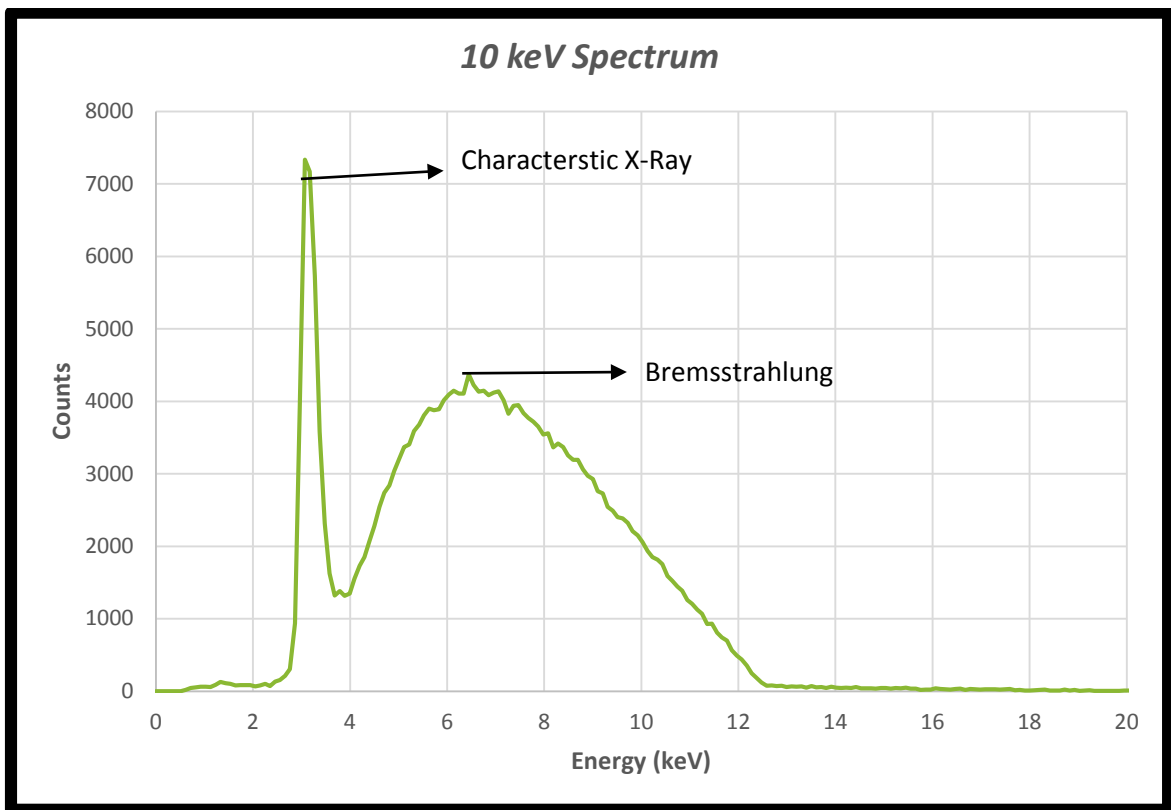
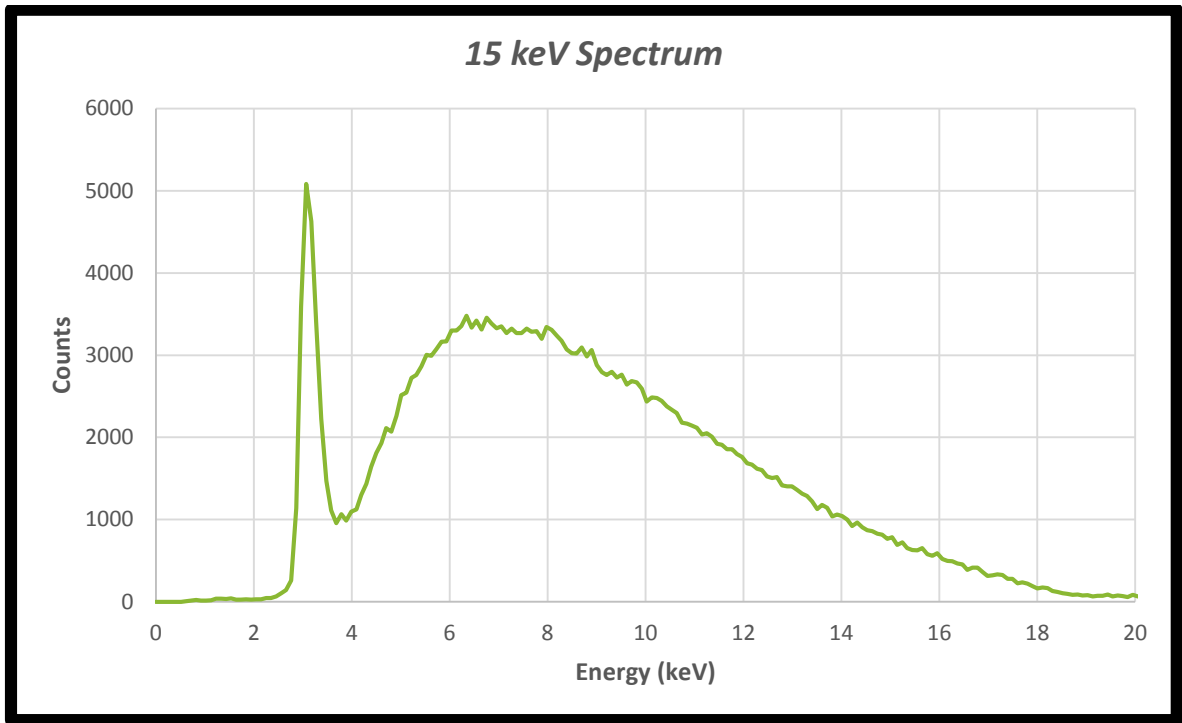


Figure 6.28: Graph showing relationship between  $\mu_{en}/\rho$  (Air) and Energy [25]

The next step for determining the dose to tissue was to obtain the photon energy spectra from the Mini-X. To do this, spectra at varying energies were obtained using the Amptek X-123 spectrometer. Figures 6.29 to 6.33, show the spectra at energies of 10 keV, 15 keV, 20 keV, 25 keV, and 30 keV respectively. As evident from the spectra, they consist of sharp defined peaks and a continuous region. The sharp defined peaks are referred to as characteristic X-Rays and carry an energy characteristic of the target material, while the continuous region of the spectrum represents the bremsstrahlung production. Figure 6.29 clearly defines the characteristic and the bremsstrahlung regions of a spectrum.



*Figure 6.29: Energy spectrum at 10 keV*



*Figure 6.30: Energy spectrum at 15 keV*

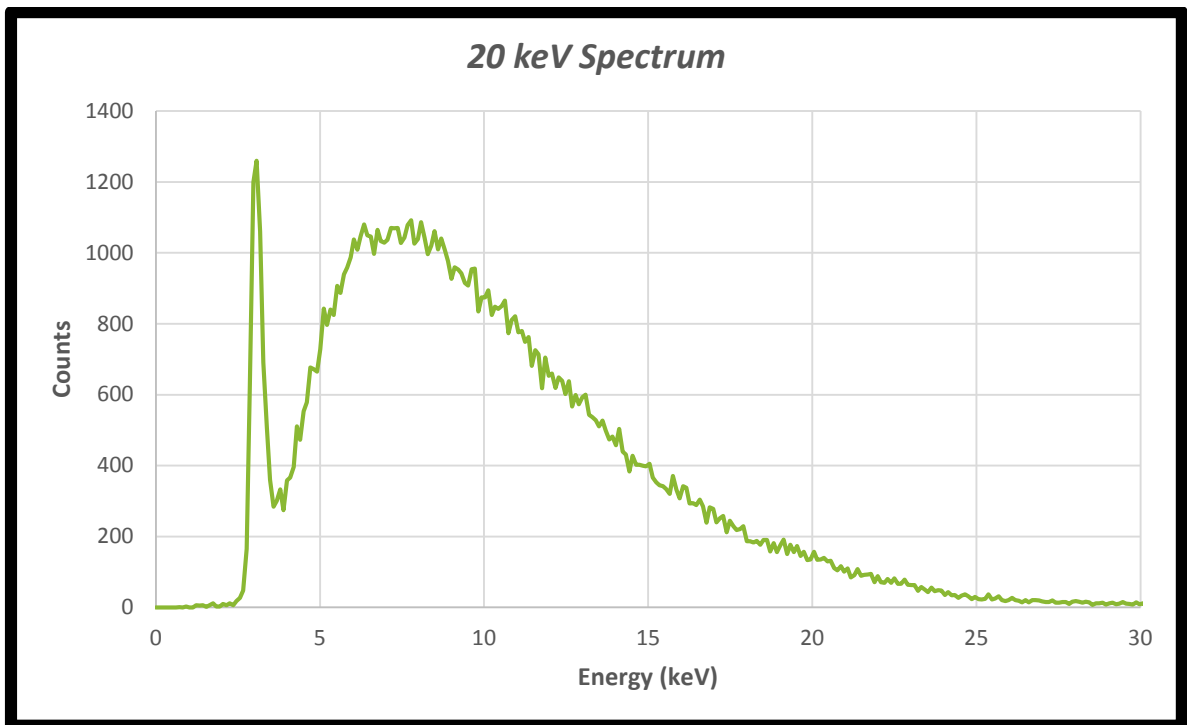


*Figure 6.31: Energy Spectrum at 20 keV*

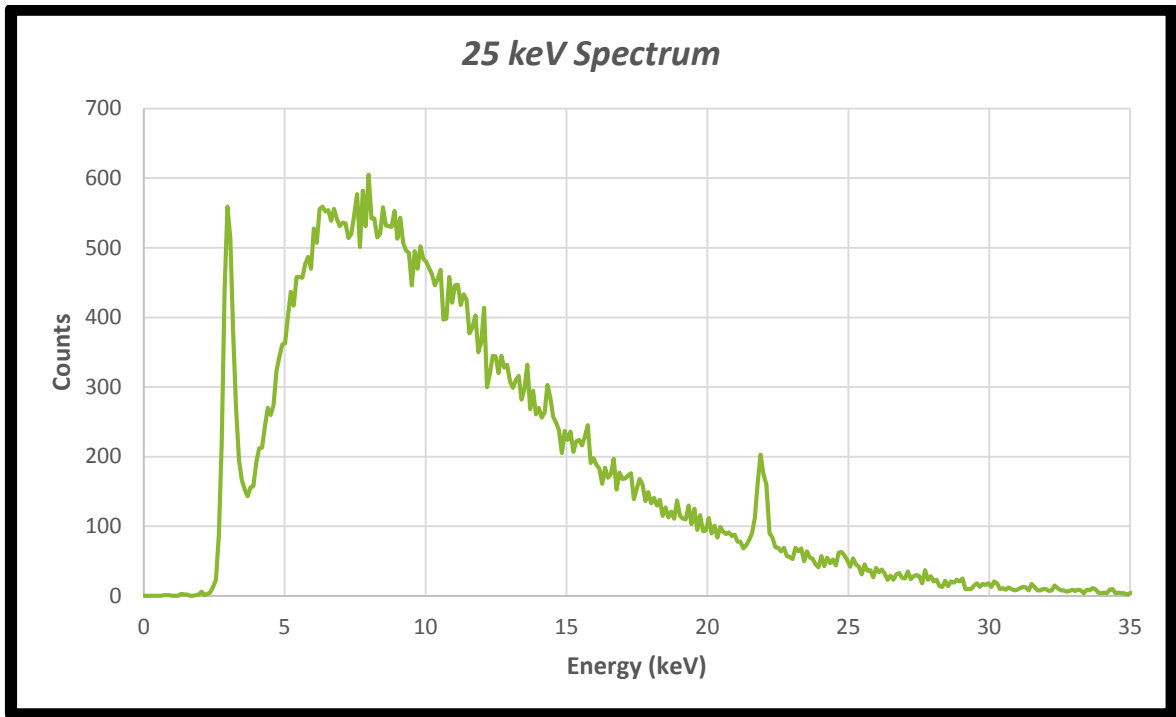


*Figure 6.32: Energy spectrum at 25 keV*

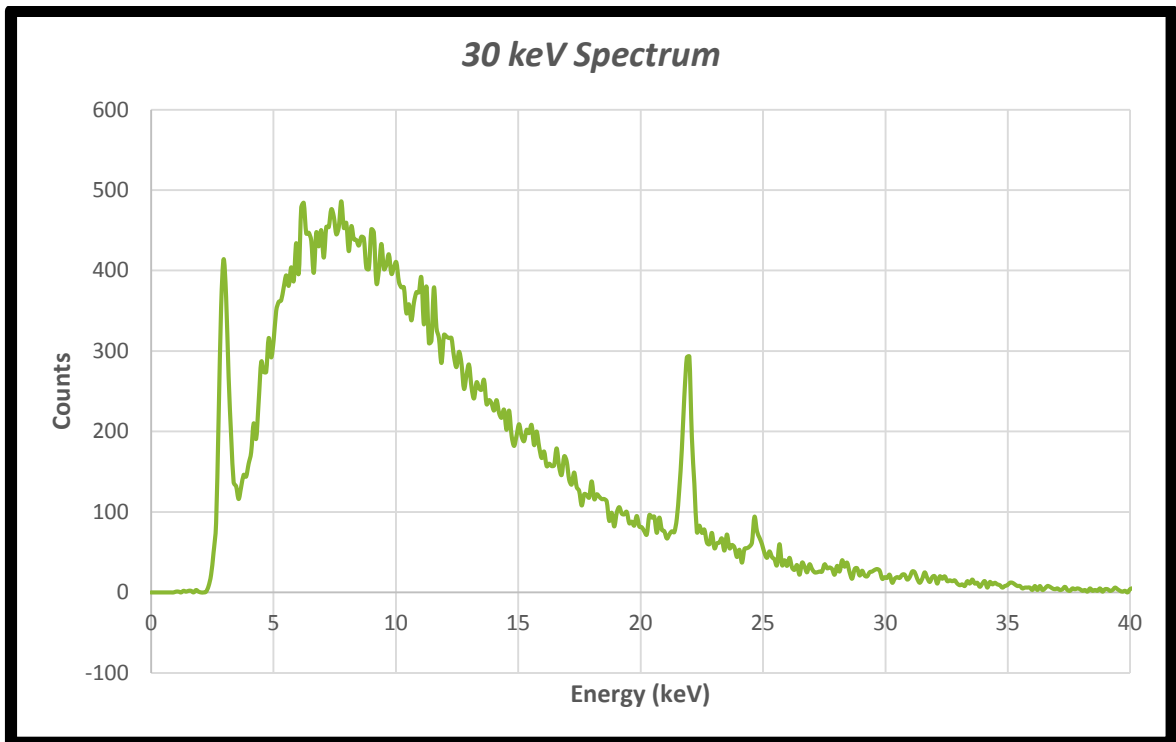


*Figure 6.33: Energy spectrum at 30 keV*

*Table 6.1: Characteristic X-Rays and Bremsstrahlung Energies for different spectra*

<i>Energy</i>	<i>Characteristic X-Ray</i>	<i>Mean Bremsstrahlung Energy</i>
10 keV	3.151 keV	6.6495 keV
15 keV	3.151 keV	6.7518 keV
20 keV	3.151 keV	7.748 keV
25 keV	3.151 and 21.995 keV	8.0817 keV
30 keV	3.151, 21.995 and 24.653 keV	7.775 keV

Table 6.1 lists the characteristic X-Ray peaks and mean bremsstrahlung energies observed for different spectra. It should be noted that the L-Series silver characteristic energy peak was observed at slightly different energies for different spectra. Silver has  $L\alpha_1$  and  $L\alpha_2$  peaks at 2.985 and 2.979 keV, respectively, and also has an  $L\beta_1$  peak at 3.151 keV. A 3.151 keV peak was observed for all the spectra and in addition to this, 21.995 and 24.653 keV peaks were observed at 25 keV and 30 keV spectra. These two peaks are the K-Series characteristic X-Ray peaks since silver has a  $K\beta_1$  peak at 24.943 keV and a  $K\alpha_2$  peak at 21.991 keV. In addition to this, the mean bremsstrahlung energy increased as a function of energy with exception of 30 keV. The mean bremsstrahlung energy at 30 keV was observed at 7.775 keV as compared to 8.0817 keV at 25 keV. This observed bremsstrahlung peak difference explains why the dose rate decreases slightly as one moves from 25 keV to 30 keV. For example, at 25 keV and 75 $\mu$ A a dose rate of 12.21 cGy/s was

observed at 2.54 cm (1 inch) from the source as compared to 12.13 cGy/s observed at same distance at 30 keV and 75 $\mu$ A.

It should also be noted that the maximum energy of the spectrum for all the energies is slightly higher than expected. For example, in the 10 keV spectrum the maximum energy 'cut off' is at 12.5 keV instead of 10 keV. This discrepancy might be caused by phenomenon called pulse pileup which occurs when simultaneous pulses arrive much closer than the resolution time of the pulse processing system. To give an example, if two pulses arrive very close to each other, the system would simply register the two pulses as a single piled up event and therefore, produce an erroneous output. This effect will be more probable when the count rate from the radiation source is high which would prevent the detector to 'recover' between two pulses [26]. It should be noted that to reduce the count rate and minimize the dead time effect a brass collimator with a 0.05 cm orifice was used on the spectrometer (see Figure 6.34). For example, at 10 keV the detector registered a dead time of almost 99 % without the collimator but, with the collimator the dead time was brought down to less than 10 %. In addition, the detector was placed at a distance of 12.7 cm from the source and the Mini-X was run at the lowest current of 5  $\mu$ A to further reduce the count rate and minimize the dead time. Figure 6.35, shows how the experimental data obtained compares with the expected data simulated using MCNP. This graph is taken from a preliminary study done at UOIT that shows experimental and simulated spectra from Mini-X at 20 keV with an Iron filter. As evident from the graph there is a clear shift in the bremsstrahlung portion of the spectrum by a few keV, while the Characteristic X-Ray energy peaks from either setup are in good agreement.

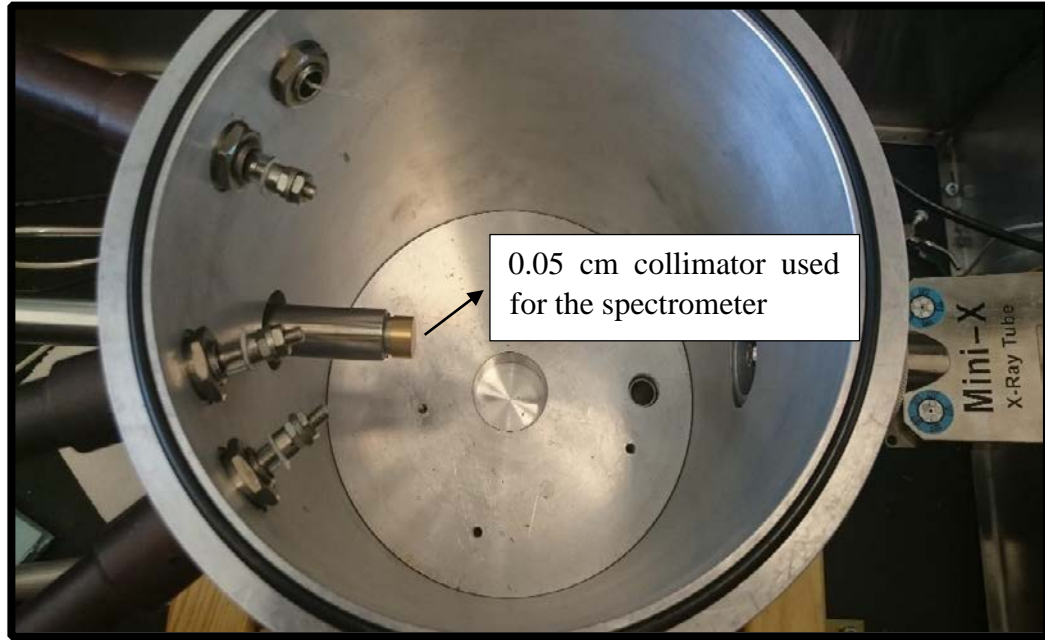


*Figure 6.34: The X-123 spectrometer with brass collimator*

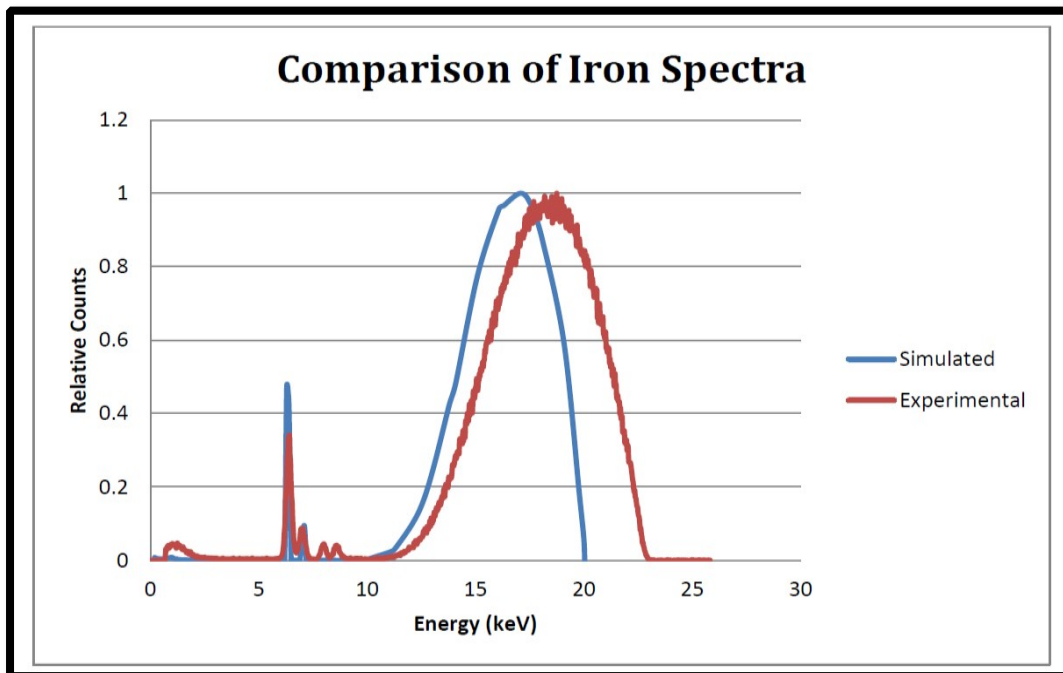


*Figure 6.35: Simulated and Experimental Mini-X spectra at 20 keV using iron filter [8]*

The next step to obtain absorbed dose to tissue was to find the energy probability distribution from the spectra, P (E). The parameter P (E) defines the probability of finding a given energy in the spectrum. This is required since the mass energy absorption coefficient values differ for different energies in a given medium. To find the P (E) value the following formula can be used:

$$P (E) = \frac{\text{Counts (E)}}{\text{Total Counts}} \quad [6.7]$$

Here Counts (E) refer to number of counts obtained at a given energy while the total counts refer to the total number of counts obtained over all the energies. Once the P (E) values are established they can be multiplied with the mass energy absorption coefficient value for that specific energy. Again the mass energy absorption coefficient values in air and water can be found using the equations in Figure 6.27 and Figure 6.28. Mathematically the average mass energy absorption coefficient for a given medium can be found using the equation below:

$$\mu_{en/p} (\text{Water}) \text{ Average} = \sum [P (E) * \mu_{en/p} (E)] \quad [6.8]$$

A similar approach can be used to find the average mass energy absorption coefficient value in air and once both the values are deduced, the resultant dose to tissue can be found by simply taking the ratio of the two mass attenuation coefficients and multiplying it by the air-kerma value for a given energy. For low energy electrons this ratio is expected to be close to 1 and hence similar values are expected for air-kerma and dose to tissue.

The results obtained for dose to tissue are described in Figures 6.36 to 6.40. The graphs establish a comparison between dose to tissue and air-kerma values. Furthermore,

Figure 6.40 plots the mass attenuation ratios as a function of energy. As evident from the graph the ratios are fairly close to the expected value of 1. Based on these graphs (Figures 6.36-6.40) it is quite clear that there is not a substantial difference between the air-kerma and dose to tissue values. This difference between the dose to tissue and air-kerma values is highlighted in table 6.2. The table shows that the percent difference between the air-kerma and dose to tissue values decreases with increasing energy.

*Table 6.2: Comparison between Air Kerma and Dose to Tissue*

<i>Energy (keV)</i>	<i>Percent difference in Air Kerma and Dose to tissue</i>
10	9.12
15	8.58
20	8.05
25	7.89

To find the percent difference between the two the following equation was used:

$$\text{Percent Difference} = \frac{[Dose(Air) - Dose(Tissue)]}{Dose(Air)} \quad [6.9]$$

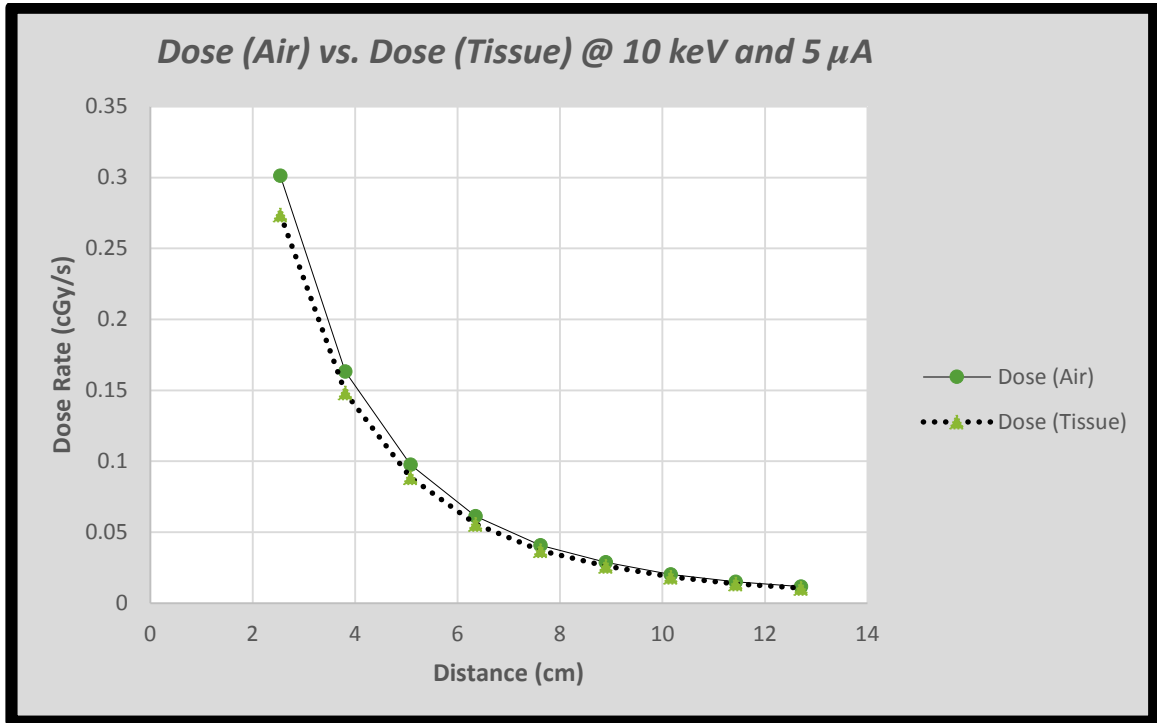


*Figure 6.36: Dose in Tissue vs. Dose in Air @ 10keV and 5  $\mu$ A*

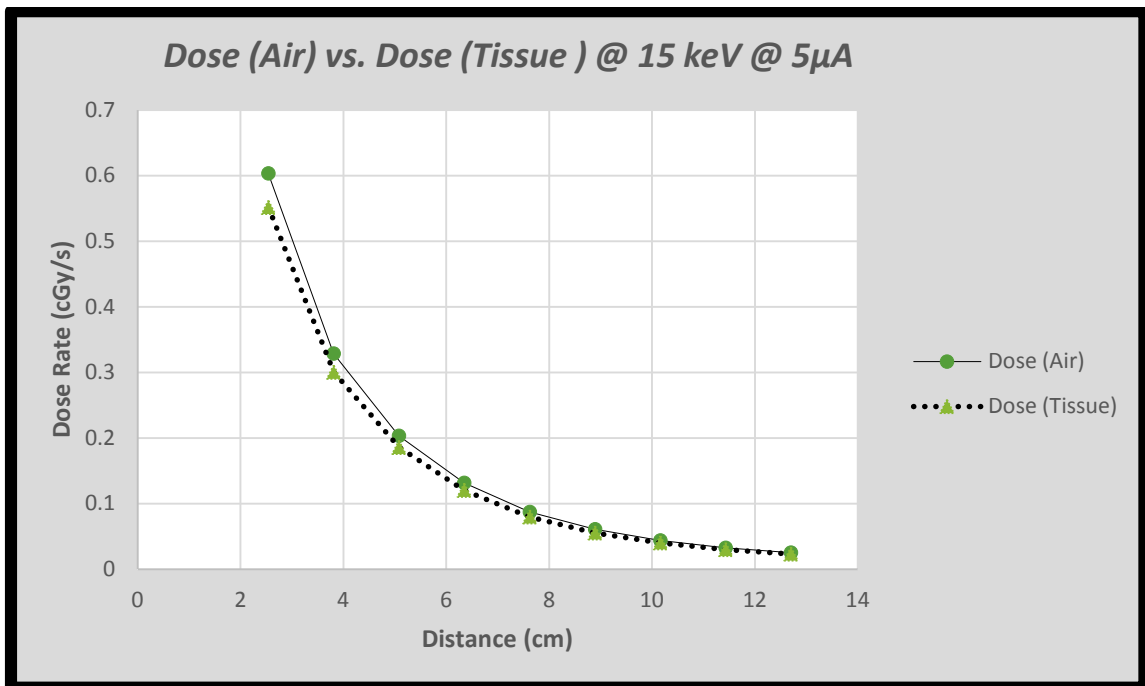


*Figure 6.37: Dose in Tissue vs. Dose in Air @ 15 keV and 5  $\mu$ A*

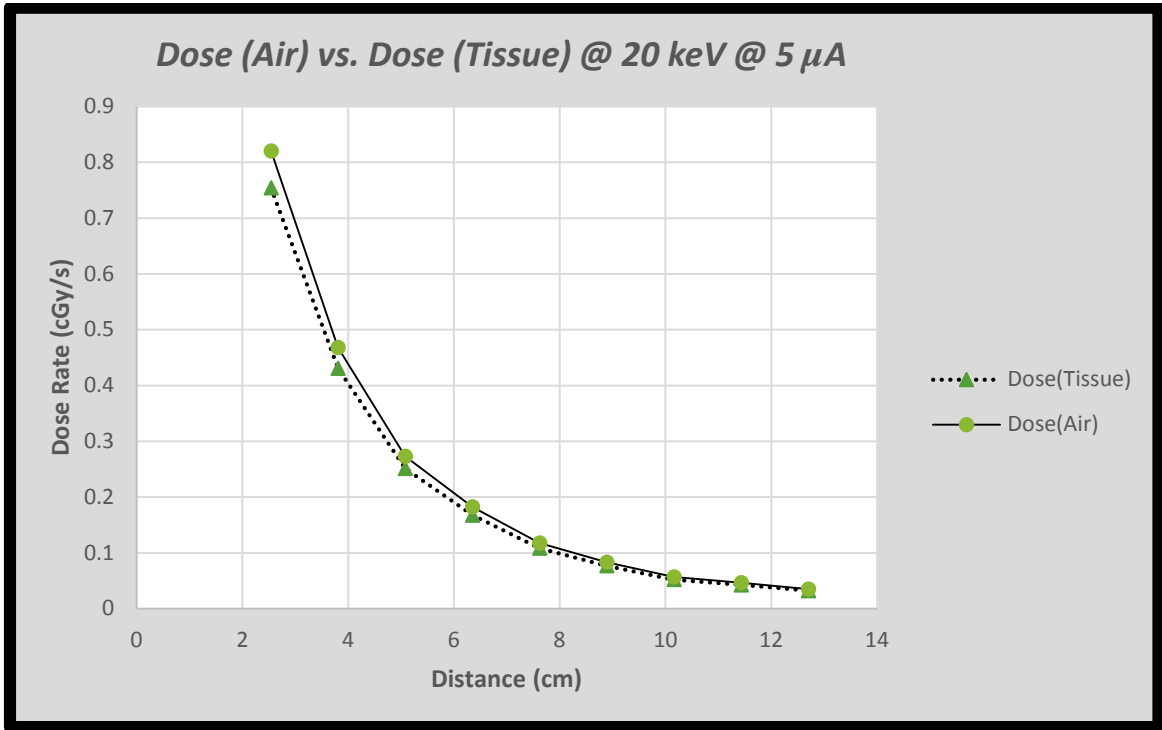


*Figure 6.38: Dose in Tissue vs. Dose in Air @ 20 keV and 5  $\mu$ A*

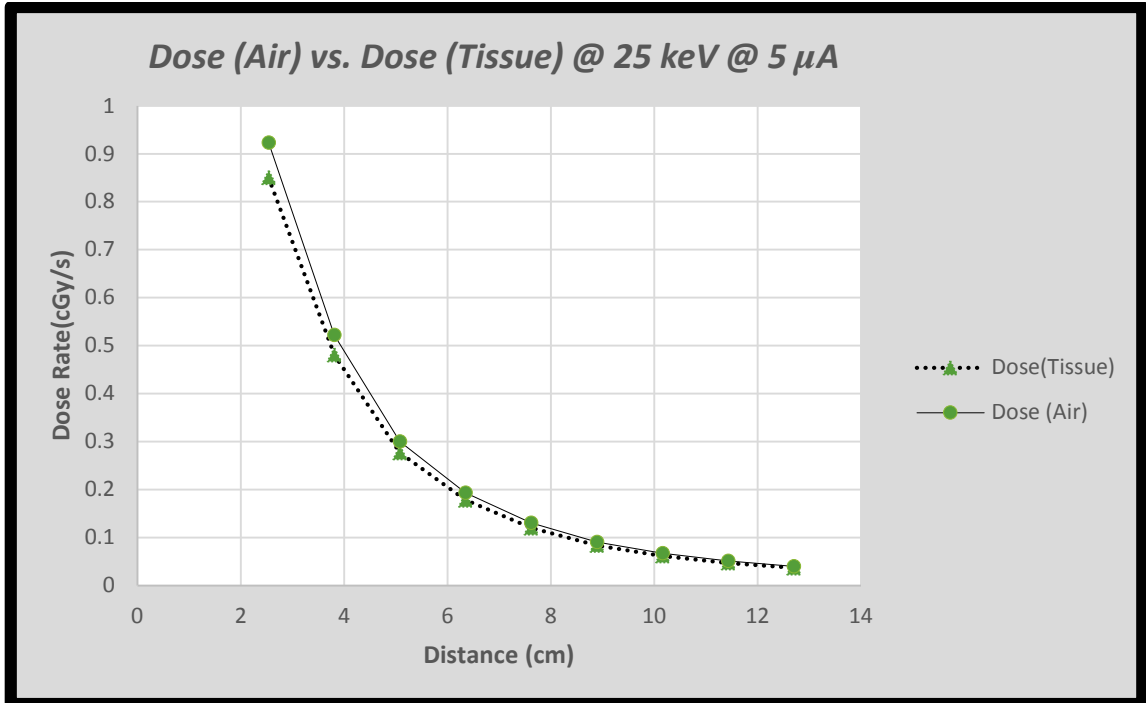


*Figure 6.39: Dose in Tissue vs. Dose in Air @ 25 keV and 5  $\mu$ A*

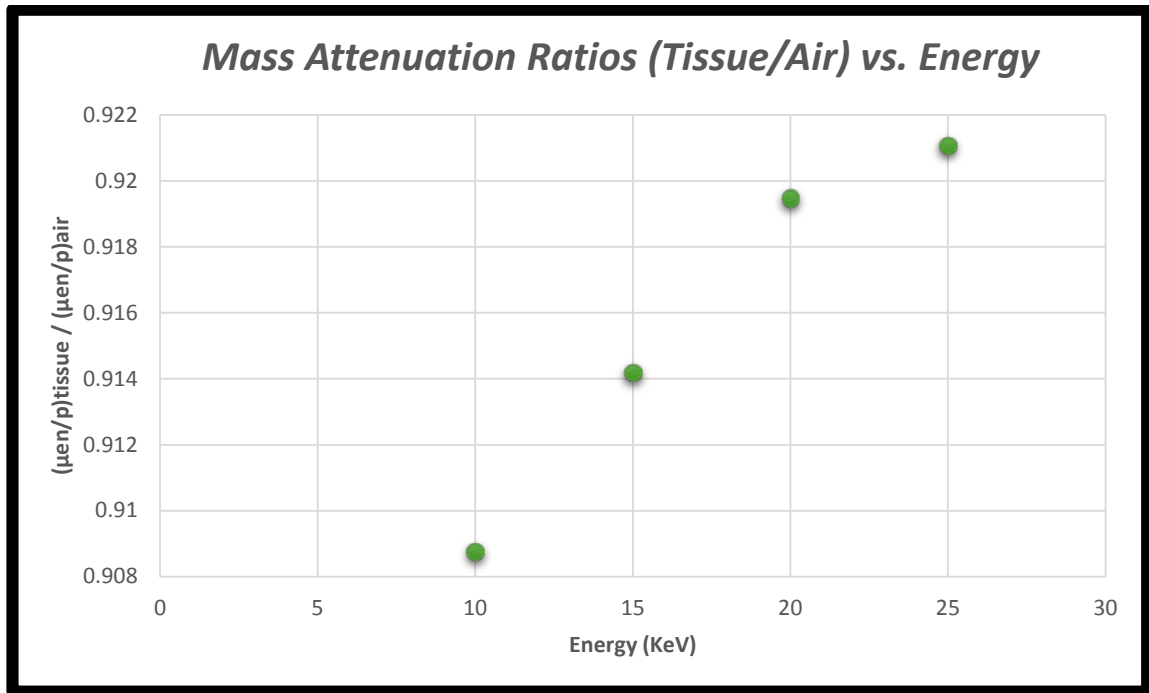


*Figure 6.40: Mass attenuation ratios (Tissue/Air) vs. Energy*

## 6.4 Cross calibration of A-20 Ionization Chamber and Landauer’s OSL nanoDots

### 6.4.1 Introduction

After characterizing the X-Ray source, the next part of the project was to establish a cross calibration curve between Exradin’s A-20 ionization chamber and Landauer’s OSL nanoDots. OSL nanoDots are proposed to be used for the future extension of this project where a biophysics experiment would be carried out using the Mini-X.

For the proposed biophysics experiment, fish eggs would be used and a detector suitable for operation in an aqueous environment is required. However, the A-20 ionization chamber is limited for in-air use and an alternate dosimeter is required for in-water dosimetry. In addition, another limitation of A-20 ionization chamber is that at a given time it only provides dose information of a single point in space and does not give a

complete picture of the spatial distribution of the incident beam. OSL nanoDots due to their extremely compact design, can be placed at various spots over the experimental setup and hence, can be used to find the spatial distribution of the incident beam. It should be noted that OSL nanoDots are not calibrated at the operational X-Ray energies of this study, hence the OSL response is not known.

Therefore, this part of the study is aimed to compare the OSL response with A-20 ionization chamber and establish a cross calibration curve that could be used to find the absorbed dose during the biophysical experiments. It should be noted that this part of the experiment was done in conjunction with Margarita Tzivaki, a PhD student at UOIT and all the dosimetric measurements using the nanoDots were carried out by Ms. Tzivaki while the measurements using the A-20 ionization chamber were carried out by the writer of this report [Margarita Tzivaki, Personal Communication, June, 2015].

#### **6.4.2 Experimental Setup and Landauer's OSL nanoDots**

Figure 6.41 shows the physical size of the nanoDot and as the image suggests each nanoDot is square in shape with side length of 1 cm.

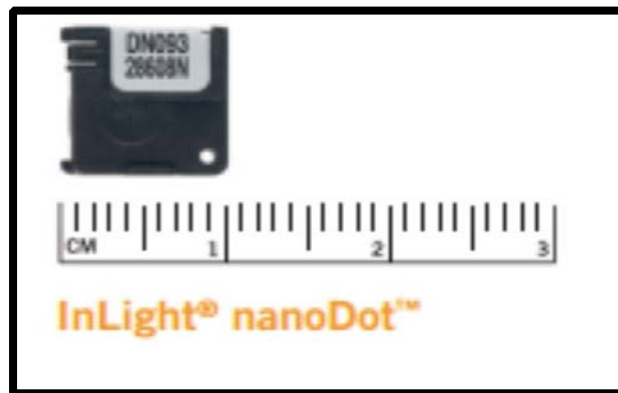


*Figure 6.41: Landauer's InLight nanoDot [26]*

These nanoDots can be read by using Landauer's MicroStar reader which works on the principles of optically stimulated luminescence to measure the absorbed dose received by exposed nanoDots. The complete setup is shown in Figure 6.42 and the setup includes a barcode scanner, Landauer's microStar reader and the attached laptop onto which the output from MicroStar reader is registered. Each nanoDot has its own unique barcode and requires ten minutes of settling time after exposure before they can be read by MicroStar reader.

The MicroStar reader is a light and portable reader that uses aluminum oxide OSL detectors with carbon doping ( $\text{Al}_2\text{O}_3:\text{C}$ ) to measure an exposure [27]. The fundamental working principle of nanoDots is similar to that of thermoluminescent detectors (TLDs), since the nanoDots also consists of a crystal that results in formation of electron-hole pairs after it is exposed to radiation.

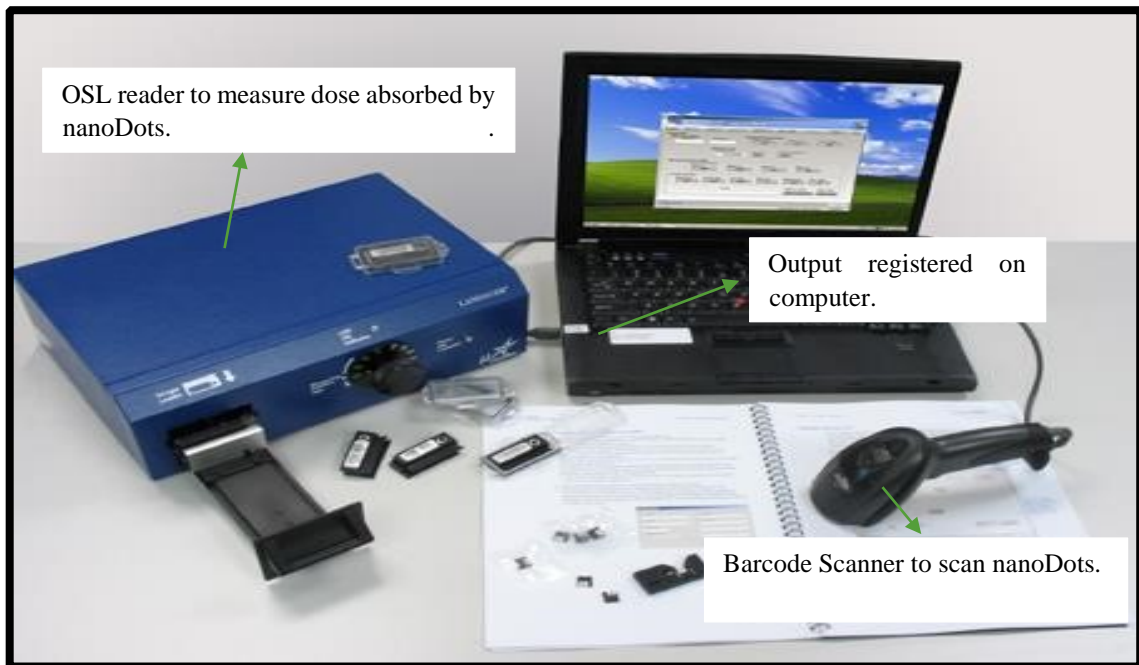


*Figure 6.42: Image showing complete setup involving the nanoDots and the microStar reader [27]*

The formation of these electron pairs inside the crystal is influenced by a phenomenon called crystal defect which as the name suggest, is an imperfection in the regular geometrical arrangement of the atoms in a crystalline solid. Figure 6.43 illustrates this concept further which shows the formation of an electron hole pair within the forbidden energy gap of the crystal lattice. The forbidden energy gap is located within the conduction and valence band of the crystal lattice. Upon further exposure of the crystal to heat, these electron hole pairs recombine thereby, resulting in an emission of a photon. The optical flux given off from the crystal is directly proportional to the amount of dose absorbed by the nanoDot and hence, allows the user to measure the absorbed dose. It should be noted that this example illustrates the working of a typical TLD but, the same principle is applicable for OSL as well since they use light instead of heat to facilitate this recombination process [28].

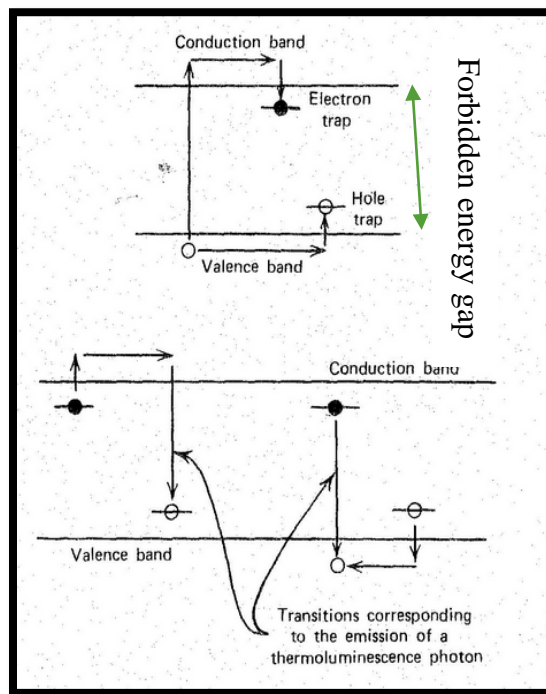


*Figure 6.43: Summary of the process of emission of thermoluminescence photon [28]*

Furthermore, the entire setup is calibrated such that the output from nanoDots is given in terms of absorbed dose to tissue. Since nanoDots are not an absolute method of dosimetry they need to be calibrated against a dosimeter of known response in order for them to be used for dosimetry. Therefore, as a final part of this project, nanoDots were calibrated against the A-20 ionization chamber and an OSL calibration curve was established. Figure 6.44 shows the vial where the biological material (fish eggs) would be placed and also highlights the place where the nanoDots would be placed for dosimetry purposes.

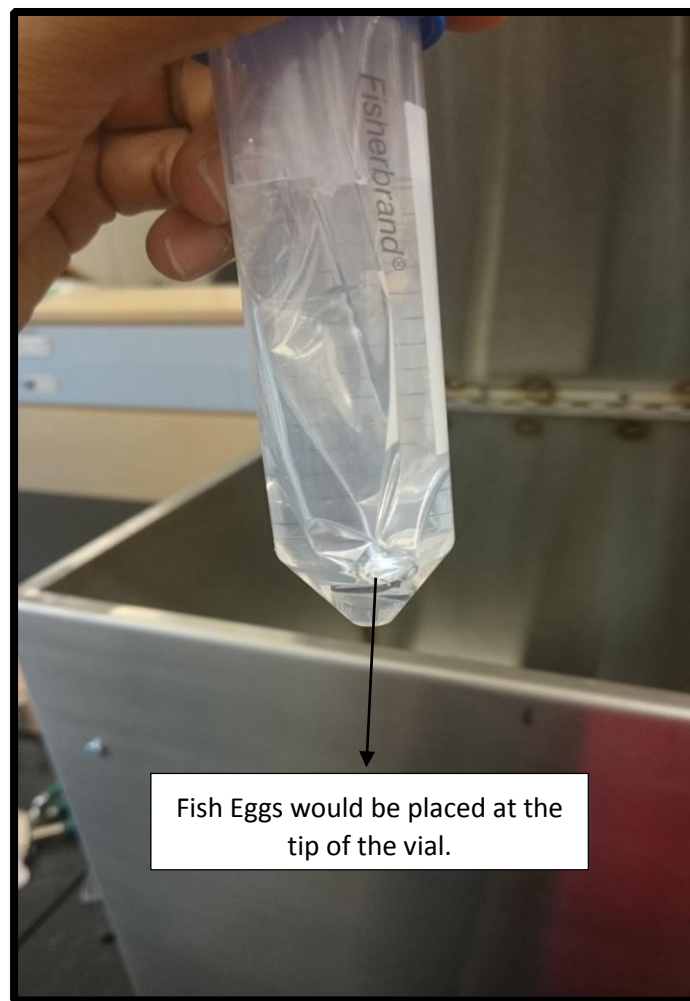


*Figure 6.44: Vial housing the fish eggs for proposed biophysics experiment*

The proposed setup for the biophysics experiment can be seen in Figure 6.45. Here a set of clamps are used to hold the vial housing the fish eggs and the tip of the vial is positioned such that it is directly opposite the Mini-X. In addition, the X-Ray source would be used without the screw on brass cover in order to ensure complete coverage of the target area. As stated earlier, a 120° beam can be achieved without the brass cover and the dose rate delivered to the fish eggs can be adjusted simply by changing the distance between the vial and the X-Ray source. However, before this can be done the nanoDots need to be calibrated against the A-20 ionization chamber. As a part of the calibration process the dose rate from A-20 ionization chamber was compared to the dose rate from nanoDots and a resultant calibration curve was obtained. This calibration curve can be used to determine the actual dose delivered to the fish eggs by looking at the dose absorbed by nanoDots.



*Figure 6.45: Proposed experimental setup for the biophysics experiment using fish eggs*

### 6.4.3 Results-Cross Calibration Curve

The first part of the calibration experiment was to compare the dose rates obtained from each of the two dosimeters. The dose rates were measured as a function of the Mini-X energy and energies were increased from 10 keV to 30 keV by an incremental factor of 2.5 keV (@ 100  $\mu$ A). The results obtained can be seen in Figures 6.46 and 6.47 respectively, which shows the dose rate in mGy/s as function of X-Ray energy (keV). As expected from the previous observed trends the dose rate obtained from both the dosimeters flattened out after 25 keV. In addition, the comparison between the doses obtained from each dosimeter is shown in Figure 6.48. Lastly, Figure 6.48 shows the ratio of the dose rates obtained from the A-20 ionization chamber to OSL nanoDots as a function of energy (keV).

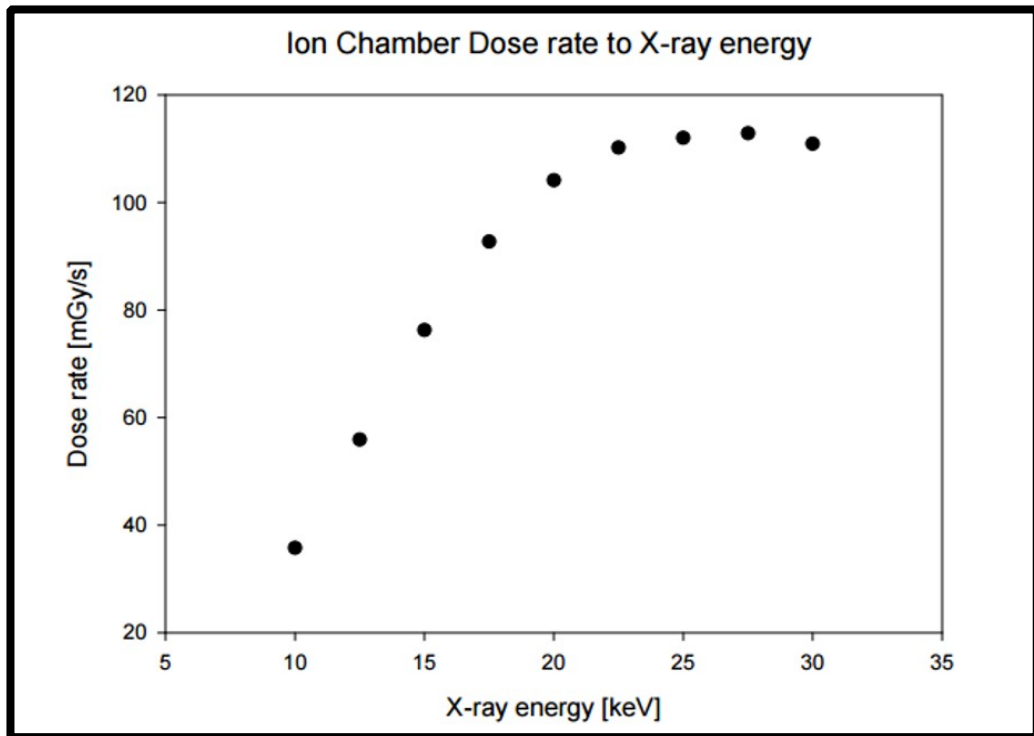


*Figure 6.46: Dose Rate as a function of Energy at 100  $\mu$ A current using the A-20 ionization chamber [Margarita Tzivaki, Personal Communication, June 2015]*

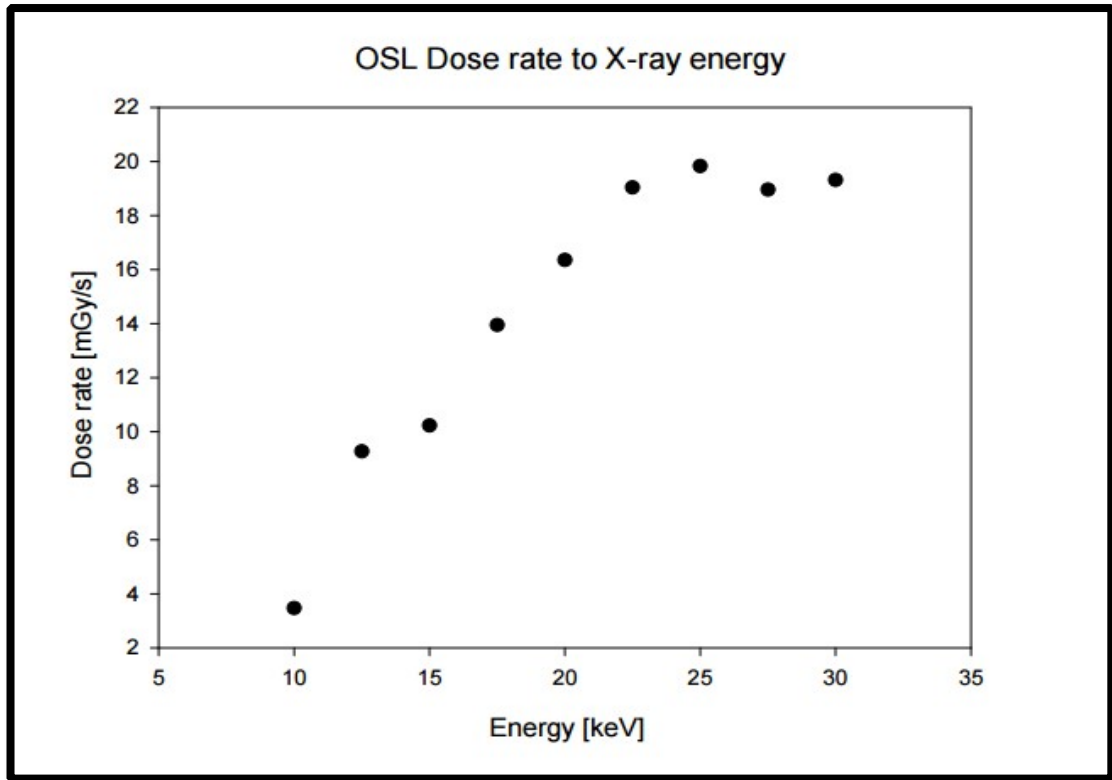


*Figure 6.47: Dose Rate as a function of Energy at 100  $\mu$ A current using the OSL nanoDots [Margarita Tzivaki, Personal Communication, June 2015]*

It was observed that the dose rates obtained from OSL were significantly lower as compared to the A-20 ionization chamber. For example at 10 keV, the dose rate measured by OSL was roughly ten times lower than that of ionization chamber. Furthermore, this factor does not stay constant for all the energies since the ratio decreases with increase in energy. For example, this ratio decreases to 7.45 as one moves from 10 keV to 15 keV and further decreases to 5.74 for 30 keV energies. Overall, the dose rate trends observed from each of the two dosimeters stay the same since both the detectors give a polynomial trend when dose rate is compared to energy. This trend is clearly evident in Figure 6.46 and 6.47. All the measurements were taken at 5.08 cm from the source.

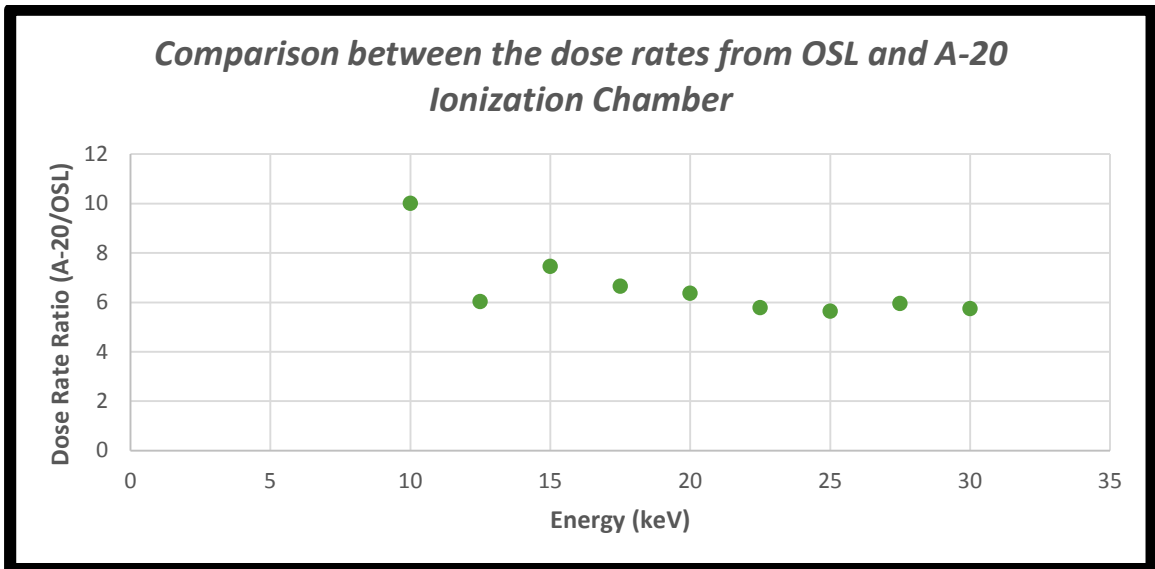


*Figure 6.48: Dose Rate ratio (Ionization Chamber/OSL nanoDots) plotted as a function of Energy*

The same measurement process was repeated with 200  $\mu\text{A}$  tube current and the dose rates from the two dosimeters were compared to establish the calibration curve. Figures 6.49 and 6.50, show the comparison between the dose rates at 100  $\mu\text{A}$  and 200  $\mu\text{A}$  respectively. These calibration curves show a fairly linear relationship between the dose rates obtained from each of the two dosimeters and can be used to determine the dose delivered to fish eggs via interpolation. Both the 100  $\mu\text{A}$  and 200  $\mu\text{A}$  currents were used to obtain a curve at ‘low-dose rates’ and ‘high-dose rates’ respectively. Considering the proposed biophysics experiment and factoring in attenuation from water and plastic shielding of the vial, 200  $\mu\text{A}$  would be the appropriate current operating range, as higher dose rates can be obtained with this setup which subsequently reduces the run time of the Mini-X. A strong linear relationship was observed for the two calibration curves (as evident from the high  $R^2$  values), suggesting the calibration curves were adequate for calibrating OSL nanoDots.

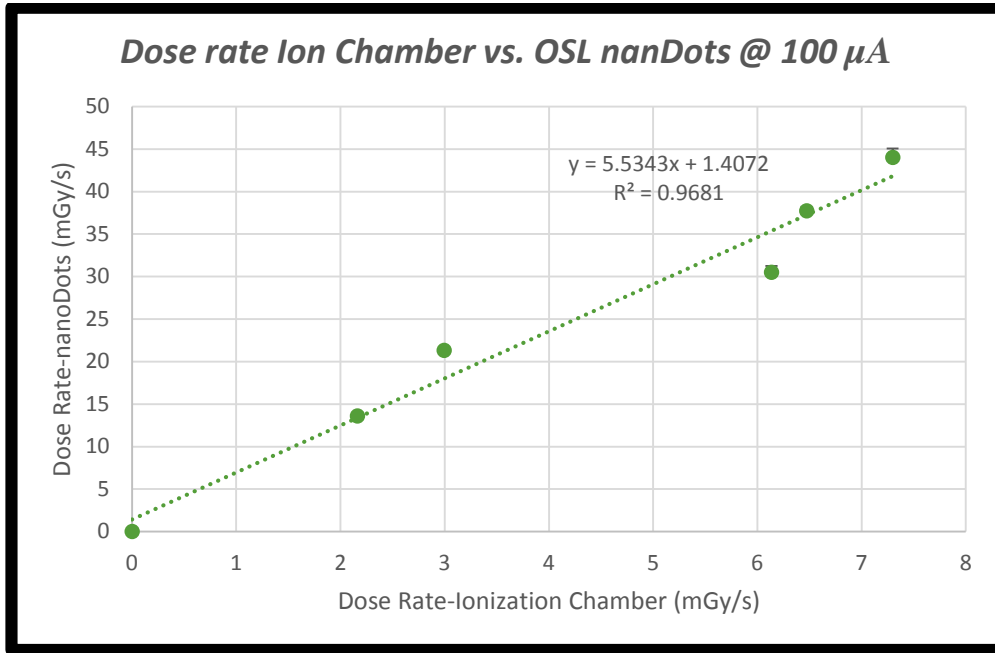


*Figure 6.49: Dose Rate comparison between nanoDots and ionization chamber at 100  $\mu$ A tube current [Margarita Tzivaki, Personal Communication, June 2015].*

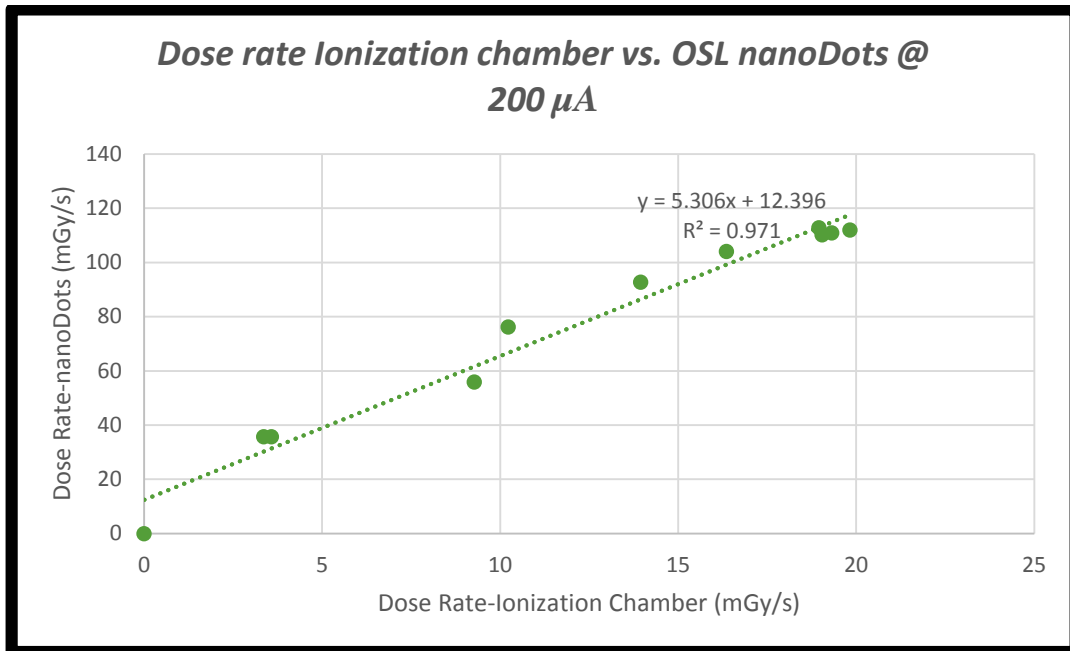


*Figure 6.50: Dose Rate comparison between nanoDots and ionization chamber at 200  $\mu$ A tube current [Margarita Tzivaki, Personal Communication, June 2015].*

The approach to find the beam profile using nanoDots was similar to the approach used with radiochromic films. For this part of the project a 10 keV beam was used at 100  $\mu$ A and nanoDots were placed on a square petri dish at set distances from the source to find the beam profile. Figure 6.51 shows the schematic of the petri dish and the placement of the nanoDots on the petri dish. The black squares here represent the nanoDots facing the X-Ray beam. The results from this experiment are outlined in Figures 6.52 and 6.53 respectively.

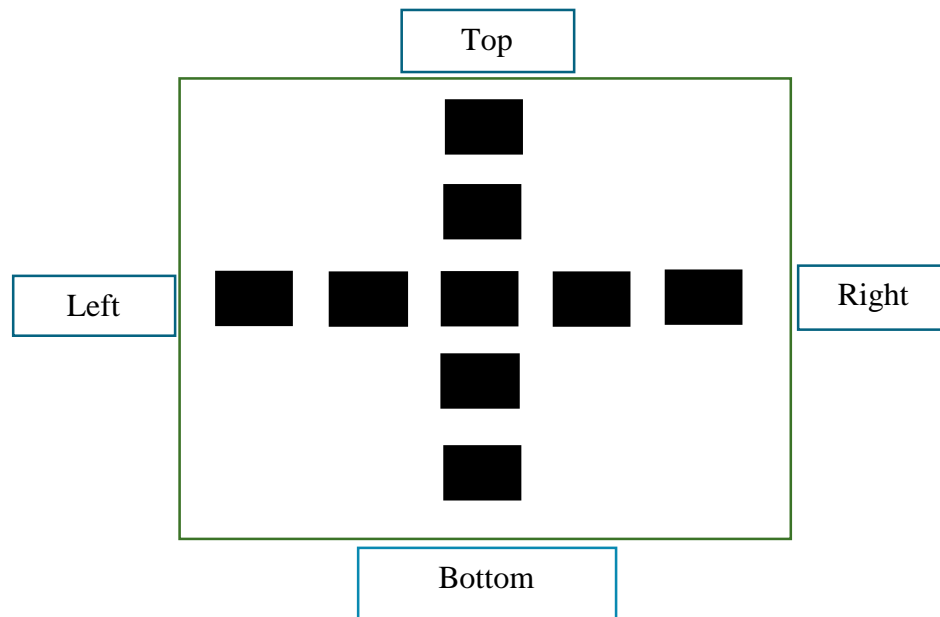


*Figure 6.51: Schematic of the petri dish showing the nanoDots facing the X-Ray beam*

After exposing the nanoDots the dose absorbed at each point was measured to obtain the beam profile. As evident from the results in Figure 6.52 and 6.53, the beam profile stays flat at distances up to 10.16 centimeters from the source. Figure 6.52, shows the beam profile as you move from left to right (x-axis) while Figure 6.53 shows the beam profile in y-axis (top to bottom). The results obtained from this part of the experiment support the findings obtained from the radiochromic film as the graphs suggest that the

beam profile remains flat in either x or the y direction and is independent of the distance from the source.

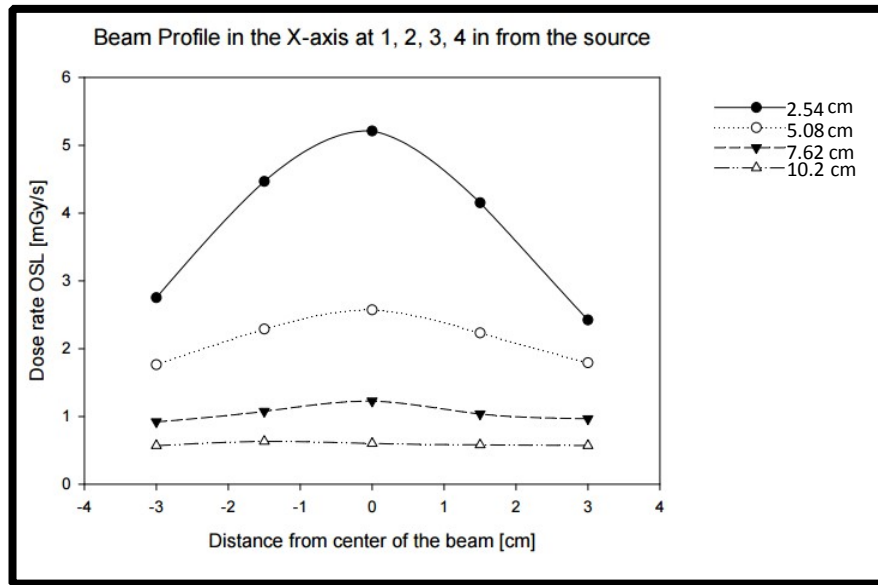


*Figure 6.52: Beam Profile for the x-axis at varying distances from the X-Ray tube*

*[Margarita Tzivaki, Personal Communication, June 2015]*

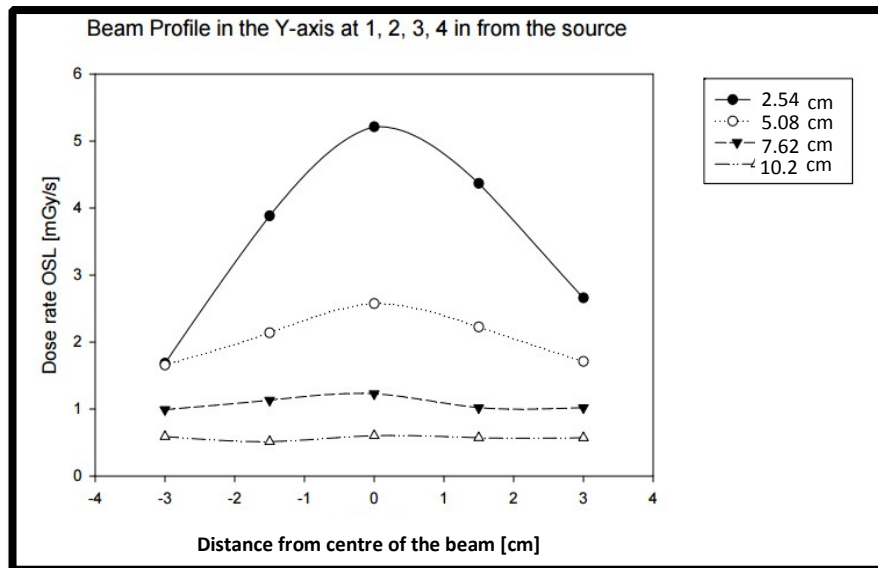


*Figure 6.53: Beam Profile for the y-axis at varying distances from the X-Ray tube*

*[Margarita Tzivaki, Personal Communication, June 2015]*

To conclude, Figures 6.52 and 6.53 can be used to measure the dose absorbed by the fish eggs and the biological impacts of the Mini-X beam can then be evaluated. The biological impacts from the Mini-X beam can then be compared with a higher energy beam, such as, Cesium-137 and this comparison can then be used to establish the relative biological effectiveness of the low energy photons.

## CHAPTER -7

### CONCLUSIONS & FUTURE WORK

The main purpose of this project was to characterize the Mini-X and understand its dosimetric properties along with beam dimensions and uniformity. Through this work, an experimental setup was developed that could be used to safely house all the equipment and hence, carry out the beam characterization experiments. A dual layered shielding was constructed to keep the user protected from the effects of leakage and was designed to keep the radiation leakage well within the regulatory requirements. To complete the characterization process three different detectors were used including Standard Imaging's A-20 ionization chamber, Amptek's X-123 spectrometer and Gafchromic's XR-QA2 radiochromic film. Lastly, a cross-calibration curve was established between Landauer's OSL nanoDots and A-20 ionization chamber with an aim of using OSL nanoDots for a proposed biophysics experiment.

Based on the results obtained, it is concluded that the Mini-X produces a uniform beam with an elliptical shape and the trend stayed true at distances up to 12.7 centimeters from the source. Two different setups including a brass cover and 3 mm collimator were used to investigate beam uniformity and beam dimensions and all the measurement were made using the XR-QA2 radiochromic films. Using the brass cover a uniform beam of 4.8 cm in width and 5.1 cm in height was found at distance of 10.16 centimeters from the source with operating parameters of 20 keV and 50  $\mu$ A. The beam size increased with increasing distance from the source and as expected, a relatively smaller beam was found when 3 mm collimator was used. It is also concluded that the beam size does not change as a function of energy between 10 keV and 25 keV for any fixed distance.

For the dosimetry part of the project, measurements were taken using the A-20 ionization chamber and the air-kerma values were measured as a function of the X-Ray tube potential and current. The air-kerma rate from the Mini-X increases with increasing tube potential and for a given tube potential the air-kerma rate increases with increase in applied current. The air-kerma rate from the Mini-X saturates after 25 keV or in other words there is no increase in air-kerma rate as one increases the energy from 25 keV to 30 keV. Dose rate of 11.56 cGy/s was obtained at operating parameters of 20 keV and 75 $\mu$ A at distance of 2.54 centimeters from the source and this rate went up to 12.21 cGy/s for 25 keV at same current and distance. Apart from air kerma values, dose to tissue values were also calculated. Using the known spectra (measured using the X-123 spectrometer) for different energies, air-kerma values were converted to dose to tissue values and it is found that dose to tissue values are quite similar to air-kerma values. Also, the percent difference between the air-kerma values and dose to tissue values decreases with increase in energy. For example, there is 9.12 % difference between the air kerma and dose to tissue values obtained at 10 keV which further reduces to 7.89 % for 25 keV.

For the last part of the project a cross-calibration curve between nanoDots and A-20 ionization chamber was established for the proposed biophysical experiment. Two different calibration curves were established with tube currents of 100 and 200  $\mu$ A respectively. This was done to provide a calibration curve for low dose rates and high dose rates respectively. It was established that the biological material (fish eggs) would be placed inside a vial and a setup to hold the vial was also constructed. All the dosimetry for this project will be done using the nanoDots. The future work of this project involves irradiating the fish eggs and observing its resultant biological effects. These biological effects would

then be compared with the biological effects caused by a higher energy beam (Cesium-137) and the RBE of the Mini-X would then be established. This RBE value would eventually give an insight into the radiation quality factor for low energy electrons such as those emitted in the beta-decay of tritium. In addition, the biological effect of low energy betas might be explored on other human and non-human samples.

In conclusion, the main objectives of the project were accomplished as an experimental facility to produce a low energy beta mimic from low energy photons was developed and the X-Ray source was successfully characterized. The results obtained suggested low energy photons with average energies similar to tritium beta decay can be produced and hence, can be used to simulate beta irradiation from tritium sources. For future work it is highly recommended that Monte-Carlo simulations be carried out to further investigate the similarity between tritium beta particles and the Mini-X low energy photons on a microscopic level. In other words, it needs to be investigated, how the energy deposited by tritium beta particles within a certain volume of tissue of cellular size compares with that deposited by the photo electrons generated in tissue by the Mini-X photo spectrum.

## APPENDIX-A

### RAW DATA TABLE-ELECTRON STOPPING POWER [12]

Energy (Mev)	Total Stopping Power (MeV cm <sup>2</sup> /g)
1.00E-02	2.26E+01
1.25E-02	1.90E+01
1.50E-02	1.65E+01
1.75E-02	1.46E+01
2.00E-02	1.32E+01
2.50E-02	1.11E+01
3.00E-02	9.65E+00
3.50E-02	8.59E+00
4.00E-02	7.77E+00
4.50E-02	7.12E+00
5.00E-02	6.60E+00
5.50E-02	6.16E+00
6.00E-02	5.79E+00
7.00E-02	5.20E+00
8.00E-02	4.75E+00
9.00E-02	4.40E+00
1.00E-01	4.11E+00
1.25E-01	3.59E+00
1.50E-01	3.24E+00
1.75E-01	2.98E+00
2.00E-01	2.79E+00
2.50E-01	2.53E+00
3.00E-01	2.35E+00
3.50E-01	2.23E+00
4.00E-01	2.15E+00
4.50E-01	2.08E+00
5.00E-01	2.03E+00
5.50E-01	2.00E+00
6.00E-01	1.96E+00
7.00E-01	1.92E+00
8.00E-01	1.89E+00
9.00E-01	1.87E+00
1.00E+00	1.85E+00

<b>Energy (MeV)</b>	<b>Total Stopping Power (MeV cm<sup>2</sup>/g)</b>
4.50E+00	1.94E+00
5.00E+00	1.96E+00
5.50E+00	1.98E+00
6.00E+00	2.00E+00
7.00E+00	2.03E+00
8.00E+00	2.07E+00
9.00E+00	2.10E+00
1.00E+01	2.13E+00
1.25E+01	2.21E+00
1.50E+01	2.28E+00
1.75E+01	2.36E+00
2.00E+01	2.43E+00
2.50E+01	2.56E+00
3.00E+01	2.70E+00
3.50E+01	2.83E+00
4.00E+01	2.96E+00
4.50E+01	3.09E+00
5.00E+01	3.22E+00
5.50E+01	3.35E+00
6.00E+01	3.48E+00
7.00E+01	3.74E+00
8.00E+01	4.00E+00
9.00E+01	4.26E+00
1.00E+02	4.52E+00
1.25E+02	5.16E+00
1.50E+02	5.81E+00
1.75E+02	6.46E+00
2.00E+02	7.11E+00
2.50E+02	8.41E+00
3.00E+02	9.72E+00
3.50E+02	1.10E+01
4.00E+02	1.23E+01
4.50E+02	1.36E+01
5.00E+02	1.49E+01
5.50E+02	1.63E+01
6.00E+02	1.76E+01
7.00E+02	2.02E+01
8.00E+02	2.28E+01
9.00E+02	2.54E+01

## REFERENCES

1. Hall, Eric J, and Amato J Giaccia. "Physics and Chemistry of Radiation Absorption." *Radiobiology for the Radiobiologist*. Sixth ed. 9-14. Print.
2. "Ionizing & Non-Ionizing Radiation." *EPA*. Environmental Protection Agency. Web. 9 June 2015.  
<[http://www.epa.gov/radiation/understand/ionize\\_nonionize.html#ionizing](http://www.epa.gov/radiation/understand/ionize_nonionize.html#ionizing)>.
3. Turner, J. E. "Phenomenon Associated with Charged Particles Track." *Atoms, Radiation, and Radiation Protection*. Third ed. New York: Pergamon, 1986. Print.
4. "Biological Aspects of Heavy Charged Particle Radiation Therapy." Web. 27 May 2015. <<http://www.aapm.org/meetings/amos2/pdf/42-11865-82728-878.pdf>>.
5. "Mimo-Bragg." *MIMO-BRAGG*. Web. 27 May 2015.  
<<http://people.na.infn.it/~manti/MIMO-BRAGG/MIMO-BRAGG-EN.xhtml>>.
6. Knoll, Glenn F. "Radiation Interactions." *Radiation Detection and Measurement*. Third ed. New York: Wiley, 1979. 60-63. Print.
7. Kohan, Leila Mirsaleh, Sunuchakan Sanguanmith, Jintana Meesungnoen, Patrick Causey, Craig R. Stuart, and Jean-Paul Jay-Gerin. "Self-radiolysis of Tritiated Water. 1. A Comparison of the Effects of  $^{60}\text{Co}$   $\gamma$ -rays and Tritium  $\beta$ -particles on Water and Aqueous Solutions at Room Temperature." *RSC Advances RSC Adv.* (2013): 19282. Print.
8. O' Sullivan, Neville Malabre. "Low Energy Photon Mimic of the Tritium Beta Decay Energy Spectrum." (2013). Print. UOIT Library.
9. Nikjoo, H., and D T Goodhead. "Track Structure Analysis Illustrating the Prominent Role of Low-energy Electrons in Radiobiological Effects of Low-LET Radiations." *Physics in Medicine and Biology Phys. Med. Biol.* (1991): 229-38. Print

10. Michael, Bellamy, and Eckerman Keith. "Relative Biological Effectiveness of Low –Energy Electrons and Photons ." *United States Environment Protection Agency*. 20 Oct. 2013. Web. 17 Aug. 2015.
11. Knoll, Glenn F. "Radiation Interactions." *Radiation Detection and Measurement*. New York: Wiley, 1979. 31-36. Print.
12. "Stopping Power and Range Tables for Electrons." *Stopping Power and Range Tables for Electrons*. NIST. Web. 9 June 2015.
13. Turner, J. E. "Phenomenon Associated with Charged Particles Track." *Atoms, Radiation, and Radiation Protection*. Third ed. New York: Pergamon, 1986. Print.
14. "What Is XRF?" *Amptek*. Web. 9 June 2015. <<http://www.amptek.com/xrf/>>.
15. "Miniature X-Ray Source." Web. 2 June 2015.  
<<http://www.amptek.com/pdf/minix.pdf>>.
16. "X-123 Complete X-Ray Spectrometer with Si-PIN Detector." *Amptek*. Web. 2 June 2015. <<http://www.amptek.com/products/x-123-complete-X-Ray-Spectrometer-with-si-pin-detector/>>.
17. "Gafchromic XR Films." *Ashland*. Web. 9 June 2015.  
<<http://www.ashland.com/Ashland/Static/Documents/ASI/AdvancedMaterials/gafchromic-xr-series.pdf>>.
18. "Using a Scanner as Densitometer - Negfix8." *Using a Scanner as Densitometer - Negfix8*. Web. 2 June 2015. <[https://sites.google.com/site/negfix/scan\\_dens](https://sites.google.com/site/negfix/scan_dens)>.
19. "Optical Density Calibration." *OD Calibration*. Web. 9 June 2015.  
<<http://rsb.info.nih.gov/ij/docs/examples/calibration/>>.
20. "Ion Chambers - - LNLS." *LNLS RSS*. Web. 9 June 2015.

<<http://lnls.cnpem.br/beamlines/xafs/equipments/ion-chambers/>>.

21. Knoll, Glenn F. "Ionization Chambers." *Radiation Detection and Measurement*.

Third ed. New York: Wiley, 1979. 132-133. Print.

22. "SuperMAX Electrometer." - *Standard Imaging*. Web. 9 June 2015.

<<http://www.standardimaging.com/electrometers/supermax-electrometer/>>.

23. Seuntjens, J.P., W. Strydom, and K.R. Strydom. "Dosimetric Principles, Quantities and Units." *Nuclear Sciences and Applications*. Web. 9 June 2015.

<<http://www-naweb.iaea.org/nahu/DMRP/documents/Chapter2.pdf>>.

24. "NIST: X-Ray Mass Attenuation Coefficients - Water, Liquid." *NIST: X-Ray Mass Attenuation Coefficients - Water, Liquid*. Web. 8 June 2015.

25. "NIST: X-Ray Mass Attenuation Coefficients - Air, Dry." *NIST: X-Ray Mass Attenuation Coefficients - Air, Dry*. Web. 8 June 2015.

26. "InLight Complete Dosimetry System Solution." *Landauer*. Web. 9 June 2015.

<[http://www.landauer.com/uploadedFiles/InLight\\_nanoDot\\_FN.pdf](http://www.landauer.com/uploadedFiles/InLight_nanoDot_FN.pdf)>.

27. "Inlight Complete Dosimetry System Solution." Web. 9 June 2015.

<[http://landauer.com/uploadedFiles/Healthcare\\_and\\_Education/Products/Readers/InLight\\_MicroStar\(1\).pdf](http://landauer.com/uploadedFiles/Healthcare_and_Education/Products/Readers/InLight_MicroStar(1).pdf)>.

28. Knoll, Glenn F. "Miscellaneous Detector Types." *Radiation Detection and Measurement*. Third ed. New York: Wiley, 1979. 730-732. Print.